In Situ TEM Creation of Nanowire Devices

Alam, Sardar Bilal

Publication date:
2015

Document Version
Publisher's PDF, also known as Version of record

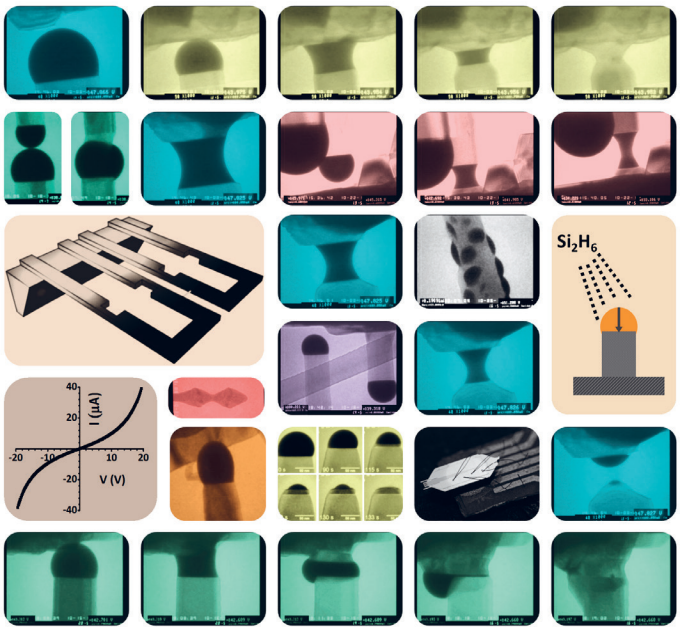

In situ TEM creation of nanowire devices

Sardar Bilal Alam
PhD Thesis May 2015

DTU Nanotech
Department of Micro- and Nanotechnology

Technical University of Denmark

In situ TEM creation of nanowire devices

Sardar Bilal Alam

Ph.D. Thesis, 26th May 2015

Main supervisor: Kristian Mølhave
Co-supervisor: Ole Hansen

Department of Micro and Nanotechnology
Technical University of Denmark

Contents

Abstract

Integration of silicon nanowires (SiNWs) as active components in devices requires that desired mechanical, thermal and electrical interfaces can be established between the nanoscale geometry of the SiNW and the microscale architecture of the device. *In situ* transmission electron microscopy (TEM), which has proved to be a powerful method for visualizing the physical processes involved in the growth of nanowires by the vapour liquid solid (VLS) mechanism, was used to study VLS SiNW contact formation process. Electrical characteristics and effects of surface modification on electrical behavior of SiNW were also investigated *in situ*.

SiNWs were grown on silicon microcantilever heaters using the VLS mechanism. When grown across a gap between adjacent cantilevers, contact was formed when the SiNW impinged on the sidewall of an adjacent cantilever. Using *in situ* TEM, SiNW contact formation process at high temperatures was observed in real time. As the eutectic droplet made contact, it wetted the surface; Si growth catalyzed by the eutectic continued, while at the same time Au often migrated/diffused away from the contact site. The parameters of this contact formation process were measured from movies recorded during contact events. It is demonstrated that the geometry of the final contact formed between the nanowire and the silicon surface could be controlled by varying the contact surface temperature and the electrical current through the bridging SiNW. By adjusting the contact surface temperature and nanowire current, the balance of Si deposition vs. Au migration could be controlled. This gave rise to a variety of contact geometries including a Si to Si contact with controlled shape and diameter, a nano gap, or a Si-Au-Si contact. It is further demonstrated that electromigration is the best candidate for controlling catalyst migration. Kinetics of the contact formation process was studied in detail and the conditions which resulted in different contact geometries are explained.

On completion of the contact, SiNW bridging the adjacent cantilevers was electrically connected at its two ends, base and tip and its electrical properties were probed *in situ* TEM. Such SiNW bridges clamped between two cantilevers *in situ* TEM was an interesting platform for studying the effect of surface modification on SiNWs electrical properties. The effect of surface oxidation was studied and it is demonstrated that oxidation causes substantial increase in the resistance of the nanowire.

Resumé

Integration af silicium nanotråde (SiNWs) som aktive komponenter i silicium-enheder kræver, at der kan etableres ønskede mekaniske, termiske og elektriske kontakter mellem nanowires nanoskala geometri og enhedens mikroskala arkitektur.

In situ transmissions elektron mikroskopi (TEM) har vist sig at være en effektivt metode til at visualisere de fysiske processer, der er involveret i væksten af nanotråde. I dette project bruges *in situ* TEM til at observere hvordan SiNW danner kontakt mellem to silicium mikrobjælker der er elektrisk opvarmede. I spidsen af nanowiren er der en eutektisk guld-silicium dråbe som først rammer bjælen ved siden af.; Si vækst katalyseret forsat af den eutektiske dråber når kontakten er skabt, mens der på samme tid migrerer og diffunderer guld væk fra kontaktstedet. Parametrene for denne kontakt dannelsesproces måles fra film optaget i TEMet. Geometrien af den endelige kontakt dannet i ren silicium mellem nanotråden og microbjælkens overflade kan styres ved at variere kontaktfladens temperatur. Dette kan give anledning til en række kontakt geometrier, herunder en Si til Si kontakt med kontrolleret form og diameter, en nanogap eller en Si-Au-Si kontakt. Det er endvidere påvist, at kontakt strukturerne også kan ændres ved hjælp en electromigrations proces, hvor Au migrationsrate og retning af migration styres ved at sende en strøm gennem wiren under kontakt dannelsesproces.

Efter kontakten er dannet er nanowiren elektrisk forbundet ved sine to ender gennem de to mikrobjlker og dens elektriske egenskaber kan måles *in situ* TEM. Sådanne frithængende nanowires *in situ* TEM er en interessant platform for at studere effekten af ændringer overfladen på nanowirens elektriske egenskaber. Effekten af overflade oxidation og ændring af overfladeruhed blev undersøgt, og det blev vist, at disse overfladebehandlinger forårsage betydelig stigning i modstanden i nanowiren.

I denne afhandling, blev virkningen af høje elektriske felter på nanowires også undersøgt. Høje elektriske felter kan deformere Si-Au dråben hvilket kan være en mulig fremgangsmåde til at ændre retningen af nanowirens vækst.

Conferences

The research presented in this thesis has been presented in the following conferences:

1. Sardar Bilal Alam ,Federico Panciera ,Ole Hansen ,Kristian Mølhave and Frances M. Ross, Creating new VLS silicon nanowire contact geometries by controlling catalyst droplet motion, poster presented at Material Research Society (MRS) Spring Meeting, San Francisco, 2014.

2. Sardar Bilal Alam, Frances M. Ross, Kristian Mølhave and Ole Hansen, *In situ* transmission electron microscopy of silicon nanowire bridge formation, poster presented at meeting of Nordic Microscopy Society, SCANDEM 2013, Copenhagen, 2013.

3. Sardar Bilal Alam, Eric Jensen, Frances M. Ross, Ole Hansen, Andrew Burrows and Kristian Mølhave, Suspended microsystems for *in situ* TEM studies of processes in gases and liquids, oral presentation give at meeting of Microscopy and Microanalysis (M&M), 19(S2), Indianapolis, 2013. (Presented by Kristian Mølhave).

4. Sardar Bilal Alam, Eric Jensen, Frances M. Ross , Ole Hansen, Andy Burrows , and Kristian Mølhave, Microchip-systems for *in situ* electron microscopy of processes in gases and liquids, Conference on *In Situ* and Correlative Electron Microscopy (CISCEM), 2014. (Presented by Kristian Mølhave). *To be published in the abstract book of the conference.*

Publications

Following publications are coming up from the work done in this thesis:

- Creating new VLS silicon nanowire contact geometries by controlling catalyst migration, Sardar Bilal Alam, Federico Panciera, Ole Hansen, Kristian Mølhave and Frances M. Ross. *Submitted to Nano Letters. Manuscript in Appendix E.*

- Exploring VLS silicon nanowire devices *in situ* TEM, Sardar Bilal Alam, Federico Panciera, Aage Andreas Sloth Nilausen, Ole Hansen, Frances M. Ross and Kristian Mølhave. *To be submitted.*

- Controlling nanowire growth through electric-field-induced deformation of the catalyst droplet, Federico Panciera, Sardar Bilal Alam, Michael M. Norton, Ole Hansen, Haim H. Bau, Kristian Mølhave, Stephan Hofmann and Frances M. Ross. *To be submitted.*

Other contributions

Book chapter, "*In situ* TEM Electrical Measurements", Silvia Canepa, Sardar Bilal Alam, Duc-The Ngo, Frances M. Ross and Kristian Mølhave. *Submitted.*

Acknowledgement

Foremost, I would like to express my deepest gratitude to my supervisor Kristian Mølhave. The work in this thesis could not have been accomplished if it was not for Kristian's immense support, encouragement, guidance and motivation. Kristian, I am sorry this was a tough journey and I am grateful for your patience. I was lucky to have Ole Hansen as my co-supervisor. His wealth of knowledge and insight was always helpful. I would also like to thank Peter Bøggild for his encouragement and for introducing me to DTU Nanotech.

My experience visiting IBM T.J. Watson Research Centre was special because of the people I meet and worked with. I am thankful to Frances M. Ross for welcoming me to her lab and facilitating my stay at IBM. I would also like to thank Frances and her family for inviting me to their home on countless occasions. At IBM, I would also like to thank, Yi-Chia Chou, Mark C. Reuter and Jeung Hun Park. A special thank you goes to Federico Panciera for working very late hours with me. The results in this work would not have been possible otherwise. While visiting IBM, I stayed at Dede Emerson's home and I am thankful for her hospitality.

My stay at DTU Nanotech has been memorable because of the smart and helpful people surrounding me. I would like to thank past and present members of the Molecular Windows Group; Eric Jensen, Carsten Købler, Rolf Erling Robberstad Møller-Nilsen, Duc-The Ngo, Rafal Dominik Wierzbicki, Silvia Canepa, Simone Laganà, Christian Kallesøe, and Marcus Levin. Thank you for the fun group meetings.

I had the opportunity to supervise bachelor students and I learned a lot from the experience and from them. In particular, Aage Andreas Sloth Nilausen has been the most impressive. I wish you all success in your research and life. Also, thank you to the administrative staff at DTU Nanotech for helping me out on countless occasions.

I would like to thank Azeem, Faheem and Saifullah for some very interesting discussions over tea in the Nanotech lunchroom. I would also like to thank Kristian Lund Andersen at Lyngby Tennis Klub for welcoming me in his training group. Only five minutes' walk from my office, LTK was a cherished sanctuary when things got tough.

Finally, I would like to thank my family for their love, support and prayers. I am blessed to have them. This work is dedicated to my parents Nazli and Zia.

1 Introduction

Semiconductor nanowires have been extensively investigated due to their unique electrical, optical, and mechanical properties that are a result of their miniature dimensions and single crystal structure. Nanowires are identified as beneficial materials that can enhance the functionality of electronic, optoelectronic, photonic, and electrochemical devices [1]–[6]. Nanowires usually have diameters that range from 10 to 300 nm and are a few micrometres in length. Nanowires have a round, rectangular or polyhedral cross-section depending on the fabrication method.

Semiconductor nanowires have been fabricated using a variety of materials [1],[5],[7] including silicon, germanium and compound semiconductors like zinc oxide. Since the properties and function of a nanowire strongly depends on its structure and composition, it is essential to develop reliable methods for nanowire fabrication and integration. Nanowires have been synthesized by a range of fabrication technologies, categorized as either top-down or bottom-up.

In top-down fabrication methods, the nanowires are carved in a bulk material of desired composition [8]. Top-down fabrication techniques have matured due to decades of extensive research in the development of integrated circuits (ICs). The nanowire structure is defined in the bulk material using lithography techniques like electron beam lithography (EBL), nano imprint lithography (NIL), and deep ultraviolet (DUV) and extreme ultraviolet (EUV) lithography. Once the etch mask is defined onto the bulk material by lithography, the nanowire structure is carved into the bulk material using wet or dry etching techniques. Dry etching is the preferred method as it gives adequate control over the dimensions of the final structure[8].

The bottom-up fabrication method involves epitaxial deposition of the desired material that creates crystalline nanowires. The epitaxial growth requires high temperatures and the material for the deposition is provided by vapour sources. The epitaxial growth of nanowires is either carried out in a chemical vapour deposition (CVD) reactor or, especially for compound semiconductor nanowires, in a metal organic vapour phase epitaxy (MOVPE) system [9].

In 1964, R.S. Wagner and W.C. Ellis, published their work on the fabrication of silicon “whiskers” using a bottom up technique called the vapour-liquid-solid (VLS) mechanism [10], [11]. Since then, the VLS mechanism has become the most common technique for fabricating nanowire structures in CVD or MOVPE systems. Immense advancements have been made to optimize this process and the properties of the nanowire devices fabricated by this scheme. This thesis will focus entirely on silicon nanowires (SiNWs) grown by the VLS mechanism.

Nanowires grown by the VLS mechanism have a wide range of possible applications: in electronics [12], solar cells [13], batteries [14], optoelectronic devices including light emitting diodes [15], lasers [16] and photodetectors [17], thermoelectric devices [18], electro-mechanical devices like resonators [19] and piezoelectric generators [20], as well as biological [21], and chemical sensors [22]. To realize SiNW based practical devices, it is important not only to gain precise control of their length, diameter, surface properties, and contamination but also ensure that reliable electrical, thermal and mechanical contacts can been created between the nanowire and the device.

Recently, self-assembled contact has been realized where the VLS SiNW grows into an opposing surface to create a bridging wire electrically connected at its two ends [23]–[25]. This self-assembled contact formation is catalysed by the metal-Si eutectic droplet at the tip of the wire. Recently, such self-assembled contacts have enabled one-step integration of VLS nanowires as transistors [26], mechanical resonators [27], [28] and sensors [29] by direct growth on these devices *in situ* CVD reactor. The direct integration of VLS nanowires in device architecture bypasses the integration issues that arise with transferring VLS grown nanowires from a substrate to the device [30], [31]. Hence, self-assembled contacts are, possibly, the most promising method for integration of VLS SiNWs in device architecture. However, the kinetics of the contact formation process has not been investigated in detail. For a process that can enable the integration of bottom-up nanowires directly onto potential practical devices it merits further investigation. There are obvious questions that device designers planning to use self-assembled contacts must address: How the contact formation process proceeds? What factors govern the kinetics of the contact formation and contact morphology? And most importantly, is it possible to precisely control the geometry of the contacts to fulfil specific design requirements? In this work, these questions are addressed.

1.1 Project description

As described above, for integration of SiNWs in devices it is essential that the method in which they are integrated in a device i.e. the intricate details of the formation of electrical connection to the nanowire are also understood. In this PhD project, using *in situ* transmission electron microscopy (TEM), the contact formation process for VLS SiNWs was investigated. To accomplish this task, the complete life cycle of VLS grown SiNWs, from their creation to electrical measurements and finally destruction were recorded.

1.1.1 Background – previous work

This study started where the work done by Dr. Christian Kallesøe under the supervision of author's main supervisor, Dr. Kristian Mølhave left off [32]. Kallesøe et al. [25], [33] grew SiNWs on locally heated regions of microcantilevers *in situ* TEM. The wires were grown in an ultrahigh vacuum TEM (UHV-TEM) using gold catalysed VLS mechanism [10], [34]. Kallesøe et al. grew the SiNW from one locally heated cantilever to an adjacent cold cantilever. When the impinging SiNW made contact with the sidewall of a cold (ca. at 70^{o}C) adjacent cantilever (See Figure 1.1), the catalyst droplet on the tip of the wire solidified, resulting in the creation of a

contact between the wire tip and the adjacent cantilever. The SiNW was thus electrically connected at its two ends, base and tip, through the two cantilevers and its electrical properties were probed *in situ* TEM at room temperature.

The work was done in collaboration with the Dr. Frances M. Ross at IBM T.J. Watson research centre in Yorktown, New York, where the UHV-TEM is located. The *in situ* TEM experiments presented in this PhD thesis were also conducted at IBM.

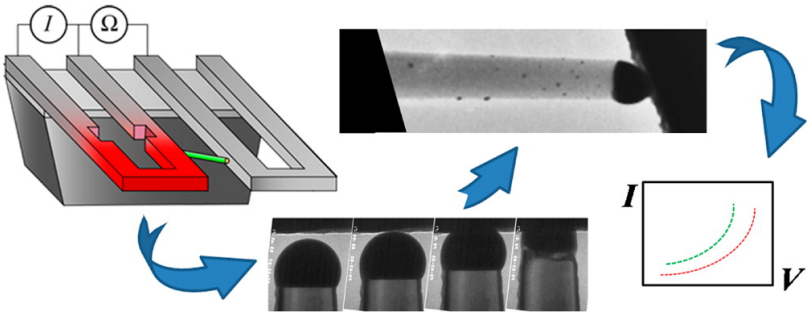

Figure 1.1 SiNW is grown from one cantilever to an adjacent cantilever *in situ* TEM. On contact the AuSi eutectic droplet solidifies and thus a SiNW bridge between the two cantilever is created whose electrical properties can be probed. Reproduced from [25].

1.1.2 **The present work**

The work by Kallesøe et al. [25] was confined to creating SiNW contacts where the contact surface was cold and the final contact was a Si-Au-Si structure. This is not representative of the conditions in a chemical vapour deposition (CVD) reactor, in which the entire sample is at growth temperatures and a Si-Si contact is created [23], [24]. In this work, the temperature of the contact surface was controlled and was set in the growth temperature range to replicate actual conditions, albeit at much lower CVD precursor gas pressures compared to CVD systems due to constraints of the TEM operation.

Microfabricated chips were developed, which were designed specifically for *in situ* TEM growth of nanowires. The chips comprised of silicon microcantilever heaters on which SiNWs were grown locally by VLS mechanism, with AuSi eutectic droplets as the catalyst and disilane as the precursor gas (See Figure 1.2). SiNWs were grown from one locally heated cantilever to an adjacent hot cantilever and allowed to impinge the adjacent cantilever. Kinetics of the contact formation process that follows when the SiNW impinges on the sidewall of the adjacent cantilever was studied in detail.

Electrical properties of the SiNWs bridging the two cantilevers were also probed at different temperatures *in situ* TEM. Carrying out both growth and electrical measurements *in situ* prevented contamination and oxidative surface effects that would arise due to exposure to air. After completion of a SiNW bridge, the surface of the SiNW was altered by oxidation and the correlation between change in surface conditions and current-voltage characteristics was established.

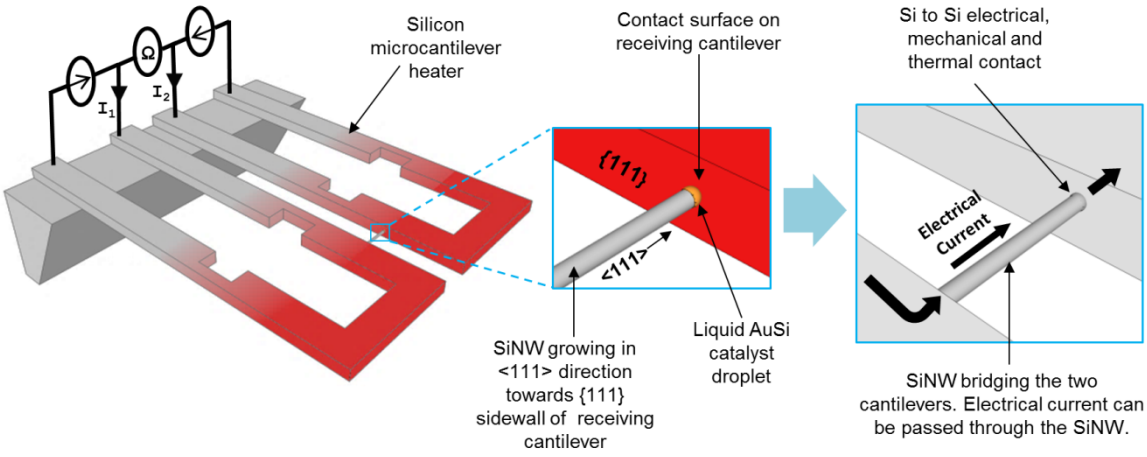

Figure 1.2 Schematic of the experimental set up for studying VLS SiNW contact formation.

1.1.3 Thesis outline

This thesis is structured in seven chapters. The description of the TEM equipment is presented in Chapter 2, while the experimental work done on developing microcantilever heaters is described in Chapter 3. VLS nanowire growth mechanism and the *in situ* TEM growth are introduced in Chapter 4. The nanowire contact formation is presented in Chapter 5. The kinetics of the contact formation is a complex process due to various way in which Au can migrate from the contact site. Chapter 5 will describe the many possible Au migration mechanisms and the different contact geometries that can be created by controlling catalyst motion. The conclusions from Chapter 5 are explained in the paper in Appendix E. In Chapter 6, electromigration of catalyst is discussed and the possibilities enabled by controlling electromigration is described as it can easily be made the most dominant migration mechanism that controls contact geometry. The electrical properties of the nanowires need to be well understood in order to develop reliable devices in the future. The current-voltage characteristics of the SiNW and the effect of surface treatments on the electrical properties are discussed in Chapter 7.

1.1.4 Additional output and future research activities in this project

In addition to the work presented in this thesis, during the course of the PhD studies, additional projects were carried out as dissemination requirement by Technical University of Denmark (DTU). This involved co-supervision of the bachelor thesis of student Aage Andreas Sloth Nilausen. In this project, polysilicon heaters embedded in a silicon nitride membrane were developed for *in situ* TEM experiments.

Another project where co-supervisory work was done was related to polysilicon nano ribbons. Two bachelor level student groups (each comprising of three students) was supervised in different semesters. In this project 50-80 nm thin polysilicon nano ribbon based SOI field effect transistors (FET) were fabricated by a top-down fabrication process and

the mobility and carrier distribution of the polysilicon channel was investigated by the FET operation.

The electrically connected SiNW bridges, created in this study, are now being investigated at Centre for Electron Nanoscopy (CEN) at DTU using electron holography. Preliminary experiments on using electron holography to study biased SiNW have been conducted and further work in this direction will be conducted in the near future.

The growth of nanowires *in situ* TEM is time consuming and the SiNW surface is coated in about monolayer of Au. Therefore nanowires are also being fabricated by more technology relevant processes of e-beam lithography. Presently work is in progress in characterizing these "clean" Au free nanowires for their electrical properties and comparing them to VLS nanowires. But this work goes beyond the present thesis.

1.1.5 **Funding and collaboration**

This work was done at the Molecular Windows Group (MoWin) at the Department of Micro- and Nanotechnology (DTU Nanotech), Technical University of Denmark (DTU), Kgs. Lyngby, Denmark. The main PhD supervisor is MoWin group leader Dr. Kristian Mølhave, while Prof. Ole Hansen is the co-supervisor.

This research was part of the FTP Nano Live project, which was funded by The Danish Council for Independent Research (Case No.10-083797). The project benefited from the state-of-the-art facilities available at DTU. The microcantilever heater chips were fabricated at the cleanroom facilities of DTU Danchip. Experiments on *in situ* TEM growth of nanowires were performed at IBM T.J. Watson Research Centre (Yorktown, New York, USA) in collaboration with Dr. Frances M. Ross and Dr. Federico Panciera. The TEM imaging analysis was also conducted at Centre for Electron Nanoscopy (CEN) DTU.

2 *In situ* transmission electron microscopy

From an early stage in the development of transmission electron microscopy, it was desired that the microscope should be transformed into a micro-laboratory in which response of the specimen to external stimuli and surrounding environment could be recorded in real time [35]. Such a TEM system will be a powerful analytical tool; being able to record the state of materials at high spatial resolution under varying conditions of environment , temperature, stress, irradiation and/or voltage bias etc. Increasing interest and development in *in situ* TEM techniques has gradually matured to a level where at present performing experiments under near realistic conditions has become feasible while maintaining high spatial resolution [36]. The advancement in *in situ* TEM has come forth by the development of electron optics and also by the advances made in micro-and nanofabrication technology [8], which resulted in the development of lab-on-chip systems that can be integrated with special TEM holders and serve as the miniature laboratory to perform the experiments under controlled conditions.

In this chapter, *in situ* TEM is briefly introduced, starting with a brief introduction to TEM, set-up, advantages and challenges of *in situ* TEM experiments and at the end, presenting the TEM at IBM used in this work for *in situ* growth of SiNWs.

2.1 Transmission electron microscope – a brief introduction

Richard Feynman, in December of 1959, gave an often quoted talk titled "There's plenty of room at the bottom" [37]. The objective of the talk was to motivate the scientific audience to explore a new field of science, that later came to be known as nanotechnology. Nanotechnology is defined as the understanding and control of matter at the nanoscale, i.e. it involves imaging, measuring, modelling and manipulating matter at length scale between approximately 1 and 100 nanometres [38]. Feynman, in his talk, put great emphases on the improvement of electron microscopes, with strong precedence: electrons have wavelength small enough to probe the physics of nanomaterials. Transmission electron microscopes have the ability to resolve nanoscale structures in great detail, and are hence an invaluable tool for nanotechnology.

Visible light microscopes have limited capability of resolving nanostructures as their resolution is limited by the wavelength of light. The resolution of optical and electron microscopes can be expressed by the classical Rayleigh criterion [39]:

$$\delta = 0.61\frac{\lambda}{\mu \sin\beta} \tag{2.1}$$

where δ is the smallest distance that can be resolved, λ is the wavelength of the radiation, μ the refractive index of the viewing medium and β the semi-angle of collection of the objective lens. Optical microscopes can often reach a resolution of δ =200 nm, slightly less than the wavelength. However, for electrons the wavelength is typically a few picometers, and δ can be less than 1 Å. For example, at 300 kV accelerating voltage, the relativistic wavelength of electron is about 2 pm. The relativistic regime is used because at this accelerating voltage, electrons travel at speeds comparable to the speed of light. The wavelength of an electron in picometers should ideally translate into sub-atomic scale imaging. However, in practice, the resolution of TEM is limited by the aberrations introduced by the electron lenses and the electron emission setup.

Electrons lenses employ an axially symmetric magnetic (or electric) field for focusing electrons. If the lens is perfect, then the image wave is identical to the object wave, except for the magnification. In this case, the image is a copy of the object, and information is transferred faithfully. But in real microscopes, electron lenses suffer from aberrations; the image wave keeps the same information content as before, but the information is "blurred" due to lens imperfections. The most important defects in images produced by TEM are spherical and chromatic aberrations and astigmatism [39].

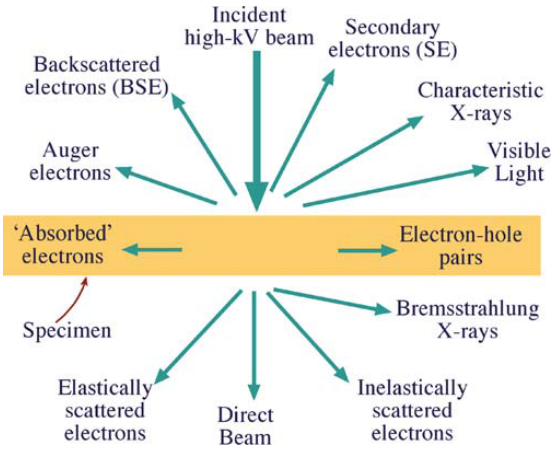

Figure 2.1 Examples of the possible signals generated, when an incident high kV electron beam interacts with matter. Reproduced from[39].

TEM provides images and diffraction patterns simultaneously as well as spectroscopic information by transmitting a beam of electrons through an ultrathin sample. To extract the information from the TEM data, it is important to understand how the incident electrons interact with the sample (and the microscope). When the thickness of the sample is comparable to the mean free path of the electron, part of the incident beam will pass through the sample unaffected and while the other fraction will be involved in electron-matter interactions, which are summarized in Figure 2.1. If there are no scattering, there will be no

mechanism to create TEM images, diffraction patterns and spectroscopic data. The transformation of the uniform intensity of the incident electron beam into non-uniform intensity after scattering by the specimen is the basis for the TEM operation. It is this non-uniformity that translates into contrast in the image. The non-uniform electron intensity beam transmitted from the sample is magnified and focused on the viewing screen or the electron detector. The image created in TEM is a 2D projection of a 3D specimen.

There are different mechanisms by which contrast is created in the TEM image, which include amplitude contrast and the related Z-contrast, diffraction contrast, and phase contrast. Amplitude contrast is due to incoherent elastic scattering of electron, also called Rutherford scattering. Elastics scattering is a function of the atomic number (Z); specimen with higher Z will scatter more electrons. As the thickness of the specimen increase, the number of interactions increase as well (mean free path is fixed), which increases incoherent elastic scattering events as well. The points in the specimen with higher Z and/or thickness produce appreciable scattering, and many of the electrons incident on such points are excluded from passing on through the lens aperture. This creates the contrast in the image, as high Z and/or thicker points in the sample will contribute to fewer electrons transmitted to the image compared to a thinner or low atomic number region, which will be brighter in the image plane. Z-contrast is the atomic scale mass-thickness contrast imaging scheme, better suited for scanning TEM (STEM).

Diffraction contrast is produced by coherent elastic scattering and is widely used contrast mechanism for studying crystals. Diffraction contrast, utilizes the Bragg diffraction condition which depends on the sample crystal structure and orientation. Diffraction contrast can be considered as a special form of amplitude contrast, where the scattering occurs at Bragg angles [39].

Phase contrast can be used to image the atomic structure of thin specimens. The transmitted and diffracted waves have different phase. Phase contrast is present when there is more than one beam contributing to the image and the phase contrast arises due to interference of these beams [39].

It is beyond the scope of this thesis to dwell into more in-depth discussion of a TEM. For a thorough treatment of TEM, the reader is referred to [39] and the excellent online resource [40].

2.2 *In situ* TEM

For the *in situ* TEM silicon nanowire experiments, an electrically contacted chip system in the sample holder and a gaseous environment with silane or disilane is required. In this section, various ways to achieve such *in situ* TEM setup are explained after a brief introduction of advantage and challenges of *in situ* TEM.

2.2.1 Advantages of *in situ* TEM

To improve the performance of nanomaterials, a deep understanding of their structure, functionality and stability under normal operational conditions is essential. Conducting experiments *in situ* TEM, nanostructured materials can be investigated with high spatial resolution in environments that are approximately equivalent to realistic ex-situ device operation.

The motivation behind ever increasing interest in performing *in situ* TEM studies stems from the exceptional amount of quantitative information that can be gathered from such experiments. Performing *in situ* TEM experiments can provide us with:

1. Real time observation of processes that occur on the nanoscale in reactive environments. For example, in this work, the SiNW contact formation was observed in great detail by *in situ* TEM.
2. Real time observation of the response of the specimen to external stimuli and to establish causality. For example, electrical measurements on nanowires can change the wire structure due to electromigration effects or Joule heating, hence altering the electrical response. Using *in situ* TEM, the relation between SiNW structural changes and its electrical behaviour can be established in real time.
3. Knowledge of pre-existing state of the specimen like surface morphology, defects, contaminations.
4. Precise measurement of the nanostructure dimensions. For example, interpreting current-voltage characteristics of nanowires requires information on exact cross-sectiontional area and thickness of surface coatings.
5. Quantitative data from the *in situ* experiments can be extracted from different TEM techniques including diffraction, electron holography and EELS (electron energy loss spectroscopy).

2.2.2 *In situ* TEM Challenges

The advantages mentioned above make *in situ* TEM an attractive tool for researchers; however, such sophisticated experiments cannot be taken lightly and a number of technological challenges must be overcome.

For *in situ* electrical characterization, a key challenge is to create robust electrical interface between the nano/micro scale of the specimen and the macro scale of the sample holder of the TEM. This means special holders with electrical leads and contact interface to specimen need to be fabricated. For example, measuring electrical and mechanical properties of bottom-up nanowires and nanotubes often requires micromanipulator systems to pick and place or pre-manipulate the 1D-nanostructure that is latter shifted in the TEM [41], [42]. Or by creating mechanical manipulator systems inside TEM holders that can contact and probe a wire *in situ* TEM [43]. The option used in this work is more direct, in which electrical contacts

were created at the two ends of the nanowire by growing wire from one electrical connection (microcantilever heater) to another.

Another issue is the effect of electron beam on the measurements. For instance, irradiation by electrons on a silicon sample can create electron-hole pairs and trapped electrons in the silicon-silicon oxide interface that will change the current-voltage behaviour of the sample. Moreover, sample preparation could have adverse effects. Gallium (Ga) ion based focused ion beam (FIB) milling has become a standard method for creating TEM lamella. FIB milling of semiconductors create amorphous surfaces in sample and the impact of Ga ion contamination on electrical properties is not fully understood. Moreover, samples like thinned down p-n junctions created from FIB milling of semiconductor devices will be affected by their surface properties that can dominate the electrical behaviour. This implies that translating the results of *in situ* measurements to actual semiconductor devices need careful consideration of the sample surface and its preparation methods.

2.2.3 **Gaseous environments in a TEM**

The electron beam will interact with the gas molecules. Electrons will be scattered by the gas, which reduces the intensity of the final image as scattered electrons are blocked by the aperture. Moreover, electrons can also ionize the gas, which results in the creation of very reactive radicals that can have unwanted interactions with the specimen and modify the results. To minimize the electron beam interactions with gas, it is ideal to keep the gas volumes in the TEM as small as possible. The introduction of controlled gas environment in a TEM can be accomplished through two different techniques: closed-cell approach and differential pumping [36].

The differential pumping technique involves modification to a TEM column in an environmental TEM: The gas is introduced by controlled flow directly into the pole piece gap, usually at a pressure less than 20 Torr [36]. To keep the gas volume surrounding the sample as small as possible, pressure limiting apertures are inserted in the bore of the pole-pieces and additional pumping channels are introduced in the microscope column [36].

In the closed cell system, special TEM holders are used which enclose the gas between two electron transparent membranes, made typically of carbon or silicon nitride. The gas surround the sample in this closed compartment, which is usually 10 to 200 μm thin [36]. There are many advantages of this approach: high pressures up to ca. 1bar (750 Torr) can be used, liquids instead of gas environment are also feasible, and this approach does not need an E-TEM and can be used with any TEM that can accept the special holder. The disadvantage is that the electrons will interact with the enclosing membranes; the interactions degrades the spatial resolution [36].

2.3 TEM at IBM

In this work, the SiNWs were grown in an ultra-high vacuum (UHV) TEM located at Dr. Frances M. Ross lab at IBM T.J. Watson Research Centre, New York. Figure 2.2(a) shows the UHV-TEM, which is a Hitachi H-9000 model with a base pressure of 0.2 nTorr [34]. To grow the SiNWs by VLS mechanism the precursor gas, disilane, was introduced in the UHV-TEM column. A maximum pressure of 20 μTorr can be maintained while the electron beam remains on.

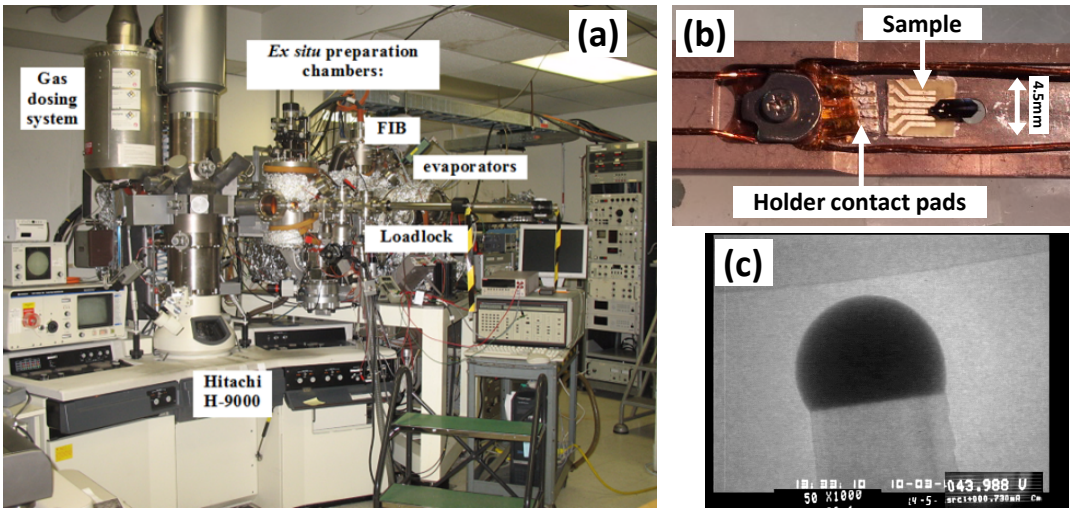

Figure 2.2 (a) UHV-TEM at IBM (Courtesy of IBM), **(b)** section of TEM sample holder with cantilever heater chip attached, and **(c)** bright field image of a SiNW approaching the facet on the side wall of a silicon cantilever.

For the purpose of growing SiNWs, there were two stages before the sample reached the TEM column. The sample was first inserted in the load lock, which had a tungsten filament lamp near the sample for baking and was pumped by a turbo and roughing pump. Samples were left in the load lock for several hours (preferably overnight) before transferring to the second stage, which was "the round house". The round house was part of the *ex situ* preparation chambers. A Knudsen cell metal evaporator, made of a quartz crucible and tantalum Joule heating element, was located in the round house and used for evaporating catalyst Au on the sample (microcantilever heater chips). After Au deposition, the sample was transferred directly to the TEM column.

The TEM holder had four electrical contacts available, which were sufficient for independently heating two microcantilever heaters. Figure 2.2(b), shows part of the TEM holder with the microcantilever heater chip. The wires running through the TEM holder were soldered to a fixed PCB with contact pads. The chip itself was mounted on a PCB, which was attached to the holder by silver paste. The contact pads on the sample PCB were connected to contact leads on the TEM holder by wire bonding. In this technique contact pads are connected through fine metallic wires, which are bonded to each contact pad with the assistance of an ultrasonic welding mechanism [44], [45]. Wire bonding offered a more flexible contacting regime in which connections between the chip and the specimen holder could be established in any

desired combination. The wire bonding technique used was wedge bonding with Al wire, since it is a room temperature technique as opposed to ball bonding which requires elevated temperature (normally above 120^{o}C).

Images in the UHV-TEM were produced using 300 kV accelerating voltage with the beam current being 1.5 nA. Bright field (BF) imaging mode was mostly used, where only the transmitted primary beam creates the image. Example of the BF image is shown in Figure 2.2 (c), where a SiNW is approaching a facet on the sidewall of receiving cantilever. Si is medium grey and the high Z liquid AuSi eutectic semicircle is darker, due to much higher scattering events. The images were recorded on MiniDV cassettes at a frame rate of 29.97 fps and were later digitized with each frame size of 640 x 480 pixels. The pressure reading from the TEM column and readings of the current/voltage sources were interlaid in the images. Hence, almost all vital parameters of the experiment were available in the images. This helped in synchronization and keeping track of the experiments with respect to time.

3 Microcantilever heaters

Typical temperatures for growth of SiNWs with the VLS mechanism *in situ* UHV-TEM were in the range of 470 to 520^{o}C. Growth temperatures were achieved using silicon microcantilever resistive heaters as the growth platform. Growing SiNWs and carbon nanotubes (CNTs) on microfabricated cantilevers is a well-known technique [33], [46], [47]. The advantages of using microcantilever heaters stems from their microscale geometry, which results in sub-millisecond response times [48], low power consumption (in mW range), and localized growth as growth temperatures are confined to limited section of the microcantilever, which itself constitutes a small part of the entire chip.

Microcantilever heaters are very valuable tools in optimizing SiNW or CNT growth parameters. By careful design, the temperature profile of the cantilever heater, with the desired maxima and gradient, can be controlled. Introducing a well-controlled temperature gradient along the cantilever structures allows the study of nanowires or CNTs growth over a large temperature window in a single experiment [47].

A possible future advantage of microheaters is that they could enable the post processing integration of SiNWs grown by VLS method to CMOS and polymeric lab-on-chip devices. Normal growth temperature in standard epitaxial growth systems far exceeds the limit for CMOS (450^{o}C) and polymers (100-150^{o}C). In addition, the fabrication of CMOS and lab-on-chip devices involves wet processes that can displace SiNWs. Hence, a yet unexplored approach for integration of epitaxial SiNWs with CMOS and lab-on-chip devices is to integrate them after the rest of the device fabrication is completed. This can be accomplished by incorporating microheaters in CMOS and lab-on-chip devices. Since heating is localized, SiNWs can be added to the device in the final stage without exposing the entire device to SiNW growth temperatures. Such an approach is particularly interesting for integrating nanowires composed of materials other than Si with CMOS devices.

This chapter presents the design, fabrication and characterization of the microcantilever heaters that were used for *in situ* TEM growth of SiNWs. Different variations of microcantilevers with distinct temperature profiles were designed and fabricated; some even had the added functionality of electromechanical actuation. However, limited time on the UHV -TEM meant that not all microheater designs could be tested. This chapter will only present the design which worked the best and all the experimental results in the following chapters were obtained using heaters of that particular design shown in Figure 3.1.

This chapter starts by presenting the overall design and electrical characteristics of the heater device. This is followed by a discussion of the results of the finite element modelling performed to estimate the temperature distribution of the cantilever. The fabrication of the

microcantilevers is briefly outlined and finally the performance of the devices is evaluated based on *in situ* TEM measurements of temperature calculated from SiNW growth rates.

3.1 Microcantilever heater design

The unique geometry of the Joule heated silicon microcantilever heaters fulfilled the essential design requirements of this work. An obvious design requirement, which free standing cantilevers satisfied, was that the growth platform should not obstruct the TEM electron beam transmitted through the SiNWs. Secondly, SiNW contact formations should be studied for a range of receiving contact surface temperatures, which was also fulfilled as the temperature of each microcantilever could be independently controlled. And finally, electrical characterization could be performed on SiNWs *in situ* TEM at different temperatures after the contact was created, which was also possible as both cantilevers were electrically isolated from each other and the Si substrate by a silicon dioxide layer.

Figure 3.1 shows the schematics of two adjacent identical microcantilever heaters. The dimensions stated in Figure 3.1 are not the planned dimensions, rather the actual numbers measured from fabricated devices. There were issues related to fabrication that altered the dimensions from their initial design values (discussed in Section 3.4).

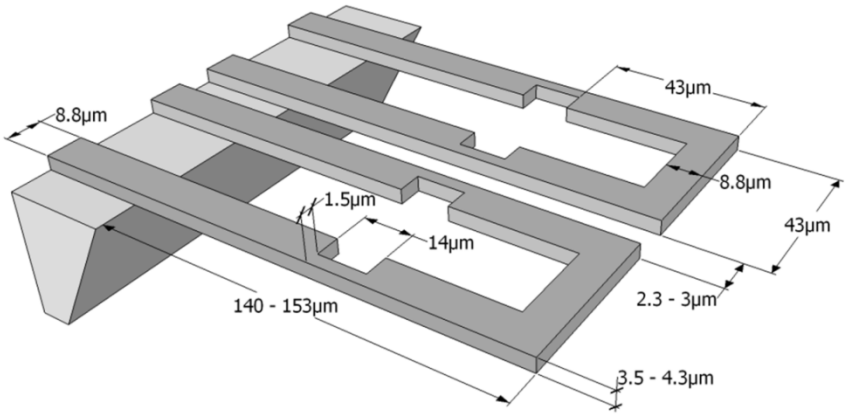

Figure 3.1 Schematic representation of the microcantilever heaters (not drawn to scale). The dimensions correspond to the measurements on the final fabricated devices.

SiNWs usually grow in the <111> crystal direction. Hence, the silicon microcantilever heaters were designed to be made from a silicon-on-insulator (SOI) wafer with a <110> monocrystalline highly doped p-type device layer, such that the opposing sides of adjacent cantilevers were {111} planes as shown in Figure 3.2. The intended temperature profile of the heater is also illustrated. The 1.5 µm narrow constriction (notch) in each leg of the cantilever loop has high thermal resistance to restrict heat transfer to the sink (chip body), with the purpose that growth temperatures and, hence, growth of SiNWs was confined to the upper part of the cantilever loop. Limiting the size of the region where growth occurred enabled easy tracking of SiNW contact events in the TEM, in which the magnification was usually set very high and the entire cantilever was not visualized at a given time. Also, incorporating a notch meant that the thermal gradient from the tip of the cantilever to the start of the notch

was not very large, hence the wires grew at similar growth rates and contacted the adjacent cantilevers with lesser time between them. Most importantly, the high thermal resistance of the notch meant that the upper part of the cantilever loops got much hotter compared to loop without any notch for a given electrical power.

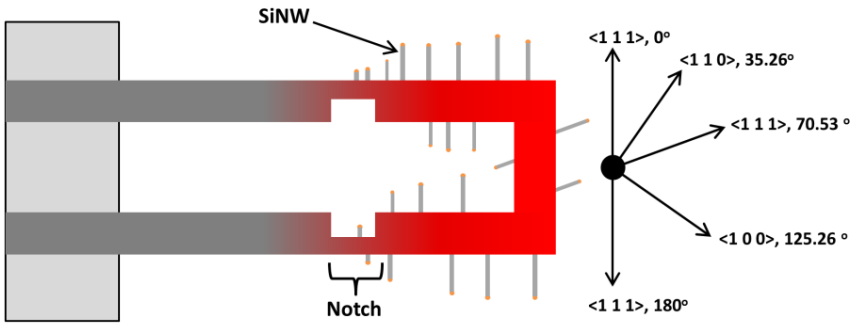

Figure 3.2 Schematic of the top view of microcantilever heater with SiNWs growing in the <111> family of directions on the cantilever sidewalls. Some of the crystal directions which lie parallel to the plane of the page are indicated. The temperature profile of the heater is also illustrated with tip being the hottest part of the cantilever (indicated by bright red colour) and the temperature gradient is the highest over the notches in each leg of the cantilever.

3.2 Joule heating of silicon cantilevers

Joule heating occurs due to collisions between moving charge carriers and the atoms of the conductor upon application of an electric current. Charge carriers are accelerated in the presence of an electric field and they impart part of their gained kinetic energy to the atomic ions of the conductor through collisions. This increases the vibrational energy of the ions which manifests as rise in temperature.

Figure 3.3 shows the experimentally obtained current–voltage (I-V) characteristic of a microcantilever heater chip operated *in situ* UHV-TEM during SiNW growth. The I-V plot has three distinct regions, where each region represents a change in cantilever resistance as temperature increases with increase in current. To understand I-V characteristics of the silicon microcantilevers, it is important to consider how the electrical resistivity of silicon depends on temperature.

The resistance R of a section of doped single crystal silicon microcantilever is described as

$$R = \frac{\rho L}{t_x W} \tag{3.1}$$

where L is the length, t_x is the thickness, and W is the width of the microcantilever section and ρ is the resistivity defined as:

$$\rho = \frac{1}{\sigma} = \frac{1}{q(n\mu_n + p\mu_p)} \tag{3.2}$$

where σ is the conductivity, q is the elementary charge, n is the electron concentration, p is the hole concentration, and μ_n and μ_p are electron and hole mobility respectively. Both carrier mobility and concentrations are dependent on temperature.

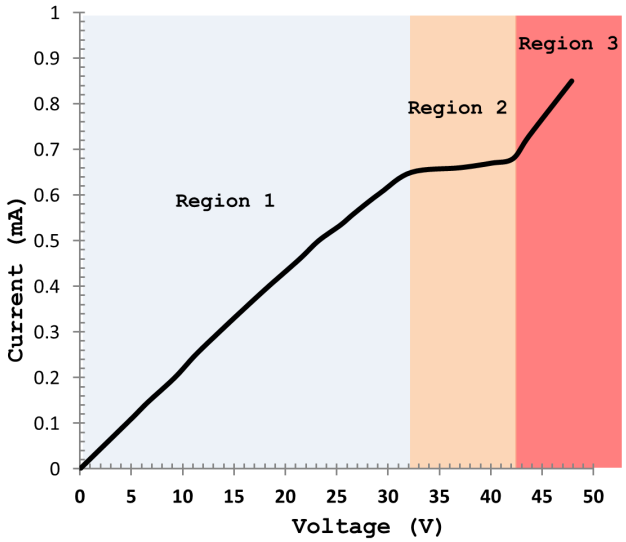

Figure 3.3 I-V characteristic of a microcantilever heater measured *in situ* UHV-TEM.

The concentration of holes (p) and electrons (n) of p-doped silicon are expressed as follows:

$$p = \frac{1}{2}\left(N_A + \sqrt{N_A^2 + 4n_i^2}\right) \tag{3.3}$$

and

$$n = \frac{n_i^2}{p} \tag{3.4}$$

where N_A is the acceptor dopant concentration (all acceptor atoms are assumed to be activated) and n_i is the intrinsic carrier concentration, which is the concentration of thermally excited electrons in the conduction band (and holes in valence band) of undoped and defect free silicon. Intrinsic carrier concentration is expressed as:

$$n_i = \sqrt{N_c N_v e^{-\frac{E_g}{k_b T}}} \tag{3.5}$$

From Equation 3.5, it can be seen that the intrinsic carrier concentration depends on the temperature T, energy band gap E_g and the density of states N_c and N_v of conduction and valence band respectively. E_g, N_c and N_v also have a dependence on temperature T and their formulation can be found in most text books on semiconductor physics, like[49].

The electron (μ_n) and hole (μ_p) mobilities dependence on temperature and dopant concentration can be defined by Arora mobility model [50]:

$$\mu_n = 88T_n^{-0.57} + \frac{7.4 \times 10^8\, T^{-2.33}}{1 + [N_A/(1.26 \times 10^{17} T_n^{2.4})]0.88T_n^{-0.146}} \tag{3.6}$$

and

$$\mu_p = 54.3T_n^{-0.57} + \frac{1.36 \times 10^8\, T^{-2.23}}{1 + [N_A/(2.35 \times 10^{17} T_n^{2.4})]0.88T_n^{-0.146}} \tag{3.7}$$

where $T_n = T/300$.

In Figure 3.3, at low voltages (Region 1), the microcantilever current increases with voltage according to Ohm's law; indicating that resistance remains relatively constant at low voltages (temperatures). As the voltage increases (Region 2), the temperature increases due to Joule heating and the current increases slowly indicating an increase in the resistance of the microcantilever. This increase is due to the fact that charge carriers mobility decreases as the temperature increases and the carrier concentrations (also dependent on temperature) remains relatively constant.

In Region 3 of the I-V plot, as the voltage and current (hence dissipated power and temperature) increases, the carrier concentration begins to increase at a much higher rate, (governed by the term $e^{-1/T}$ in Eq. 3.5), than that at which mobility is decreasing defined by $\sim T^{-2.2}$ (Eq. 3.6 and 3.7) [50], [51] . This causes the microcantilever resistance to drop and the current increases rapidly. As the voltage (temperature) is increased further, thermal carrier generation will increase the intrinsic carrier concentration to a level that exceeds the dopant concentration and silicon will become intrinsic [52]. Since the current increase rapidly in the transition from Region 2 to Region 3 in the I-V plot, it is prudent to operate the power supplies as constant current sources for Joule heating of silicon heaters to avoid destroying them.

In addition to Joule heating, a secondary effect owning to the Thomson effect arises at the micro and nanoscale [53]. The Thomson effect occurs in a conductor that is exposed to a temperature gradient. The Thomson effect becomes important when the device dimensions are scaled down and it becomes more dominant than convection and radiation heat loss mechanisms. Due to the Thomson effect the phenomena of "temperature peak drag" occurs in microheaters, by which the temperature peak at the centre of the bridge is shifted by several microns [53]. In case of boron doped microcantilevers, the temperature peak at the tip will be dragged towards the positively biased cantilever leg as it corresponds with the direction of current flow since the hot carriers also carry thermal energy. However, since the growth at the tip is not relevant for contact studies, and the notch architecture in the experiment proved to be very efficient in confining high temperatures to the upper part of the loop where the thermal gradient is relatively small (in the order of 0.2 to 1 K/μm), the peak drag can be ignored. However, it should be stated here that there will be varying degree of hot region's extension in the two notches of the cantilever.

Another outcome of heating the cantilever is their expansion due to the rise in temperature. In an over-simplified case, the change in length ΔL of cantilever of length L, when the temperature increases by an amount ΔT is given as:

$$\Delta L = \alpha L \Delta T \tag{3.8}$$

where α is the coefficient of linear thermal expansion, which for Si also has a dependence on temperature. Thermal expansion can be critical if the coefficient of linear thermal expansion of the bulk silicon (microcantilevers) is different from the bridging SiNW between the cantilevers and the contraction of the SiNW and the cantilever in the cooling cycle is in the opposing direction. During the designing phase of the microcantilever heaters it is assumed that linear thermal expansion of SiNWs is the same as bulk Si. From Equation 3.8, it can be seen that ΔL has a dependence on L, hence the length wise expansion of cantilevers is more than the sideways, which is the reason SiNW contacts are created between parallel cantilevers. In this work, "loop in loop" designs were also made where expansion difference of the two cantilever loops was only within a few nanometers but experiments on that design did not yield wires that were long enough to make contacts and there was not sufficient time available to optimize growth on those cantilever designs. The "loop in loop" cantilever designs are presented in Appendix A.

3.3 FEM modelling of microcantilever heaters

Finite Element Modelling (FEM) programme COMSOL Multiphysics (Version 4.3) was used to aid in designing the microcantilever heaters. A detailed description on performing COMSOL simulation of Joule heating of microcantilever heater has been given in [47] and [54]. In this section, important considerations for COMSOL simulations are briefly explained.

3.3.1 Electrical resistivity temperature dependence

As discussed previously, the resistivity ρ of silicon, expressed in Equation 3.2, depends on the charge carrier concentration and mobility, both of which exhibit a dependence on temperature. The dependence of electron and hole concentration and mobilities on temperature and dopant concentration, as defined in Section 3.2, were incorporated in the COMSOL model.

Using the temperature dependence of n_i, hole and electron concentrations are plotted in Figure 3.4(a). For reference, n_i is plotted as well and it can be seen that around ca. 1050K (775^{o}C), the values of p, n and n_i are comparable. When p=n=n_i, a criteria that is full filled by intrinsic silicon, the p-doped silicon is said to have become intrinsic. The mobilities vs. temperature plot using the Arora mobility model is plotted in Figure 3.4(b). Using mobility and carrier concentration models, the resistivity as a function of temperature is plotted in Figure 3.4(c). As reference second order model, that uses thermal coefficients of resistance (TCR) as evaluated in [55], is also plotted.

To use the resistivity vs. temperature model, the resistivity (and hence the dopant concentration) at room temperature must be known. Using four point probe setup, the average resistivity of the device layer of SOI was measured to be 0.088 Ωcm for an assumed

device layer thickness of 4 µm provided by supplier. This resistivity corresponds to boron dopant concentration of ca. $3x10^{17}$ cm^{-3}.

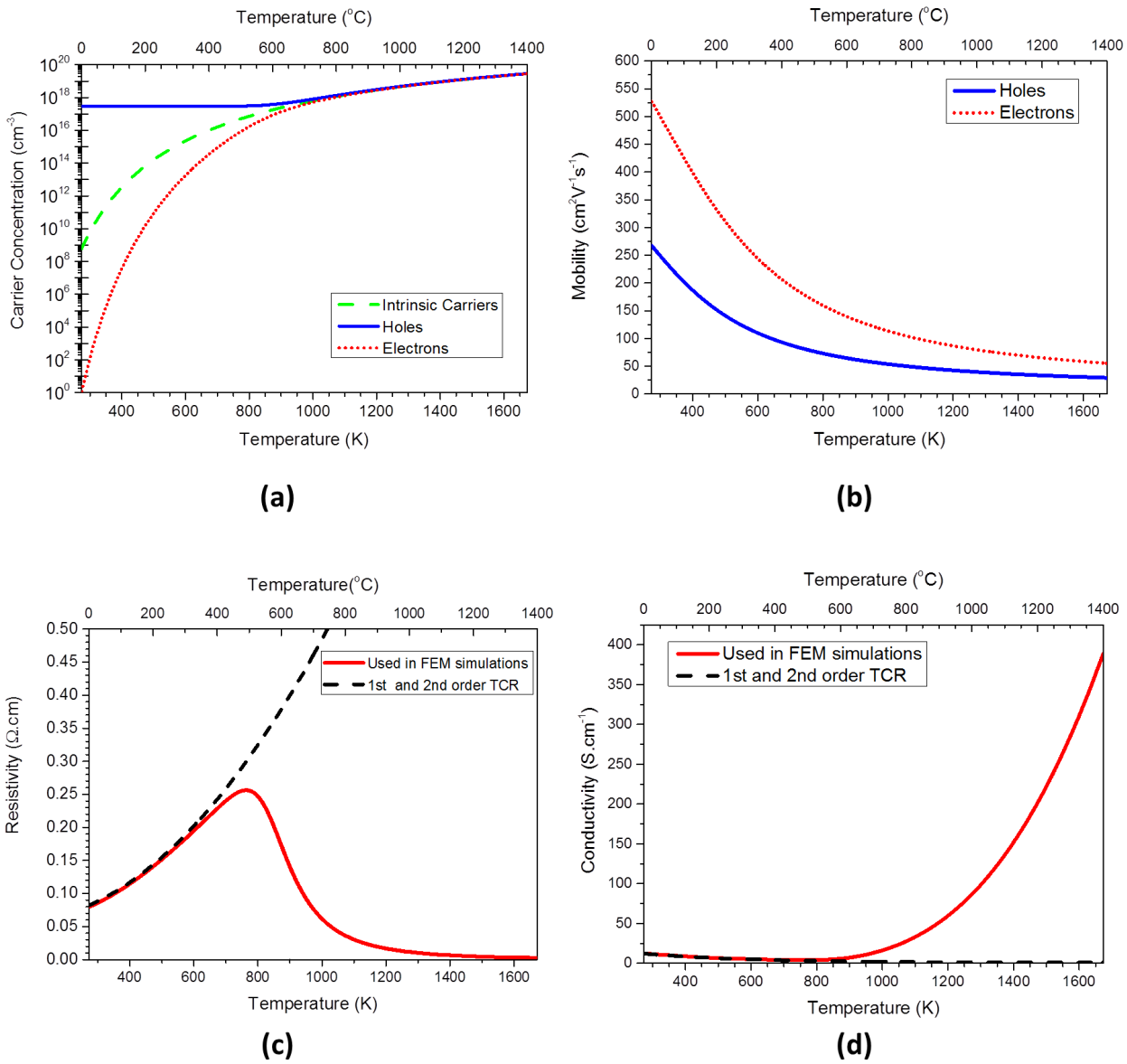

Figure 3.4 Plots presenting the temperature dependence of **(a)** carrier concentrations, **(b)** hole and electron mobility according to Arora model, **(c)** resistivity used in FEM simulations (evaluated using carrier and mobility models in (a) and (b)) and resistivity evaluated using second order TCR model, and **(d)** the corresponding conductivity.

3.3.2 Si thermal conductivity temperature dependence

The thermal conductivity of Si shows strong dependence on temperature and this dependence was accounted for in the COMSOL model. For temperatures higher than 273K, thermal conductivity (k) can be expressed by the empirical formula [56], [57]:

$$k(T) = 2.475 \times 10^5 T^{-1.3} \tag{3.9}$$

Thermal conductivity sets the thermal resistance of the cantilevers, and hence the temperature gradient along the cantilever length. For a small section of cantilever length Δx, thermal resistance (R_θ) is given as:

$$R_\theta = \frac{\Delta x}{Ak} \tag{3.10}$$

where A is the cross sectional area perpendicular to path of heat flow while length Δx is in path parallel to heat flow and it is assumed that k does not change in value over Δx. From Equation 3.10, it can be seen that the thermal resistance of the notches in the cantilever design have a higher thermal resistance.

Understanding the dependence of thermal conductivity is important for contact formation events as well, since thermomigration of Au (Section 5.4.1) depends on the temperature gradient *dT/dx,* which is defined by k and hence, the corresponding absolute temperature.

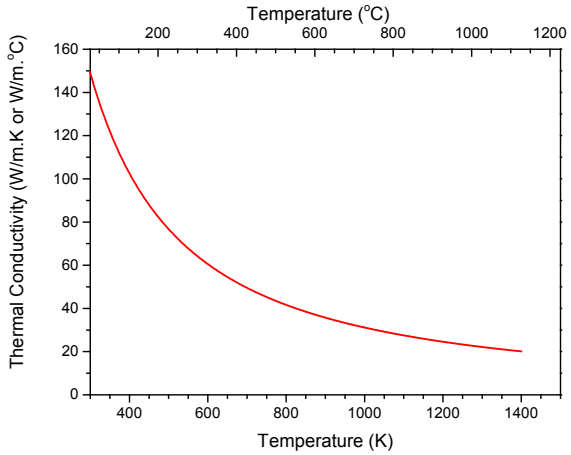

Figure 3.5 Thermal conductivity of Si as a function of temperature.

3.3.3 **Chip heating**

Defining correct boundary conditions is essential for obtaining reliable results from simulations. In simulation of Joule heating of microcantilever heaters, the critical boundary condition that was defined was the average temperature of the chip bulk (Si substrate) as it shifts the microcantilever temperature. Kallesøe et al. [33] estimates the chip temperature to be 75± 25°C/mA for chips of similar design. In this work, the chip temperature was roughly estimated by imagining a path of heat flow, which starts from the cantilever , goes through the underlying oxide layer (k=1.4 W/mK, R_θ=13 K/W), the Si substrate (k=150 W/mK, R_θ=1 K/W), the epoxy EP0-TEK H77 (k=0.88 W/mK, R_θ=125 K/W), the PCB (k=0.3 W/mK, R_θ=150 K/W) and ends at the TEM holder which is assumed to be at room temperature. The total thermal resistance ($R_{\theta\text{-}total}$) is around 290 K/W. For the I-V curve seen in Figure 3.3, the growth temperature (ca. 520°C) was obtained for 32 mW. For the theoretical thermal resistance that

is calculated here, this translates into a chip temperature of 35°C (from Eq. 3.11) and chip heating rate of about 1 °C/mW.

$$T_{chip} = P_{Dissipated} \cdot R_{\theta-total} + T_{room} \tag{3.11}$$

3.3.4 Emissivity

Another parameter that must be accounted for to complete the simulation is the emissivity of the microcantilevers, which is required for estimating heat transfer by radiation. The heat flux for black body radiation scales as T^4 but also depends on the emissivity. For thin silicon layers (about 4μm thin), the emissivity is 1 to 3 orders of magnitude smaller than the bulk silicon value of 0.68 [54]. In the simulations, it is taken to be 10^{-3}. Hence, the black body radiation is significantly reduced for thin microcantilever architecture.

3.3.5 FEM results

Joule heating of the microcantilever was simulated using the data for electrical and thermal conductivity, emissivity and chip temperature boundary condition presented above. There were significant differences in the dimensions of fabricated microcantilevers from chip to chip, in particular the length of the cantilever and their thickness. This meant that a single COMSOL model could not be used for all microcantilever heaters. Figure 3.6, shows the surface temperature for Joule heating current of 1 mA for a microcantilever heater whose dimensions match the heater shown in Figure 4.9.

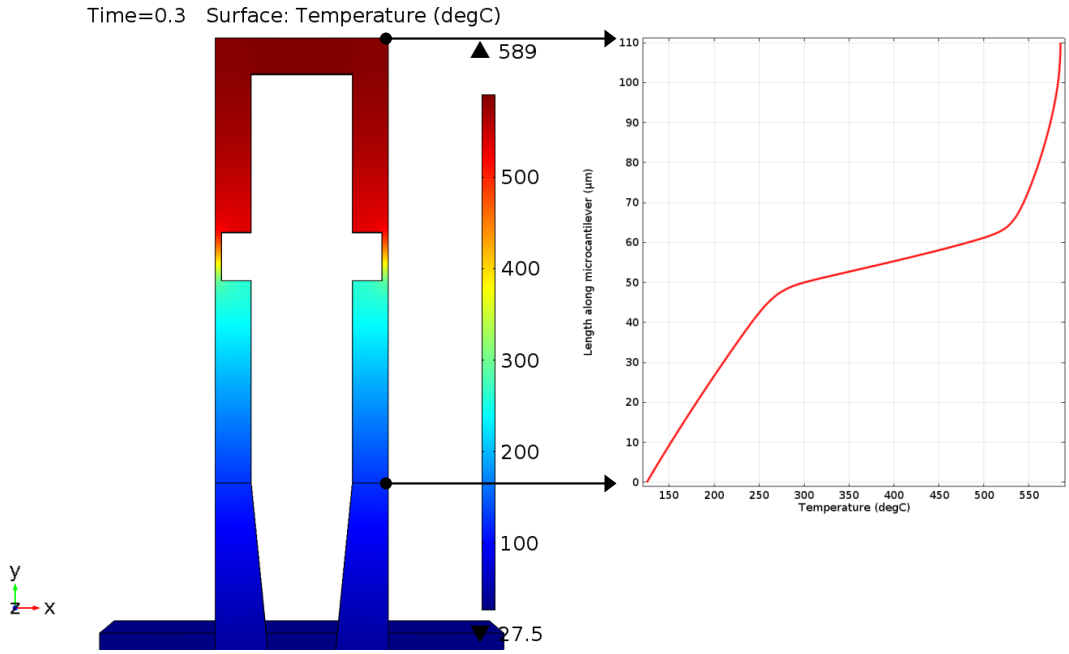

Figure 3.6 FEM simulation result of a Joule heating of a microcantilever heater for 1 mA heating current. The gradient between the tip of cantilever and the start of the notch is 1.2 K/μm, while over the notch the gradient is 14 K/μm.

In the simulation result, the maximum temperature at the tip is 585°C, and the averaged thermal gradient from the tip of the cantilever to the top of the notch is about 1.2 K/μm. From the experimental measurements (using growth rates discussed in the following section), for 1 mA (48.5 mW) current, the temperature at the tip was about 565°C, which is close to expected values (See Figure 3.11, Chip #3 curve). The FEM simulations can give a good prediction of the temperature if the dimensions of the cantilever were well known and the room temperature resistivity is accurately measured.

3.4 **Fabrication**

The microcantilever chips were fabricated using standard microfabrication processes [8]. The complete fabrication process flow is given in Appendix B.

The masks for lithography were designed in L-Edit CAD tool. The chips were fabricated using a process similar to the one used in [33] and [58]. The microcantilevers pattern, defined by UV lithography, was etched (RIE) in the <110> device layer of an SOI wafer (wafer flat is in the <111> direction). The device layer was boron doped with average resistivity of 0.085-0.1 Ωcm. The cantilevers were released by etching the 500 μm thin Si substrate in KOH followed by removing the 500 nm thin buried oxide (BOX) layer in BHF solution.

Dry etching created rough sidewalls for the cantilevers. To circumvent them, the cantilevers were briefly etched in KOH solution, and the {111} planes were exposed. For this purpose, two different KOH etching conditions were tested: Etching in 28 wt% KOH at room temperature for 20 s and etching in 28 wt% KOH at 60°C for 5 s. The latter approach created bigger areas where <111> facets were exposed.

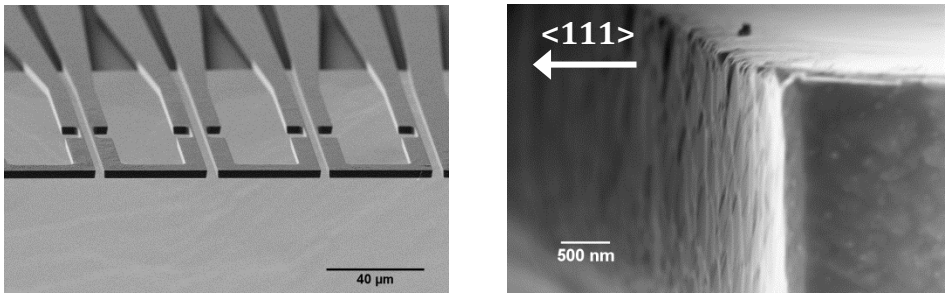

Figure 3.7 SEM image of **(a)** microcantilever heaters and **(b)** zoomed in image of the {111} plane after KOH etch at 60°C for 5 s.

After the chips were fabricated, they were attached to a PCB using EPO-TEK H77 epoxy. The leads between the microcantilevers and contact pads on the chip may not be symmetric for a pair of adjacent microcantilevers. This would have resulted in different spatial voltage profile for the two cantilevers and resulted in substantial current through the wire on contact. To make the resistance of the microcantilever heaters equal, 10 nm of Ti followed by 80-100 nm of Au was deposited over the leads and contact pads through a shadow mask (see Figure 3.8(b)). The BHF under etching of the oxide layer ensures there was no short circuit between

the silicon leads when the gold was deposited by e-beam evaporation. The chips were wire bonded to the PCB. The metallization of the contact pads greatly improved the ability to wire bond successfully. Various chip designs were tested and the design with the cantilevers safely positioned within a hole in the middle of the chip (see Figure A.1) was far more durable when handled in the laboratory compared to earlier designs with the cantilevers sticking out over the edge of the chip (Figure 3.8).

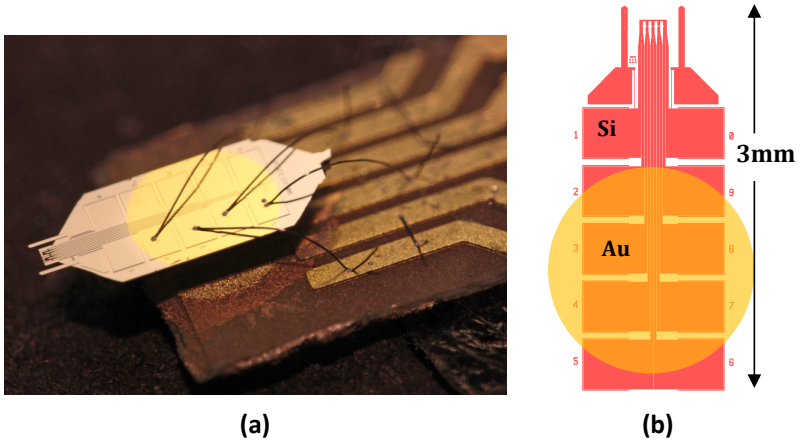

Figure 3.8 (a) Picture of a microcantilever heater chip mounted and wire bonded to a PCB. **(b)** Schematic of the contact pad and lead layout. The coverage of Au deposition is indicated by the yellow circle.

The key issues encountered during the fabrication were: (i) the non-uniform thickness of device layer of SOI wafers, which varied from 3.7 to 4.7 µm over a single wafer, which meant that the etching endpoint detection of RIE system was not effective as some gaps were etched to the bottom BOX layer before the rest and suffered from sideways etching which widened the gap by ca. 1 µm, and (ii) the KOH etching of Si substrate was not accurate, which was expected as etch rate was about 1.5 µm/min and total etching time is ~6 hours. A few tens of minutes of over etching due to wafer thickness variations meant that cantilever loops were not of equal lengths and the cantilever lengths varied from 140 to 153 µm.

3.5 Characterization of microcantilever heaters

A key issue in characterizing microcantilever heaters is to reliably measure the temperature of the fabricated devices. The micrometre scale dimensions of the cantilevers render traditional measurements tools like thermocouples hard to implement. The temperature of the cantilever heaters can be experimentally inferred using techniques like Raman spectroscopy, infrared camera and temperature sensitive resistivity measurements[54].

The variations in the dimensions of the cantilevers from chip to chip translated into variation in electrical resistance of the microcantilevers. Microcantilever heater resistance were recorded to be in a range of 39 to 43 kΩ, though variation in the resistance between two cantilevers on the same chip was less than 1 kΩ . The Joule heating currents, for which stable growth was recorded, were in the range of 0.68 to 0.82 mA (28 to 35 mW respectively). The

large spread in the possible Joule heating currents that gave stable temperatures in the range of 480 to 520°C, meant that each chip had to be calibrated for temperature during experiments. This was accomplished by observing the formation of AuSi eutectic melt at known eutectic temperature of 363°C and by inferring the temperature from the SiNW growth rates at higher temperatures.

3.5.1 Temperature from SiNW growth rates

The growth rate of SiNW depends on temperature and pressure, and has an Arrhenius dependence given by [59]:

$$\frac{dl}{dt} = BPe^{-\frac{E_a}{k_B T}} \tag{3.9}$$

which can be re-written as:

$$T = -\frac{E_a}{k_B}\frac{1}{ln\left(\frac{dl/dt}{BP}\right)} \tag{3.10}$$

where dl/dt is the growth rate in nm/s, E_a is the activation energy, P is the pressure in Torr, k_b is the Boltzmann constant and B is the pre-exponential factor given by nm/s per Torr. Kodambaka et al. [59] fitted the dl/dt vs. T plot for wires grown *in situ* UHV-TEM at a pressure of 1 µTorr to get an activation energy of E_a =0.53±0.02 eV. From[59], B can be evaluated to be 3.78x10^7 nm/sTorr. The growth rate has a linear dependence on pressure (over at least three order of magnitudes, 10^{-8} to 10^{-5} Torr) [59] and hence E_a and B can be used for other pressure values as well by linear scaling.

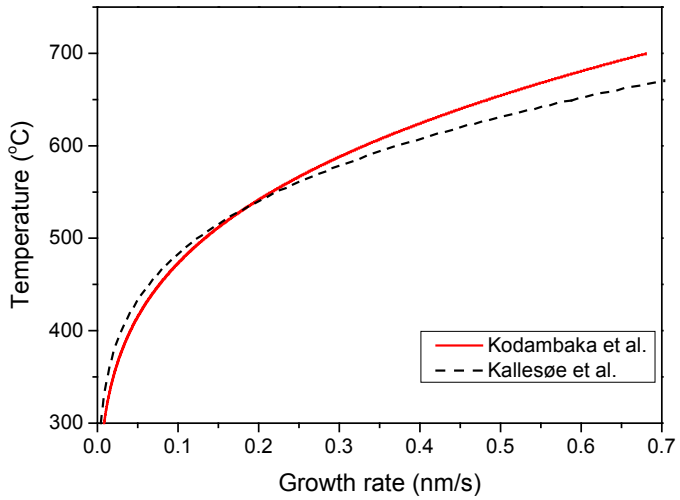

Figure 3.9 Temperature vs. growth rate for disilane pressure of 10 µTorr.

Kallesøe et al. [33] also evaluated the Arrhenius relationship, where E_a of 0.64 eV and B of 1.83x10^8 nm/sTorr was obtained. One likely reason for the different E_a and B values is that Kallesøe et al. experiments suffered from Al contamination in the catalyst. For this reason, in

this work the numbers obtained by Kodambaka et al. were used for temperature calibration through growth rates. For comparison, in Figure 3.9, temperatures vs. growth rates are plotted for E_a and B determined by Kodambaka et al. and Kallesøe et al. As can be seen from Figure 3.9, despite the difference in Arrhenius parameters obtained by Kodambaka et al. and Kallesøe et al., their temperature plots are very similar with a relative difference of about ± 10°C, which was considered to be the uncertainty of measuring temperature from growth rates. Kodambaka et al. [59], used infrared pyrometer for determination of temperature, which had a relative error of ±20°C for the same sample and an absolute error of ca. 50°C. Here relative temperature error is more important as temperature gradients are the driving force in situations like thermomigration. It is also worth mentioning that measuring change in length of the nanowire from recorded videos to determine growth rate can introduce some error due to uncertainty in the measurement. This error was reduced by measuring growth rate over at least 1 minute and preferable 3-5 minutes under stable pressure conditions to get an average rate.

To determine the temperature of contact events, not only the temperature of the impinging wire but also (more importantly) the temperature of the contact surface must be measured. Hence, it was essential to measure SiNW growth rates (and evaluate the temperature) on the receiving cantilever. In the ideal case, the impinging nanowire and the nanowire used for the receiving surface temperature calibration were at symmetrical locations on their respective microcantilevers. Examples of such scenarios are shown in Figure 3.10. When both cantilevers were heated by equal Joule heating current, the temperatures measured from the growth rate of such SiNW pairs were very similar with only ±10°C temperature difference between them. This suggested that the microcantilever heaters, on a given chip, for equal heating current were identical in their temperature profile. Hence, in the case of equal currents, if the contact surface temperature is not known, it can be inferred from the impinging SiNW.

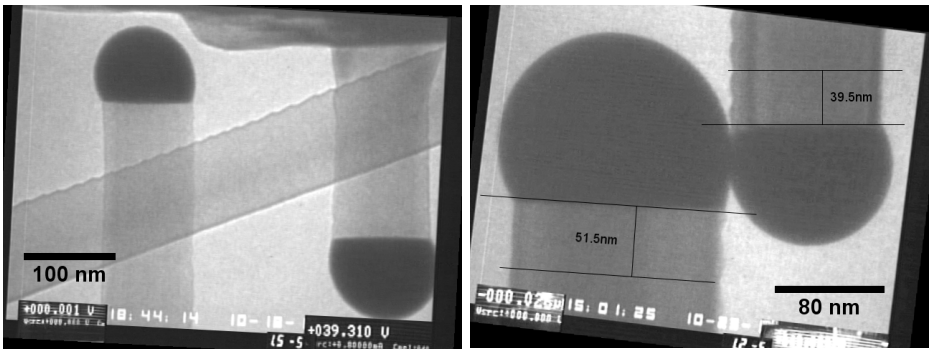

(a) (b)

Figure 3.10 SiNWs growing in symmetric location on their respective microcantilevers are ideal for calibrating the SiNW origin and receiving cantilever temperatures.

Transitions of the Au particle from solid to a liquid AuSi eutectic at 363°C were also used to calibrate the microcantilevers, as these transitions only depend on the temperature and occur at a particular temperature. However, transition from liquid eutectic to solid Au is not reliable due to supercooling effect that was observed, that is, the solid to liquid and liquid to solid transitions do not occur at the same current level as discussed in Chapter 4. From solid to

liquid eutectic transitions, a heating rate of 13±2°C/mW for the cantilever was calculated (cantilevers are at room temperature when no current is applied). The temperature at the tip of cantilevers on three different chips is plotted against the supplied current in Figure 3.11.

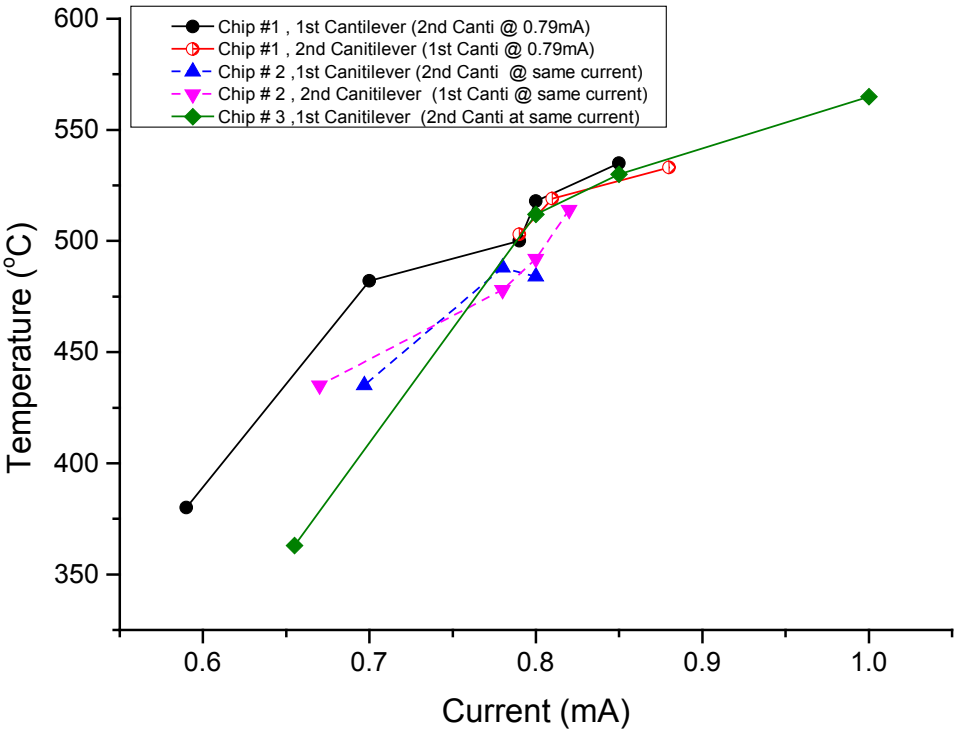

Figure 3.11 Temperature at cantilever tip plotted against current for three different chips. The cantilevers are normally operated between 0.68 to 0.85 mA.

3.5.2 Temperature gradient over cantilever

If the location of the nanowire used for calibration of the receiving surface is further away from the impinging SiNW, then the contact surface temperature T_{ct} must be inferred by using the temperature gradient dT/dx over the cantilever:

$$T_{ct} = T_{WR} \pm L \cdot \frac{dT}{dx} \tag{3.11}$$

where T_{WR} is the temperature of the wire on the receiving cantilever which is a distance L from the SiNW impingement site. Temperature gradient data was evaluated from the COMSOL results and also from experiments by measuring growth temperatures at different location of the cantilever. Figure 3.12 shows the temperature measured from growth rate of two wires, where one wire was located near the tip and the second wire was near the notch. The heating current of the cantilevers was changed and its effect on the temperature and temperature gradient was measured. The gradient was measured to be between 0.2 to 0.75 K/µm. It decreases with decreasing temperatures, which agrees with thermal conductivity plot in Figure 3.5.

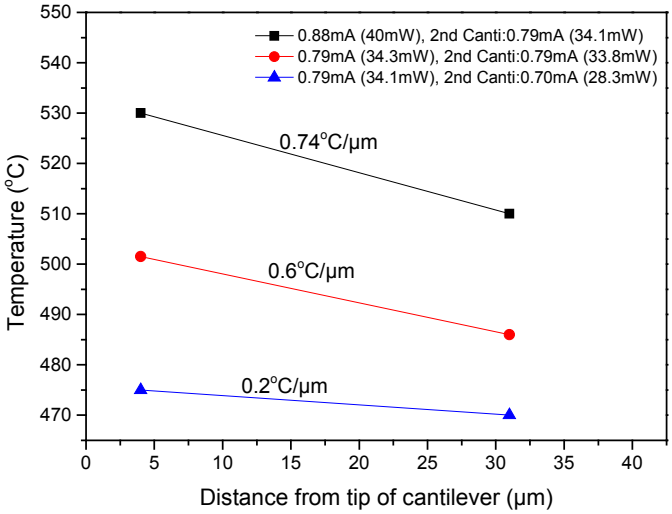

Figure 3.12 Temperature gradients for different heating currents. The effect of chip heating on temperature can be seen by comparing the plots for the case where current of second cantilever is reduced.

3.5.3 **Chip heating**

From Figure 3.12, the chip temperature can be calculated as well. If the two temperature trends for the 0.79 mA (34 mW) current are compared, we see drop in temperature when the adjacent second cantilever current was reduced from 0.79 mA (33.8 mW) to 0.7 mA (28.3 mW). From this, the contribution of second cantilever to chip heating was predicted, which is about 3°C/mW or 170°C/mA, which is much higher than predicted by the simple estimate in section 3.3.3 and [33].

3.6 **Summary**

Monocrystalline silicon microcantilever heaters were fabricated for *in situ* TEM growth of SiNWs. The design of the microcantilever incorporates {111} sidewalls which ensure the SiNW grow perpendicular from these sidewalls and take the shortest distance to reach the adjacent microcantilever heater. To ensure the {111} planes, the last step of the fabrication process was a short etch in KOH solution to ensure {111} facets on the surface of the cantilever structures defined in SOI device layer by RIE process. Low resistance in the leads to the heaters by using a gold coating ensured low chip heating and easy wedge bonding to the metal surface. The notched cantilever design with nanowires growing from the {111} sidewall of the cantilever loop to the side of an adjacent loop proved to be stable platform for contacted nanowires.

The temperature distribution over the microcantilevers was verified using COMSOL FEM tool. The temperature of the heaters was experimentally measure using the SiNW growth rate which has an Arrhenius dependence on temperature. By comparing growth rate of SiNW growing on symmetric locations on the two cantilevers; it was observed that for an equal

Joule heating current, the temperature difference between the two cantilevers is within ± 10^{o}C. Based on COMSOL simulation and experimental measurements, the temperature gradients were estimated that were essential to predict the temperature of the receiving cantilever temperature at the contact site.

4 SiNW growth *in situ* TEM

The VLS mechanism, a metal catalysed CVD process, is the most prominent bottom-up technique for fabricating silicon nanowires [60]. A key difference between VLS growth of SiNWs in conventional CVD reactor to *in situ* UHV-TEM growth is the constraint on the pressure of the precursor gas, which must be kept very low in the TEM for maintaining usable imaging with electron beam. For *in situ* UHV-TEM growth, disilane (Si_2H_6) pressure is usually in the range of 10^{-6} to 10^{-5} Torr, which is 4 to 6 order of magnitude lower than conventional CVD reactors. Low disilane pressure translates into very low growth rates of 5 to 15 nm/min, which are much lower than the µm/min range for CVD reactors. The low growth rates are beneficial as processes related to SiNW growth, which at normal rates would be harder to observe, can be slowed down for examination.

This chapter will introduce basic theory of VLS nanowire growth and present a brief summary of intricate details of the SiNW growth by VLS mechanism, a feat made possible by *in situ* TEM observations [34].

4.1 VLS mechanism – introduction

The VLS mechanism is summarized in Figure 4.1, in which, as an example, formation of an axial Si/Ge nanowire is explained.

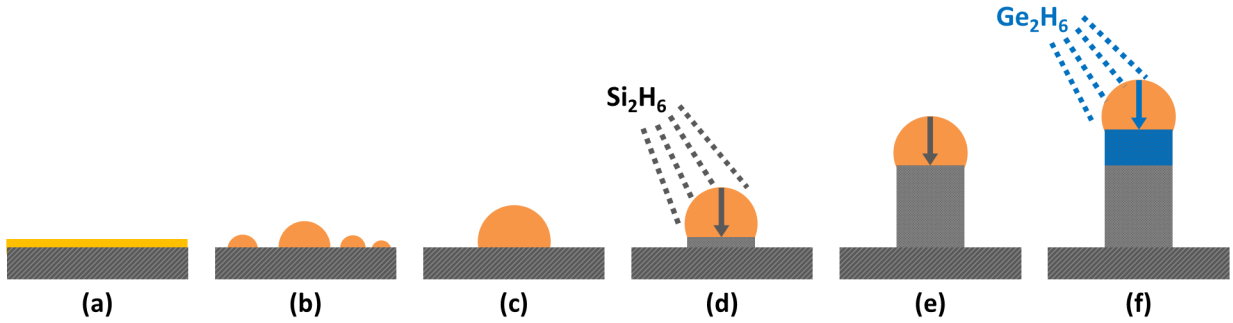

Figure 4.1 Schematic diagram of the VLS process of axial (Si/Ge) nanowire growth from Au: **(a)** Au is deposited on a Si substrate with no native oxide, **(b)** AuSi eutectic droplets containing ca.20% Si are formed when sample is heated above 363°C, **(c)** droplets size can increase by Ostwald ripening; the larger droplets increase in size at the expense of smaller ones, **(d)** exposure to a precursor gas such as disilane which adsorbs preferentially at the droplet surface and supersaturates the droplet with Si, causing Si to precipitate beneath the droplet, **(e)** Si precipitation results in the growth of silicon nanowire, **(f)** axial (heterostructure) nanowires like Si/Ge can be grown by changing the source gas. Adapted from [34].

A thin layer of Au is deposited on an oxide free Si surface which is later heated to above 363^{o}C. At 363^{o}C, Au forms a liquid eutectic alloy with Si, which results in the agglomeration of Au thin film into AuSi eutectic droplets that can increase or shrink in size due to surface diffusion effect of Ostwald ripening. Si required for nanowire growth is supplied in the gas-phase by disilane (Si_2H_6). The disilane precursor gas molecules dissociate at the eutectic droplet surface and Si is preferentially adsorbed by the eutectic. The eutectic droplet becomes supersaturated and Si precipitates. The eutectic droplet continues to absorb more Si which eventually precipitates at the droplet base; with time a column i.e. a nanowire shaped epitaxial platform of Si is formed underneath the droplet.

Heterostructures with varying material composition can also be created and the VLS mechanism for fabricating an axial Si/Ge nanowire is shown in Figure 4.1(f). If the precursor gas is changed to digermane, Ge can be deposited to the nanowire, creating a Si/Ge axial heterostructure nanowire. Similarly, during the growth process, dopants can be incorporated in the nanowire by adding a dopant precursor gas to the reactor. For example, for n-type doping, phosphine is the added precursor gas.

The diameter of the nanowire depends on the dimensions of the catalyst particle. With VLS mechanism, dense arrays of nanowire with diameters ranging from 10 to 100s of nano meters and lengths in several micro meters can be fabricated over an entire wafer. If the catalytic particles are lithographically defined, ordered arrays of nanowires of desired diameter and pitch can be fabricated by VLS mechanism.

4.1.1 **Au-Si binary system**

Figure 4.2 shows the phase diagram (PD) of the Au-Si binary system. A prominent feature of the PD is the eutectic point at 363±3 ^{o}C and corresponding composition of 19±0.5 at% of Si. The eutectic point is significantly lower than melting temperatures for pure Si (1412^{o}C) and Au (1063^{o}C). The phase above the V shaped liquidus line is liquid. The composition of the Au-Si binary system above the eutectic temperature depends on the availability of Si: if Si supply is limited, the composition of the liquid is on the left hand side (LHS) of the eutectic point, while if the Si is abundant – a case true for Si substrates – the composition of the AuSi droplet lies on the Si-rich liquidus line on the right hand side (RHS) of the eutectic point. RHS of eutectic point is where VLS growth regime lies. When a Si precursor like disilane is introduced in the system, Si from the disilane is adsorbed by the AuSi droplet, which results in an increase in the concentration of Si beyond the equilibrium concentration. The new composition of AuSi droplet is thermodynamically unstable and lies slightly on the right of the liquidus line. To regain equilibrium concentration, the droplet precipitates pure Si. By maintaining the continuous supply of Si to the droplet; the non-equilibrium precipitation process can continue to create an epitaxial nanowire.

When the temperature is slowly lowered below the eutectic point (363^{o}C), solid Au and Si will precipitate out, each containing trace amount of the other material. If AuSi droplet with composition of, for example, 40 at% of Si is cooled; this alloy will follow the liquidus line and only precipitate Si until it reaches the eutectic temperature [9]. On further cooling, Si and Au will segregate from each other.

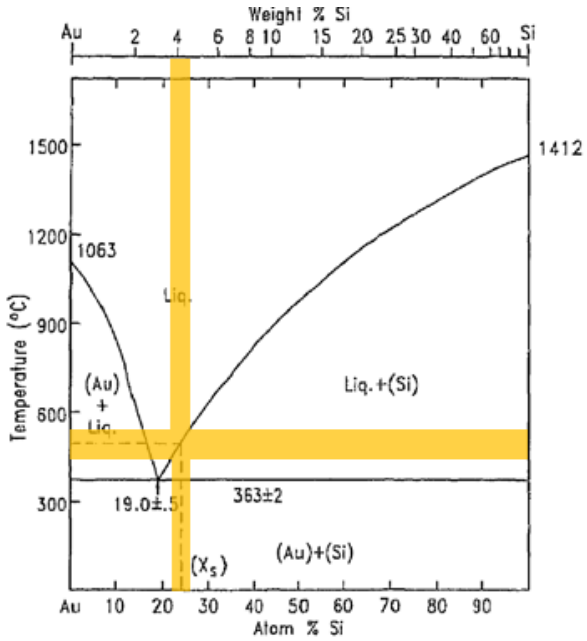

Figure 4.2 Phase diagram of Au-Si binary system. The yellow strips indicate the nanowire growth temperature range in this work, which is 450 to 550°C and corresponds to ca. 22 to 26 atomic % of Si. Adapted from [61].

Growth temperatures in this work were from 450 to 550°C, which for AuSi eutectic in Si-rich regime correspond to a composition of 22 to 26 at% of Si. In the following chapters, it will be seen that most analysis of contacts was done by calculating eutectic volumes and hence knowing composition of eutectic in volume percentage is important. Here, an assumption is made that the volume of Si and Au atom in the eutectic is similar; thus atomic percentage of Si was assumed to be equal to volumetric percentage of Si in the eutectic. This is a good enough estimate as the size of Au and Si atom is comparable (the metallic radius of Au is 144 pm, while Si is 138 pm) and given that the density of the eutectic matches a weighted mixture of Si and Au [62].

4.2 SiNW growth in TEM – experimental setup

In order to be able to grow epitaxial SiNWs, it is critical to remove the native oxide from the silicon microcantilevers. The first step, after wire bonding the sample to the TEM holder, was to remove the native oxide by etching it in 10% HF vapour for 10 minutes. After oxide removal, the sample was immediately (within 5 minutes) transferred into the load lock. The sample was left in the TEM load lock under vacuum, where it was also baked at 100 to 150°C, under a tungsten lamp, for several hours (preferably overnight) to degas and remove moisture. Later the sample was transferred to the Au evaporator housed in the sample preparation chamber section of the TEM without breaking the vacuum; thus maintaining an oxide free surface. Using the Knudsen cell evaporator, less than 5 nm of Au was deposited on the top and bottom of the cantilever chip at a grazing angle (about 10-15°) to ensure Au

coverage on the cantilever sidewalls. Sufficient Au coverage was essential for non-tapering "healthy" wire growth.

The sample was finally transferred to the TEM column, and the heating current was applied to the two microcantilevers in the presence of disilane gas. Usually, growth temperatures between 450 to 520^{o}C were set on the cantilever to initiate nucleation. The setup was left at growth temperatures for 20-30 minutes before the transitions of Au into droplets, which Ostwald ripens over time and form AuSi eutectic droplets, were observed.

The disilane pressure was kept around $5x10^{-6}$ to $2x10^{-5}$ Torr and an average growth rate of 10 ± 5 nm/min was observed. The SiNWs of interest were the ones that traversed the gap between the two adjacent cantilevers (Figure 1.2) and reached the sidewall of their opposing cantilever. The gap size between the cantilevers varied from 2.3 to 3μm, which meant several hours of growth were required before SiNWs reached the receiving cantilever sidewall.

4.3 Initial coarsening of AuSi eutectic droplets

By heating Au covered Si surface to above 363^{o}C, the thin layer of Au is transformed into a distribution of small AuSi eutectic droplets. If the annealing is continued, some droplets can become bigger on the expense of smaller droplets by the process of Ostwald ripening (OR). OR is a thermodynamically driven spontaneous process that occurs because larger droplets, with lower surface to volume ratio, are more energetically stable than smaller ones. This is because the atoms on the surface of a droplet are energetically less stable than the one packed in the bulk and atoms from smaller droplets will migrate to larger droplets to reduce the surface area of the system. The internal pressure of the droplet is a good guideline to determine if coarsening is thermodynamically favourable or not. The internal pressure of the eutectic droplets is given by Young – Laplace equation, which links pressure difference (ΔP) between internal and external pressure to surface tension (γ) and radii of curvatures R_x and R_y (in orthogonal directions) as:

$$\Delta P = \gamma \left(\frac{1}{R_x} + \frac{1}{R_y} \right) \tag{4.1}$$

For spherical surfaces, such as droplets, R_x=R_y=R and Equation 4.1 can be written as:

$$\Delta P = \frac{2\gamma}{R} \tag{4.2}$$

From Eq. 4.2, it can be seen that the internal pressure of the droplet increases with decreasing radius R. For small energetically unfavourable AuSi eutectic droplets, Au will detach from the droplet and diffuse through the surface and then attach to surface of the larger droplet. Diffusion through the surface is possible because the <111> Si surface in the SiNW growth system has a surface coverage of 1 monolayer of Au [63]. The concentration gradient of Au around the interface of the shrinking and growing droplets will define how fast the coarsening can take place if it is not limited by detachment/attachment of Au atoms.

4.4 Growth kinetics for SiNW growth

According to Givargizov [64], there are four rate limiting factors in VLS growth of SiNWs:(i) mass transport in the gas phase, (ii) chemical dissociation of disilane at gas-liquid interface, (iii) diffusion through the liquid eutectic and (iv) incorporation of Si from eutectic into the solid. Kodambaka et al. [59] presented that for SiNW growth, the sole rate limiting step is the thermally activated Au-catalysed adsorption of disilane directly on the catalyst droplet. Kodambaka at al. [59] has summarized the activation energies to overcome all these steps in one E_a value of 0.53 eV, and the Arrhenius curves have already been presented in Figure 3.9.

4.4.1 Temperature dependence

This has been discussed in Section 3.5.1, where the Arrhenius dependence of growth rate on temperature was used to calibrate the temperature of the microcantilever heaters.

4.4.2 Diameter dependence

A consequence of rate of growth being limited by incorporation of Si from the vapour into the AuSi eutectic is that length growth rate *dl/dt* are independent of diameter [59]. Though Kallesøe [32] did notice some variations in growth rate with diameter but not significant compared to the uncertainty of the measurements.

In this work, some variation in growth rate was expected over the cantilevers which have a thermal gradient. For wires growing in symmetric locations on opposing sidewalls (See Figure 3.10), despite variations in diameter, similar growth rates were recorded. It must be remembered that volumetric rate of deposition are strongly dependent on wire diameters and there could be variations in the individual cantilevers dimensions after fabrication translating into difference in temperature, but nevertheless similar growth rates were observed when similar currents were applied. This indicates a fairly reproducible temperature distribution in the two cantilevers in the devices and independence of growth rate from wire diameters.

4.4.3 Pressure dependence

In [59], SiNW growth was measured at a fixed temperature over pressures ranging from 10^{-8} to 10^{-5} Torr, and it was shown that *dl/dt* has a linear relationship with pressure. This observation implied that the sticking probability *S* is independent of pressure and has a value of about 0.1 at T=575^{o}C as evaluated by Kodambaka et al. [59]. The sticking probability *S* is the probability that disilane molecules impinging on the AuSi eutectic droplet are trapped on surface and adsorb to dissociate chemically. It can be shown that the sticking probability *S* is represented in the prefactor *B* in Equation 3.9 and is defined as:

$$S = \frac{Si\ atoms\ incorporated\ in\ the\ SiNW\ per\ unit\ time}{Si_2H_6\ molecules\ impinging\ on\ the\ AuSi\ droplet\ per\ unit\ time} \tag{4.3}$$

which can be expressed quantitatively as

$$S = \frac{\left(dl/dt\right) A_{NW} N_{Si}}{2F A_{drop}} \tag{4.4}$$

where *dl/dt* as mentioned in Section 3.5.1 is the growth rate, A_{NW} is the cross sectional area of the SiNW, A_{drop} is the surface area of the AuSi eutectic droplet, N_{si} is the atomic density of Si, which is about $5x10^{22}$ atoms/cm^3 . The factor 2 is present as each disilane molecule has two Si atoms. *F* is the disilane impingement rate, i.e. the number of disilane atoms impinging per unit area per unit time and is given as:

$$F = \frac{P}{\sqrt{2\pi m k_b T_{RT}}} \tag{4.5}$$

where *P* is the pressure, *m* is the mass of disilane molecule, k_b is Boltzmann constant and T_{RT} is the room temperature. The mean free path of disilane molecule is much larger than the TEM column and hence the temperature of the gas is taken to be room temperature T_{RT}. Re-writing Equation 4.4 after inserting Equation 4.5:

$$\frac{dl}{dt} = 2\frac{A_{drop}}{A_{NW}} \frac{P}{N_{Si}\sqrt{2\pi m k_b T_{RT}}} S \tag{4.6}$$

The growth rate of SiNW depends on temperature as defined by Equation 3.9. This implies that the sticking coefficient must have a dependence on temperature of the form:

$$S(T) = I_o e^{-\frac{E_a}{k_b T}} \tag{4.7}$$

where I_o is defined as the incorporation coefficient which summarizes not only the temperature variation of the sticking probability but also disilane dissociation and Si precipitation in one term. The value of I_o was evaluated to be 115 and S was found to be ~0.05 at 520^{o}C. Combing Equation 4.6 and 4.7,

$$\frac{dl}{dt} = 2\frac{A_{drop}}{A_{NW}} \frac{P}{N_{Si}\sqrt{2\pi m k_b T_{RT}}} I_0 e^{-\frac{E_a}{k_b T}} \tag{4.8}$$

Comparing Equation 3.9 with 4.8, the pre-exponential factor *B* is related to sticking probability through the equation:

$$B = 2\frac{A_{drop}}{A_{NW}} \frac{I_0}{N_{Si}\sqrt{2\pi m k_b T_{RT}}} \tag{4.9}$$

The wires approaching the cantilever will see part of the disilane flux being blocked by the cantilever, which being about 4 μm thick is much larger than nanowire diameter. The ballistic moving disilane molecules are, however, not adsorbed by Si and will "bounce off" the

cantilever. Thus, only very close to the cantilever, of the order of nanowire diameter, there could be decrease in growth rates if the sticking coefficient is large, but it is in fact around 0.1.

4.5 Structure and composition of SiNW

SiNWs predominantly grow in the <111> crystal direction with hexagonal cross section, with alternating wider and narrower sides, and {11$\bar{2}$} sidewalls. The {11$\bar{2}$} sides of the SiNW show periodic sawtooth facets as shown in Figure 4.3 [65]. The sawtooth facets are at an angle to the <111> growth direction, the smaller facet is {111} while the longer facet is {113}. In Figure 4.3(c), the period (p) and amplitude (h) of the oscillating facets depends on the wire radius and have been estimated by Ross et al. [65]. The period (p) of the sawtooth facets of wire of radius r_{nw} is about $0.45r_{nw}$ and amplitude (h) is about 0.14p [65].

The sawtooth faceted sidewalls of the SiNW grown in UHV-TEM have a significant amount of Au coverage. Wiethoff et al. [66] estimated the mean Au coverage to be 0.4 - 0.46 monolayer or 3.1-3.6x10^{14} atoms/cm^2. The majority of Au is located on the smaller {111} facets. The facets on the sidewall of SiNW are believed to be induced by the Au coverage [65], [66].

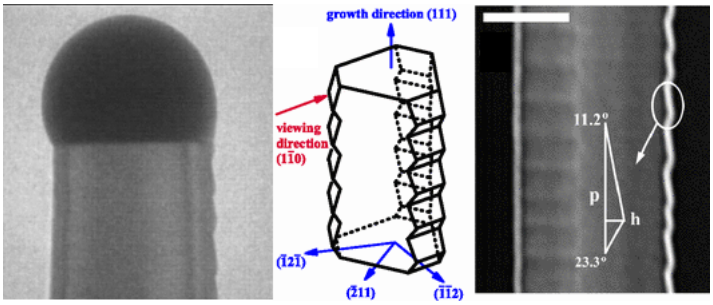

Figure 4.3 (a) TEM image of SiNW with sawtooth facets , **(b)** schematic of the 3D structure of a wire and **(c)** TEM images indicating the period p and amplitude h of the facet and the angles. Reproduced from [65].

As a SiNW grows, Au is continuously lost from the catalyst droplet to form the monolayer on the wire sidewall facets. Hence, how long the SiNWs can grow is limited by the relation between the Au coverage and the catalyst droplet volume. As the Au is transferred to the sidewall, the droplet volume will shrink to a point where it is completely consumed and the growth terminates. Hannon et al. [63], defined that the droplet will be compelelty consumed when the nanowire of radius r_{nw} reaches the critical length l_c, given as:

$$l_c = \frac{r_{nw}^2}{2a\theta} \tag{4.10}$$

where a^3 is the atomic volume of Au (a≈0.26 nm) and θ is the average coverage of Au on the sidewalls. For the estimated Au coverage of 0.4 monolayer, the maximum attainable length before the catalyst is consumed for a wire diameter of 40 nm is ~ 2 µm. This agrees with

finding in this work, where the minimum gap between the cantilevers was 2.3 μm and wires below 40 μm were not able to grow long enough to traverse the gap. Equation 4.3 sets design criteria for setting the gap dimension. The growth may terminate before reaching critical length l_c due to OR, which is discussed in the following section and was most likely the reason some wires tapered and growth terminated before the length l_c was reached.

A feature common to all VLS grown SiNWs is the expansion of the nanowire base during the initial stages of growth [60]. Figure 4.4(a), shows the intial configuraiton of an AuSi droplet on Si surface. Figure 4.4(b) to (d) shows time sequece of SiNW at the stage when the first sawtooth facets were being created. It can be seen that the base of the wire is wider than the wire diameter above the first sawtooth. The widening of the base is due to the tranistion of the droplet shape in the initial phase of wire growth [60]. This transition of droplet shape is related to a change (increase) in contact angle. For comparison, Figure 4.4(a) showing the droplet in the very begining of wire growth has contact angle of about 60^o,while for Figure 4.4(b), the contact angle of the droplet is ~120^o.

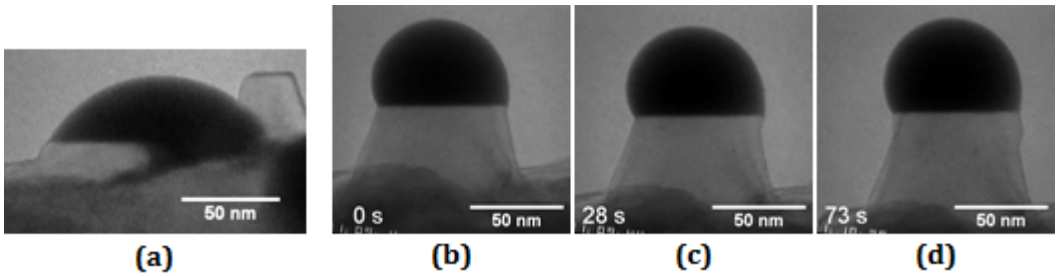

Figure 4.4 (a) AuSi droplet in initial phase of SiNW growth, **(b)-(d)** Growth of the first sidewall sawtooth facet. The SiNW base is wider than the wire diameter.

Though SiNW preferentially grow in <111> direction, introduction of oxygen can change the growth direction to <110> [67]. It was observed that the growth direction *in situ* UHV-TEM could also be changed by cooling and restarting growth, which could destabilize the catalyst droplet riding at the tip of the nanowire causing it to partially wet one of the sidewall facets of the wire (most likely {111} surface). Restarted growth would create a kinked wire.

4.6 Tapering and termination of SiNW growth

In addition to surface incorporation of Au from the catalyst droplet, OR process can also cause wire tapering. Au coverage on sidewalls of the SiNWs and the microcantilevers enables Au to migrate over the surface of the microcantilever and also up and down the SiNW [63]. Driven by OR, Au preferentially migrates from smaller to bigger droplets, which causes the catalyst droplet volumes to change over time during growth. This results in wider wires to get wider as their AuSi eutectic droplet volume increases, while the neighboring wires which are losing Au to the wider wire will taper [63]. Figure 4.5(a) shows a group of SiNWs growing on the opposing sides walls, where the diameter of SiNW growing on the bottom cantilever has gradually increased to more than double its initial value (from ca. 60 to 130 nm) due to OR.

The wires that get wider usually do so at the expense of neighbouring wires. Figure 4.5(b) shows the time sequence of tapering process in which the catalyst droplet shrinks as Au diffuses away by surface migration. Growth of the SiNW terminated when the entire droplet was consumed.

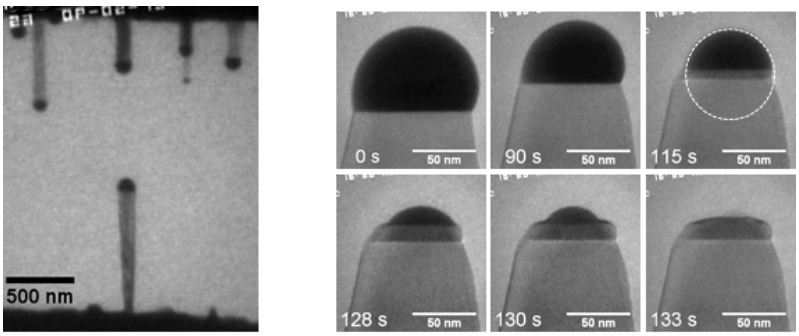

Figure 4.5 Examples of Au migration to and away from the AuSi droplet. **(a)** The diameter of the SiNW (at the bottom) is increasing due to continuous addition of Au to the catalyst droplet by OR. **(b)** Time sequence of the tapering and termination of SiNW growth due to loss of Au which is migrating from the catalyst droplet, scale bar is 50 nm.

The kinetics of the tapering process is plotted in Figure 4.6, in which it can be seen that the growth rate of Si increases at a much higher rate in the final stage before termination. The rise in the growth rate was due to the fact that as the Au migrates away, the remaining eutectic maintains its AuSi composition defined by the liquidus line in PD and deposited the excess Si to the wire. This second source of Si, in addition to disilane, increased the growth rate.

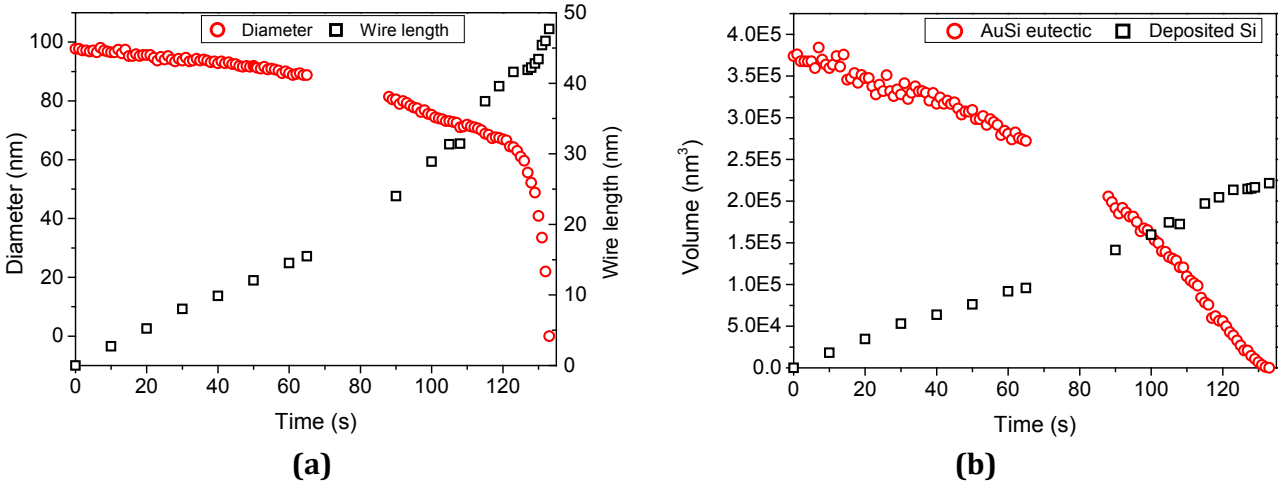

Figure 4.6 (a) AuSi eutectic droplet diameter and wire length plotted against time. The increase in *dl/dt* at the final stages can be seen. **(b)** Volume of AuSi eutectic droplet and deposited Si as function of time.

Volume of Si that segregates from the shrinking eutectic can be calculated easily as volume percentage of Si in the eutectic can be estimated from the PD. While the contribution to

deposited Si from dissociation of disilane gas (VLS mechanism) can be estimated if, ϑ, the volumetric rate of Si deposition (dV_{Si}/dt) per surface area of eutectic droplet (A_{drop}) is known. From Equation 4.6, it can be written:

$$\vartheta = \frac{d^2V_{Si}}{dA_{drop}dt} = 2\frac{P}{N_{Si}\sqrt{2\pi m k_b T_{RT}}}S \tag{4.11}$$

where $dV_{Si} = A_{NW}dl$. For the tapering wire in Figure 4.5(b), the temperature was ~560°C and disilane pressure was 8 μTorr. The volumetric rate of Si deposition per surface area of the eutectic droplet was evaluated to be ϑ=0.061 nm^3 per nm^2 per second (nm/s). With known ϑ, the Si deposited from the gas phase can be estimated. The observed volume of silicon deposited as function of time matched the volume obtained by combining eutectic segregation due to Au migration and the continued silicon supply from the disilane gas through the eutectic surface area, as shown in Fig 4.7. For the tapering wires, eutectic segregation provided about 10-50% of the disilane contribution.

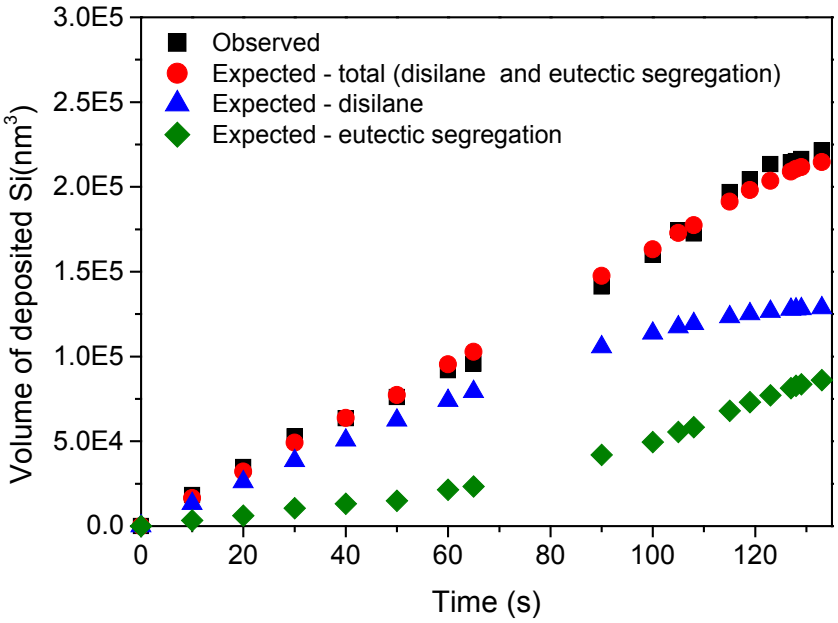

Figure 4.7 Observed and expected volume of deposited Si as function of time.

The droplet decay involves three steps (i) detachment of the Au from the AuSi droplet, (ii) diffusion over the SiNW and microcantilever surface and (iii) attachment to a larger droplet elsewhere. The internal pressure of the Au droplet can be inferred from its radius of curvature. The radius of curvature is determined by matching a circle to the droplet shape as shown in Figure 4.5(b) for t=115 s mark. The corresponding internal pressure of the droplet is then evaluated using Equation 4.2, where surface tension for AuSi droplets is taken to be 1.22 J/m^2 [68]. The increase in the internal pressure of the droplet does show correlation to the change in slope of the volume vs. time plot. The average dV/dt from 0 to 40 s is about 1400 nm^3/s which increased to ~3500 nm^3/s for t=88 to 100s. Indicating that droplets will shrink faster as they grow smaller.

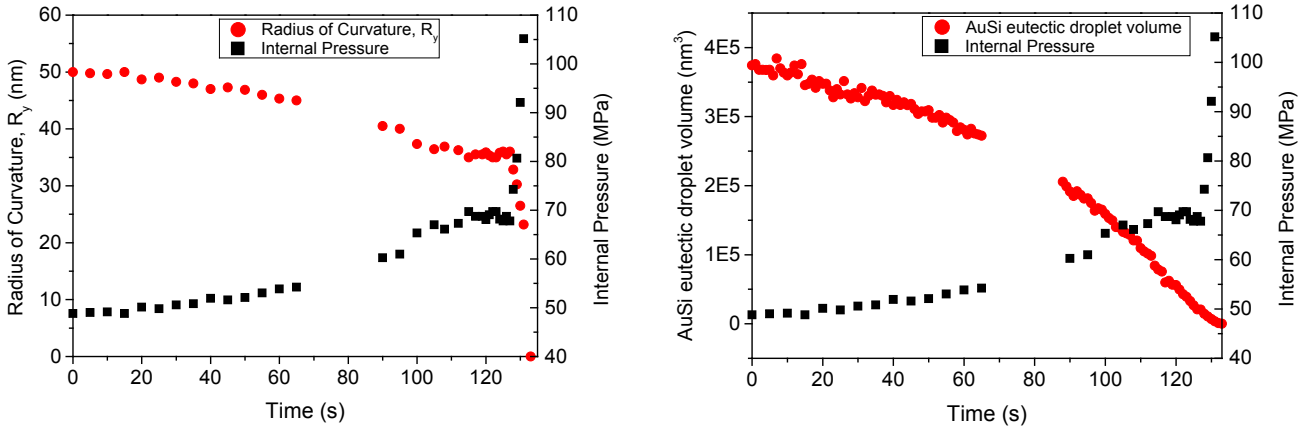

(a) **(b)**

Figure 4.8 (a) Radius of curvature and internal pressure of AuSi eutectic droplet plotted vs. time. **(b)** Volume and internal pressure of droplet vs. time plot.

4.7 Influence of electromigration of Au on growth

In addition to OR, electromigration can drive Au surface migration over SiNW sidewalls and the microcantilever surface. By examining the wire density over the microcantilever heater, in Figure 4.9 (and Figure A.3), the effect of electromigration on Au diffusion and hence wire growth can be concluded.

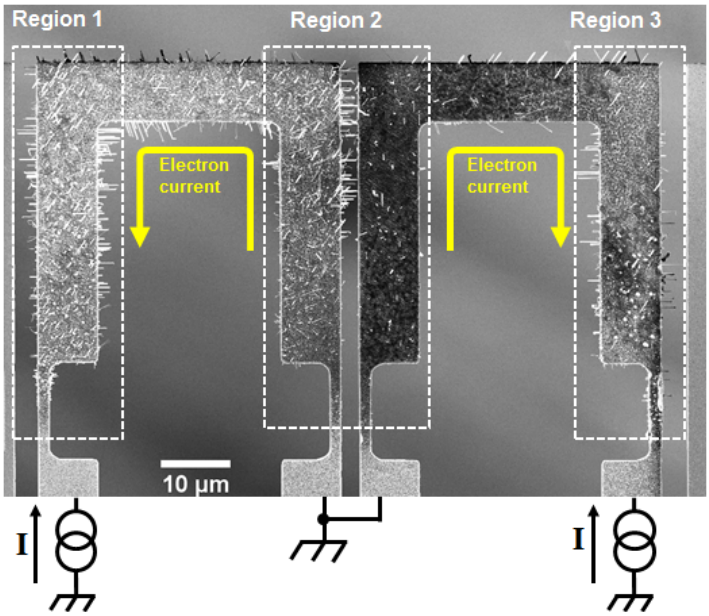

Figure 4.9 Microcantilever heaters with SiNWs grown on them. The cantilever heaters were operated by constant current source as shown by the connections. The direction of the electron current is opposite to the conventional current. The more common configuration used in experiments is given in Appendix A, Figure A.3.

The direction of electron current is opposite to the conventional current of positive charge as indicted in Figure 4.9. The experiments conducted on electromigration of Au are discussed in Chapter 6, where it is demonstrated that the migration of Au is in the direction of electron current. An observation also reported in [69]. At growth temperatures, electromigration rate of Au was high enough for the electron current to transport Au from one end of the hot microcantilever towards the other in the timespan of the growth experiment which lasted for several hours. The microcantilever chip in Figure 4.9 was operated at 0.8 mA for the left cantilever and within range of 0.8 to 1 mA for the right cantilever loop. The corresponding current densities through the different section of the loop are summarized in Table 4.1.

Table 4.1 Current density through different sections of microcantilever heater

Section	Cross sectional area (μm^2)	Current density at 0.8 mA ($\mu A/\mu m^2$)	Current density at 1 mA ($\mu A/\mu m^2$)
Notch	7.6	105	131
Upper loop above notch	34.8	23	29

Electromigration will transport Au in the direction of electron current i.e., away from the grounded terminal and towards the positively biased output of the constant current source. This resulted in gradual depletion of Au in notches and legs of the microcantilever that were connected to the ground terminal. This can be observed in Figure 4.9, in which there is a stark difference in the density of wires growing in Region 1 and Region 3 to lower section of Region 2. Region 1 and upper part of Region 2 have a wire density of about 1 wire per 2 μm^2. However, the sidewalls of the cantilever in Region 2 at and above the notch have relatively lower wire density. This is because electron current is driving the Au from Region 2 towards Region 1 and 3. The migration of Au by electromigration will stop beyond the notch structures due to decrease in temperature to below eutectic point closer to the chip body as shown in Figure 3.6. To ensure maximum number of wire grew in the gap between the two microcantilevers; the electron current direction was set towards the gap as shown in Figure A.3.

4.8 Supercooling in AuSi eutectic droplets

During heating, the transformation of solid Au island into AuSi liquid eutectic droplet at the known eutectic temperature of 363±5^{o}C provided a reliable data point for calibrating the temperature of the microcantilevers. On cooling the AuSi droplets, supercooling was observed, that is, the AuSi droplets remained liquid below the eutectic temperature. Supercooling is the process in which a liquid is cooled below its freezing point without it becoming solid. Supercooling in AuSi eutectic droplets is a known phenomenon [62]. The degree of supercooling of AuSi eutectic droplets depends on the substrate surface in contact

with it and the thermal history [70]. When the AuSi island is sufficiently cooled, the AuSi island will solidify, and Si will segregate as can be seen in Figure 4.10.

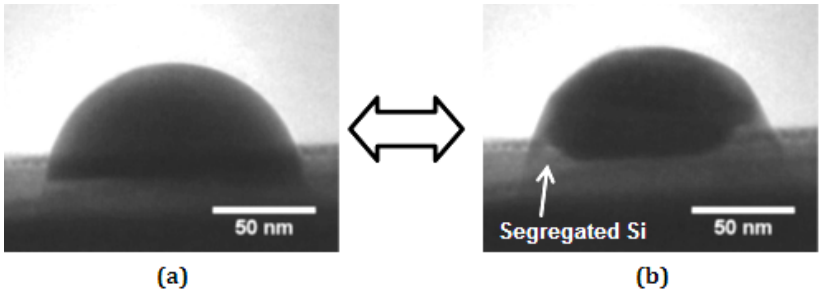

Figure 4.10 Transformation from **(a)** liquid AuSi eutectic droplet into **(b)** Au solid particle. The Si that segregated from the eutectic and is dumped is indicated by an arrow. Supercooling is observed in this system, i.e. transition from solid to liquid occurs at a higher temperature than solidification.

During the cooling down cycle, the solidification of AuSi droplets occurred at temperatures 40 to 180°C less than eutectic temperature. The solidification temperature was interpolated by assuming the temperature followed a linear trend with respect to electrical power between eutectic and room temperature. Solidification temperature (T_S) was evaluated as:

$$T_S = \frac{\Delta T}{\Delta P} P_S = \left(\frac{T_E - T_{RT}}{P_E - P_{RT}}\right) P_S \tag{4.12}$$

where P_S is the electrical power supplied to the cantilever at solidification temperature and T_E is the eutectic temperature achieved by supplied power P_E. T_{RT} is room temperature at supplied power P_{RT}, which is zero Watts. Since, the second cantilever was not heated; the effect of chip heating by second cantilever does not apply.

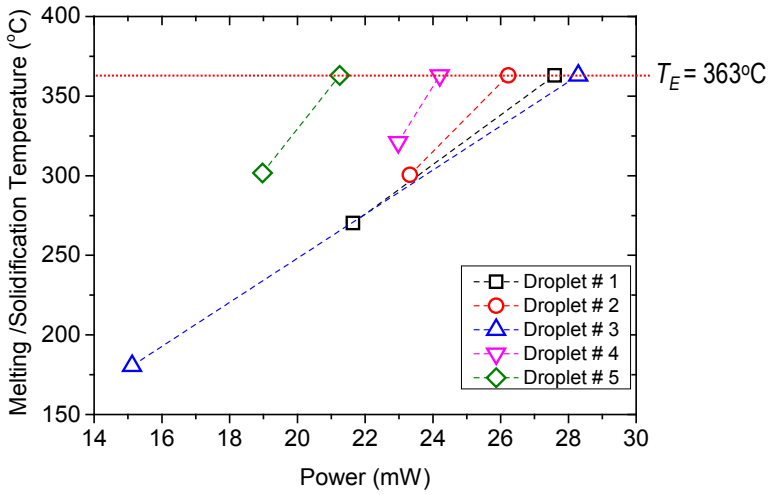

Figure 4.11 Eutectic temperature and solidification temperature for five different AuSi droplets on different microcantilever heaters. The eutectic temperature T_E is indicated by the horizontal line at 363°C, while the data points below T_E marker line are solidification temperatures when cooling down the droplets.

The solidification temperature for five different droplets, evaluated by Equation 4.12 is shown in Figure 4.11, which as can be seen are below the eutectic temperature. The data is presented for five different droplets on five different cantilevers, when the second cantilever is cold.

4.9 Summary

The VLS mechanism, with AuSi eutectic droplet as the catalyst and disilane as the gas phase source of Si, was used to grow epitaxial SiNWs *in situ* TEM. The growth rate of SiNWs has an Arrhenius dependence on temperature, linear relation to disilane pressure and is independent of wire diameter. The SiNWs usually grow in the <111> direction and have hexagonal cross sections. The sidewalls of the SiNWs have periodic sawtooth facets and 0.4-0.46 monolayer of Au over the surface. The source of Au on the SiNW sidewall is AuSi catalyst droplet. Hence, the length of the wire is limited by the volume of the AuSi droplet: as the wire grows, Au is transferred to surface from the shrinking catalyst, which if entirely consumed results in termination of growth.

The surface of the cantilevers is also covered by Au, one monolayer thin in case of {111} sidewalls. The Au coverage over the SiNWs surface and cantilevers enabled Au to migrate to and from the AuSi droplets during growth by Ostwald Ripening process. This results in wires with large diameter getting even wider at the expense of neighbouring thinner wires which lose their Au to the larger wires and tapper due to shrinking droplet. Growth rate of tapering wires increase closer to growth termination because as the Au migrates away, the segregated Si is deposited at the SiNW tip.

Electromigration of Au driven by the current flowing through the microcantilever heater also effects the SiNW growth and can cause tapering/widening of wires. Au migrates in the direction of electron current, which translated into higher density of wires on the cantilever legs which are connected to the positive terminal of the current source.

5 SiNW contact geometries

Integration of SiNWs in devices requires that electrical, thermal and mechanical contacts with desired properties can be established between the nanowire and the microscale architecture of the devices. For example, for SiNW based biosensors, the transducible property is the electrical conductance, which should be measured reliably without hindrance from the geometry of the contact structure. For integration of VLS SiNWs in device design, it is essential to have a comprehensive understanding of their self-assembled contact mechanism; an achievable task with the aid of *in situ* TEM.

This chapter will present real time observations, made using *in situ* TEM, of the VLS SiNW contact formation process. With *in situ* TEM, the kinetics of the formation of freely suspended self-assembled SiNW contacts can be observed in detail and the effect of adjusting the conditions of the contact region on the contact formation mechanism can be studied in real time. The main aims of this chapter are, first, to investigate what possible new SiNW contact geometries can be created by CVD method and what are the conditions required for their creation. Secondly, to find out what physical mechanisms determine the contact structure, although many competing process can make a clear answer difficult to achieve.

This chapter begins by a brief review of literature available on contact formation mechanism. This is followed by presenting the experimental setup used in the UHV-TEM to fabricate and control SiNW contact geometries. Theory of factors that will influence the VLS SiNW contact formation process are then discussed, wherein a methodology to analyse the experimental results is also established. Then, the experimental results are presented and, for different contact geometries, the fabrication method and kinetics are analysed. The chapter concludes by identifying the best method to create controlled contact geometries. Those conclusions are presented in the paper in Appendix E.

5.1 Literature review

To the best of author's knowledge, apart from Kallesøe et al. [25], only Sharma et al. [24] have investigated the structural characteristics of a silicon-silicon contact formed between SiNW synthesized by VLS mechanism and an opposing flat Si surface. In [24], SiNW were grown in a CVD reactor with Au as the catalyst, SiH_4 (15 sccm) as the precursor and at growth temperature of 670^{o}C, which resulted in growth rate of 400 nm/min. The wires were grown on the {111} sidewall of a trench etched in the device layer of an SOI wafer and impinged on the adjacent {111} sidewall. Sharma et al. prepared a lamella of the connected wire for TEM analysis by focused ion beam (FIB) milling. Their HRTEM investigation of the lattice

concluded that the VLS SiNW's self-assembled connection is epitaxial and unstrained Si to Si contact.

To obtain deeper understanding of the contact mechanism and determine the factor that can control the contact structure, it is beneficial to observe the process in real time using *in situ* TEM.

5.2 Experimental setup

To study the contact formation mechanism in real time, SiNW contacts were created *in situ* TEM. SiNWs were synthetized *in situ* TEM using the process mentioned in Section 4.2. The self-assembled contact formation mechanism is initiated when a SiNW, grown from a microcantilever heater (referred to as "origin cantilever"), impinges on an opposing flat surface. The flat surface, in this work, was the {111} sidewall of an adjacent cantilever, henceforth referred to as the "receiving cantilever". Figure 5.1, illustrates the basic setup of the experiment.

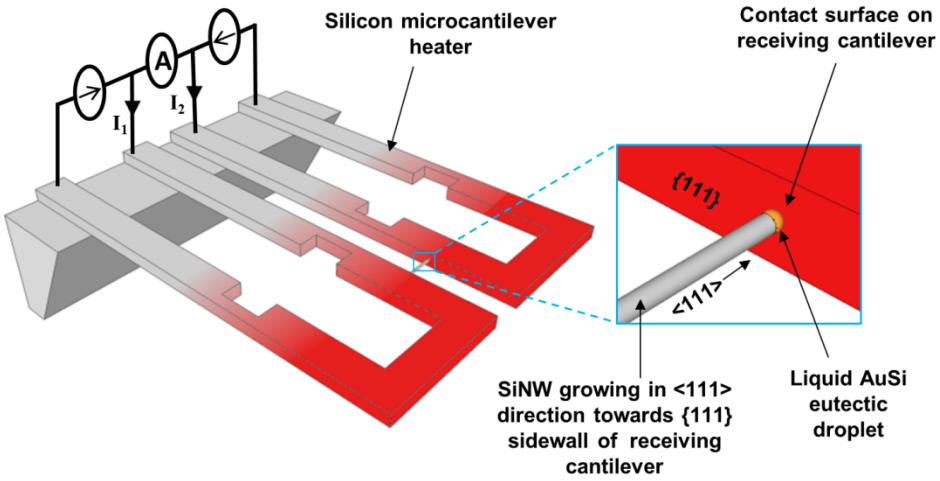

Figure 5.1 Schematic illustration of the contact formation experiment.

As explained in Chapter 3, the SiNW growth temperatures were achieved on the cantilevers by Joule heating. A constant current of 0.65 to 1 mA was passed through each cantilever by separate power supplies typically connected to a common ground (See Figure 5.2). A slight difference in the voltage distribution over the microcantilever existed between the two cantilever loops operating at same current level. This difference was due to slight dissimilarity in the two cantilever loop resistances. The resistance of the two cantilevers was about 42 kΩ with difference between them of about ±1 kΩ. Hence, the two power supplies (Keithley 2400 SourceMeter) had an output voltage difference not exceeding ±0.5 V when operating as constant current sources. This implied that when a wire connected between the two cantilevers operating at same supply current level; a small current in μA range passed

through the wire due to the imbalance in the voltage distribution of the two cantilevers. This leakage current was higher if the two loops were operating at different current levels.

To perform I-V measurements on the bridging nanowire, and also to measure this leakage current, a third ammeter/voltage supply V_R (Keithley 2400 SourceMeter) was connected between the opposing legs of each microcantilever. Figure 5.2 illustrate the equivalent circuit diagram for microcantilever circuits with and without the third Keithley SourceMeter. In the circuit diagram depicted in Figure 5.2(b), one terminal of the third meter/supply is set as the reference voltage V_R for current source I_2 in place of ground. For a Keithley SourceMeter, when V_R is set to 0 V, it acts as an ammeter, which measured the leakage current through the SiNW (R_{SiNW}). The reference voltage V_R could be shifted from 0 V to a desired voltage if controlled current through the SiNW was required while heating the two cantilever heaters. This setup was used for the high temperature electromigration experiments discussed in Chapter 6 and I-V measurements of SiNW at high temperatures, discussed in Chapter 7.

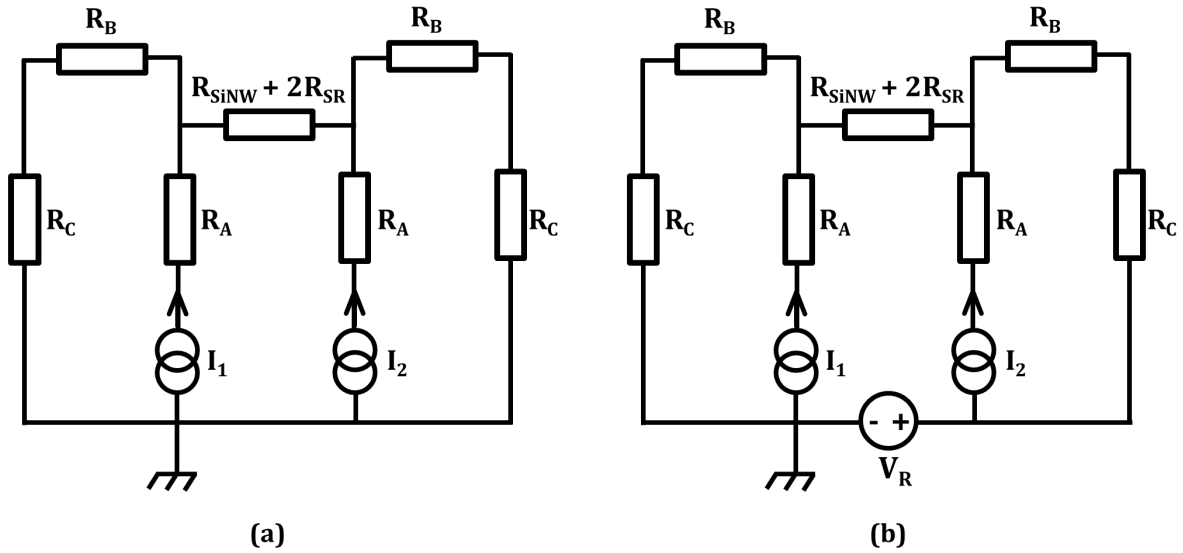

Figure 5.2 Equivalent circuit diagrams for the microcantilever experiments (a) without the third supply/meter and (b) with the voltage supply/ammeter V_R which sets the reference voltage for I_2 instead of ground. R_{SiNW} is the resistance of the SiNW connected between the two cantilevers and R_{SR} is Maxwell spreading resistance contribution from the contact between the wire and the cantilever. The other resistances shown in the equivalent circuit represent different section of the microcantilever heater.

If Figure 4.9 is compared with the schematics in Figure 5.1 (and its circuit diagram in 5.2(a)) it will be seen that the current directions are reversed. As discussed in Chapter 4, electromigration of AuSi eutectic over the cantilever was an important issue and controlled the density of nanowires on the cantilever. To ensure maximum number of wires grew in the gap between the cantilevers, the electron current direction was towards the gap, the case shown in Figure A.3. Ensuring maximum number of wires grew between the gap was beneficial to maximize, in each experiment, the number of contacts that could be created. This is beneficial as wires grew at very slow rates (about 5 to 15 nm/s) and with the post processing required to make the samples ready for growth, usually only one microcantilever chip could be used per day in the TEM.

The TEM imaging was recorded on MiniDV cassettes at a frame rate of 29.97 fps. Quantitative data of contact formation was obtained from digitized files created from these recorded videos. For each contact experiment, the volume and thickness of deposited Si, and the volume, lateral surface area and thickness of the migrating eutectic was determined usually at a rate of one measurement per second. Details of the method used to analyse the videos and estimate the volumes and surface areas are given in Appendix C.

5.3 The contact formation process

The diameters of the SiNWs studied in this work were in the range of 40 to 160 nm. The wires were grown from one silicon microcantilever heater towards an adjacent (receiving) cantilever (See Figure 5.1). Upon reaching the sidewall of the receiving cantilever, the observed Si-Si contact formation that followed is illustrated in Figure 5.3.

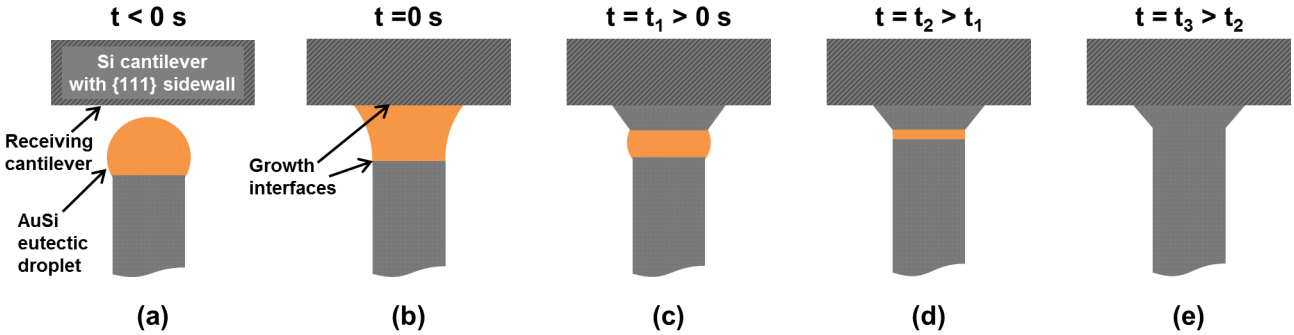

Figure 5.3 Schematic of the contact formation mechanism: **(a)** Free SiNW approaching the receiving cantilever, **(b)** moment of contact when the AuSi catalyst spreads on the receiving cantilever, **(c)-(d)** Au migrates from contact site while Si is being deposited until **(e)** a Si-Si contact is created.

When the impinging wire makes contact with the receiving cantilever, the AuSi eutectic droplet wets the sidewall of the receiving cantilever and its shape is transformed from a semi spherical for free SiNW to a hyperboloid sandwiched between the SiNW and cantilever sidewall (Figure 5.3(b)). This sandwiched AuSi eutectic liquid will catalyse further epitaxial growth until a Si-Si contact is created. There are two liquid-solid interfaces from which epitaxial growth could proceed: one growth front is at AuSi eutectic and SiNW interface and the second growth front is at the interface between eutectic and the cantilever.

While Si is being deposited to create the final Si-Si contact, Au is often migrating or diffusing away from the contact site and hence shrinking the AuSi eutectic volume. The migrating Au may either move to large surface of the receiving cantilever that becomes available to it when the wire makes contact, or it may migrate over the surface of the SiNW. The final location of Au should depend on the dominant migration mechanism and one aim of this work is to try to elucidate which may be the dominant mechanisms in this complex system as discussed in the next section.

The Si deposited in the Si-Si contact has two sources: (i) the Si captured from the gas phase by the VLS mechanism, and (ii) Si that segregates from the AuSi eutectic as the eutectic volume shrinks due to Au diffusion/migration; a case similar to the decaying droplet over the tapering wire discussed in Section 4.6.

The final geometry of the Si-Si contact structure is governed by the Si deposition rate and the rate at which the eutectic volume shrinks with time. By controlling the temperature (and voltage distribution) of the receiving cantilever, the balance between Si growth rate and the eutectic shrinkage due to Au diffusion and electro/thermomigration can be controlled to create contact structures of desired geometries.

When a large enough current is forced to pass through contacting wire, for example, by changing the reference voltage V_R, electromigration became the most dominant effect and this is discussed in more detail in Chapter 6. Electromigration is also the dominant Au migration mechanism if there is a large difference in applied bias voltage (and current) of the two cantilevers; this case is discussed in this chapter.

5.4 Factors controlling contact geometry

In the contact formation process, the rate of migration of Au from the contact site and the rate of Si deposition should define the final geometry of the contact. Au migration and Si deposition rates could be altered by controlling the conditions of the contact surface, which involves adjusting the Joule heating current of the receiving cantilever. Changing the current supplied to the receiving cantilever affects four parameter of the receiving surface:

1. First, changing the current shifts the absolute temperature of the contact surface that changes the rate of Si deposition at the contact site and also affects the Au diffusion and migration mechanisms. Au migration mechanisms of diffusion, electro and thermomigration have an Arrhenius dependence on temperature.
2. Changing the temperature changes the temperature gradient across the cantilever and across the bridging SiNW, which can drive the Au motion by thermomigration, with higher gradient resulting in more prominent thermomigration, as explained in Section 5.4.1.
3. Thirdly, altering the current in the cantilever loop, not only changes its temperature profile but also its voltage distribution as the constant current source has to compensate for the increase or decrease in current by adjusting the applied voltage. When the voltage distribution of the two cantilever loops is not symmetrically equal, it results in a voltage difference across the SiNW that bridges them and current flows through the bridging nanowire. This current will move the Au away from the contact site by electromigration. Even in the case where the two loops are operating at the same current and temperature, a voltage difference as large as 0.5 V could exist between the two cantilever power supplies due to difference in the electrical resistance of the two cantilevers.
4. Changing the current, and hence the current density, passing through the receiving cantilever should change the rate of Au electromigration over the cantilever surface as

well. Increasing the current on the receiving cantilever, for example, should increase Au migration from the contact site if the current density of the cantilever is higher than for nanowires. Otherwise nanowire current would drive electromigration.

These four parameters of the receiving surface, dependent on the supplied current, define the rate of AuSi eutectic shrinkage and Si deposition, and hence the final geometry of the contact. In the following subsections, Si deposition and different Au migration mechanism are discussed.

5.4.1 **Au migration mechanisms**

Results from *in situ* UHV-TEM SiNW growth have shown that diffusion of Au due to Ostwald ripening (OR) defines the length and shape of free SiNWs [63]. As discussed in Section 4.3, in OR mechanism large AuSi eutectic droplets grow at the expense of smaller droplets through the diffusion of Au atoms from the smaller to the larger droplets. This diffusion of Au atoms is driven by the Gibbs-Thomson effect. If AuSi eutectic liquid at the contact site has significant geometrical curvature, then Au migration by OR must be considered in any analysis of the contact formation process. However, OR process occurs over a longer time scale (few hours in case of UHV-TEM example in Figure 4.5(a)) compared to typical contact formation event and it is not expected to be a dominant migration mechanism.

The limited field of view in TEM makes it difficult to ascertain the presence of other AuSi eutectic droplets near the bridging SiNW that are serving as the source or sink for Au atoms. However, the internal pressure of the AuSi eutectic droplet at the contact site, derived from Equation 4.1, can be used to check if OR is the dominant migration mechanism; that is, the radius of curvature of the AuSi eutectic at the contact is a good indicator if OR is plausible if AuSi eutectic droplets with large or negative radii of curvature mainly grow while AuSi eutectic droplets with smaller radii of curvatures mainly shrink.

In addition to OR, thermo and electromigration mechanism can drive Au diffusion. In thermomigration, Au migration is driven by the temperature gradient. Ichinokawa et al. [69] investigated the thermomigration of AuSi eutectic islands on Si substrate and demonstrated that the islands moved from low to high temperatures and the thermomigration velocity is proportional to the temperature gradient. Electromigration, as shown in Section 4.7, is the mechanism in which the direct current flowing through the solid can cause Au atoms to migrate. Ichinokawa et al. [69] also investigated the electromigration of liquid AuSi islands at high temperatures. Their results agreed with the observation made in Section 4.7 that the Au moves in the direction of electron current, that is, in direction opposite to conventional electrical current. In [69], it is demonstrated that the velocity of AuSi island electromigration is directly proportional to the current density.

Following the treatment in [69], the diffusion velocity v of the migrating Au atoms due to a concentration gradient, temperature gradient and electrical current can be expressed using the Fick's diffusion equation, as follows:

$$v = -D\frac{\partial lnC}{\partial x} - \frac{D}{T}\frac{Q^*}{k_B T}\frac{\partial T}{\partial x} + BeZ^*\rho j \tag{5.1}$$

where C is the concentration of Au atoms, Q^* is apparent heat of transport for the migrating Au atoms, k_B is Boltzmann's constant, B is mobility, Z^* is the effective charge number of migrating ions, e is elementary charge, ρ is resistivity of AuSi eutectic droplets, j is the current density and D is diffusivity. The diffusivity D obeys Arrhenius behaviour with respect to temperature T:

$$D = D_0 exp\left(\frac{-E_{diff}}{k_B T}\right) \tag{5.2}$$

where E_{diff} is the activation energy for diffusion and D_0 is the pre-exponential factor.

The second term in Equation 5.1 represents the diffusion velocity due to thermomigration, and using Equation 5.2, it can be expressed as:

$$v = -\frac{D_0 Q^*}{k_B T^2}\frac{\partial T}{\partial x} exp\left(\frac{-E_{diff}}{k_B T}\right) \tag{5.3}$$

From Eq. 5.3, it is evident that the diffusion velocity increases with higher temperature gradient at fixed temperature. Ichinokawa et al. [69], observes that Q* is negative for all metals, as they move from cold to hot regions and measured an activation energy of 0.6 eV for thermomigration.

The third term in Equation 5.1 represents the migration velocity due to electromigration and can be rewritten following the Nernst - Einstein relation relating mobility B to diffusivity D:

$$v = BeZ^*\rho j = \frac{D_0}{k_B T}\ exp\left(\frac{-E_{diff}}{k_B T}\right) eZ^*\rho j \tag{5.4}$$

Ichinokawa et al. [69] determined an activation energy of 0.7 eV for electromigration driven diffusion. Their activation energies obtained for the two migration mechanism, electromigration and thermomigration, agree within experimental error with each other. Ichinokawa et al. made their observations on microscopic gold islands on Si, which likely have different diffusion coefficients compared to individual atoms. For diffusion of individual Au atoms, the values of D_o =0.12 m^2/s and E_{diff} = 1.99 eV as given in [71] will be considered.

In the electromigration process, the net force acting on the diffusion atom (ion) has two contributions: a direct force and wind force [72]. The direct force is due to the applied electric field E ($E=\rho j$) that exerts a direct electrostatic force on the moving ion. The electron wind force arises from the momentum exchange due to the scattering of conduction electrons by the migrating atoms. In simplified terms, the electrons moving with a certain drift velocity due

to the applied electric field E will scatter from the diffusing atoms, and "push" them in the direction of electron flow. The net driving force F_{em} on the diffusing atom is given as:

$$F_{em} = eZ^*E = e(Z_{el} + Z_{wd})E \tag{5.5}$$

The effective charge number, Z^*, is dimensionless and its value range from 10^{-1} to 10^2 [72]. Z^* can be thought of as the effective charge the moving specie has to possess in order that it be subject to an electrostatic force equal to the driving force for electromigration. In Equation 5.5, Z^* is divided into the contribution for each driving force. Z_{el} represents the direct electrostatic force and its value can be expected to be the nominal valence of the diffusing ion when the dynamic screening effect is ignored. The second term, Z_{wd}, is an assumed charge number that corresponds to the wind force and is larger than Z_{el} for good conductors. In metal conductors, due to the screening by conduction electrons, the direct force on the ion is quite small and wind force is more dominant. Hence, for metal conductors, ions move in the direction of electron current. In case of semiconductors, as the resistivity is higher, the effect of direct force is greater than in metals. The direction of metal impurity atoms may not be in the direction of electron wind. As Ichinokawa et al. [69], [73], demonstrated that though AuSi islands move in the direction opposite to the conventional current, i.e., in the direction of electron flow, the AlSi islands behaved oppositely by moving in the direction of current. The opposite directions of electromigration for Au and Al on Si are assumed to be due to difference in electronegativity of the metal atoms with respect to Si: Au has larger electronegativity than Si, while Al is smaller than Si [73]. The electromigration of Au atoms on Si in the direction of electron current has also been observed in [74].

Instead of individual atoms, AuSi eutectic droplets can also relocate due to the Marangoni effect, which relates to the motion of liquid by surface tension gradients that can be generated by changes in any variable that affects surface tension, such as composition and temperature. Due to a temperature gradient, it is assumed that the surface tension of AuSi eutectic (dependent on temperature) varies over the length of the cantilever and can cause the eutectic to move. From Equation 4.1, it can be concluded that for a droplet with certain radius, higher surface tension yields to higher internal pressure. Hence, AuSi eutectic from droplets in the cold regions with higher surface tension (and internal pressure) can be "squeezed out" and move to the hot regions with lower surface tension and internal pressure.

In [75], Lu and Jiang have given the surface tension of Au, $\gamma_{Au,}$ to be 1.211 J/m^2, which is very close to the value of 1.22 J/m^2 for AuSi eutectic . For Au droplets, the temperature coefficient of surface tension $d\gamma_{Au}/dT$ was found to be -0.00018 J/m^2/K [75]. If it is assumed that AuSi eutectic surface tension has similar temperature coefficient, the difference in internal pressure ΔP_{12} of two droplets with equal radius R but at different temperature T_1 and T_2 can be expressed as:

$$\Delta P_{12} = \big(\gamma_{lv}(T_2) - \gamma_{lv}(T_1)\big)\frac{2}{R} \tag{5.6}$$

Assuming the surface tension coefficient of Au and AuSi eutectic are similar,

$$\Delta P_{12} = \frac{2}{R}\Delta T \frac{d\gamma_{Au}}{dT} \tag{5.7}$$

Estimating the pressure difference by Equation 5.7, it can be seen that the internal pressure changes are not significant: As a worst case, for a droplet of radius 20 nm, and temperature difference of 100 ^{o}C, the pressure difference is only 0.71 MPa. This implies that the effect is much smaller than OR, where easily occurring curvature differences between droplets gives rise to much higher internal pressure difference between the droplets than the Marangoni effect estimated here.

Upon initial contact of the AuSi eutectic with the receiving cantilever, part of the Au from the eutectic can move to the surface of the microcantilever to form the equilibrium surface coverage. That is, if it is considered there was not sufficient Au near the contact site then Au on the wire tip would diffuse away because it wants to form the $\sqrt{3} \times \sqrt{3}$ surface reconstruction of 1/3 monolayer of Au [63]. If the coverage on the destination is lower than equilibrium, the Au will "fill up" the surface. In the experiments, Au was deposited on both sides (top and bottom) of the cantilever to minimize surface coverage losses to the catalyst droplet. And if there was more than 1/3 monolayer, the surface is already "full" and the excess forms droplets. Hence, existence of AuSi droplets on the (111) sidewall will negate this diffusion mechanism. Formation of droplets on wire by electromigration was visualized; indicating surface coverage on the wires and cantilever surfaces.

In analysing the contact formation experiments, volumetric rate of Au migration are measured first. But from them, Au diffusion velocity v can be obtained as volumetric migration rate of Au (dV_{Au}/dt) is related to Au diffusion velocity v as:

$$\frac{dV_{Au}}{dt} = C_{int} a v = 2\pi r_{int} a v \tag{5.8}$$

where a is the unit length of Au unit cell (a=2.6 pm) and C_{int} is the circumference and r_{int} is the radius of the Si/AuSi eutectic interface. As can be seen in Figure 5.3(b), there are two Si/AuSi interfaces. C_{int} represents, at any given time, the circumference of the growth interface from which Au is migrating. In Section 5.5, it will be shown that at any given time, growth only proceeds from one growth front and Au also migrates in one direction and, hence, only from one of the interface.

5.4.2 **Si deposition during contact formation**

In the contact formation process, there are two primary sources of Si deposition. Si incorporated in the Si-Si contact comes from the disilane gas phase via the VLS mechanism and from the Si that segregates from the AuSi eutectic as eutectic volume shrinks due to diffusion of Au. Both the Si deposition mechanisms have a dependence on temperature. For Si captured from the disilane gas, an Arrhenius relationship similar to one presented in Equation 3.9 can be written:

$$\frac{dV_{gas}}{dt} = Ge^{-\frac{E_{gas}}{k_B T}} \tag{5.9}$$

where G is the prefactor and E_{gas} is the activation energy for incorporation of Si from disilane gas to the contact. As was the case for free SiNW growth, E_{gas} encompasses all the steps of Si incorporation from gas phase to the contact site, i.e., mass transport in the gas phase, chemical dissociation of disilane at gas-liquid interface, diffusion of Si atoms through the liquid eutectic and incorporation of Si from eutectic into the solid, in a single activation energy. dV_{gas}/dt is the volumetric deposition rate of Si captured from the gas phase. In contrast to the free SiNW where growth rate (dl/dt) is used, for contact formation process, the volumetric rates are used since the diameter of the contact may not remain constant during the contact formation process. Following the derivation in Section 4.4.3, the prefactor G can be derived. Silicon deposition rate from gas phase is given as:

$$\frac{dV_{gas}}{dt} = 2A_s \frac{P}{N_{Si}\sqrt{2\pi m k_B T_{RT}}} I_0 e^{-\frac{E_{gas}}{k_b T}} \tag{5.10}$$

Where A_s is the surface area of the AuSi eutectic liquid sandwiched between the two Si/AuSi interfaces. Comparing Equation 5.9 and 5.10, we can write:

$$G = 2A_s \frac{P}{N_{Si}\sqrt{2\pi m k_B T_{RT}}} I_0 \tag{5.11}$$

Si that segregates from the shrinking AuSi eutectic and is incorporated in the contact site relies on the eutectic shrinkage rate and the contribution from this Si deposition mode can be given as:

$$\frac{dV_{seg}}{dt} = U\frac{dV_{eu}}{dt} \tag{5.12}$$

Where dV_{seg}/dt is the deposition rate for Si that comes from segregation of Si from the eutectic, and dV_{eu}/dt is the rate of change of eutectic volume (and must not be confused with dV_{Au}/dt, the migration rate of Au). U will define the segregation coefficient, given by an Arrhenius equation as well:

$$U = \beta M e^{-\frac{E_{seg}}{k_B T}} \tag{5.13}$$

β is the atomic percentage of Si in the AuSi eutectic and is defined by the AuSi phase diagram. E_{seg} is the activation energy required for segregation of Si atom from the eutectic, its diffusion through the AuSi eutectic and epitaxial incorporation to the Si contact growth front. M is the proportionality constant that covers the dissolution rate of Si in the eutectic and the fact that the eutectic is supersaturated and β may not represent the actual percentage of Si in the eutectic at equilibrium as defined in Figure 4.2.

The total deposition rate of Si (dV_{Si}/dt) at the contact site is given as:

$$\frac{dV_{Si}}{dt} = \frac{dV_{gas}}{dt} + \frac{dV_{seg}}{dt} \tag{5.16}$$

$$\frac{dV_{Si}}{dt} = 2A_s \frac{P}{N_{Si}\sqrt{2\pi m k_b T_{RT}}} I_0 e^{-\frac{E_{gas}}{k_B T}} + \beta M e^{-\frac{E_{seg}}{k_B T}} \frac{dV_{eu}}{dt} \tag{5.17}$$

From experimental results, it is not easy to accurately determine the contribution of each Si source to the Si deposition rate. Hence, for experiments, the total Si deposition is represented by a single Arrhenius equation, where the activation energy covers Si deposition from both VLS mechanism and segregation. Moreover the experiments were carried out in a limited temperature range between 470 to 550°C and hence activation energy from Arrhenius graphs will not be reliable.

5.4.3 Methodology for the contact geometry study

To study the contact formation process, the dimensions of the deposited Si and shrinking eutectic are measured at different stages of the contact formation process. These parameters include: the width of the contact at its interface with the receiving cantilever (w_c), the height of Si deposited on the cantilever (h_c) and nanowire (h_{nw}), height of the eutectic (h_e), the diameter of the interface between Si and liquid eutectic (d_{int}) and the radii of curvature of the liquid eutectic (R_x and R_y). These dimensions are shown in Figure 5.4. There are two Si /liquid eutectic interfaces; d_{int} will represent the interface from which the Au is escaping by one of the above mentioned Au migration mechanism. For the hyperbolic geometry of the liquid eutectic in Figure 5.4(c), R_y is negative while R_x is positive, i.e., positive curvature when convex and negative when concave.

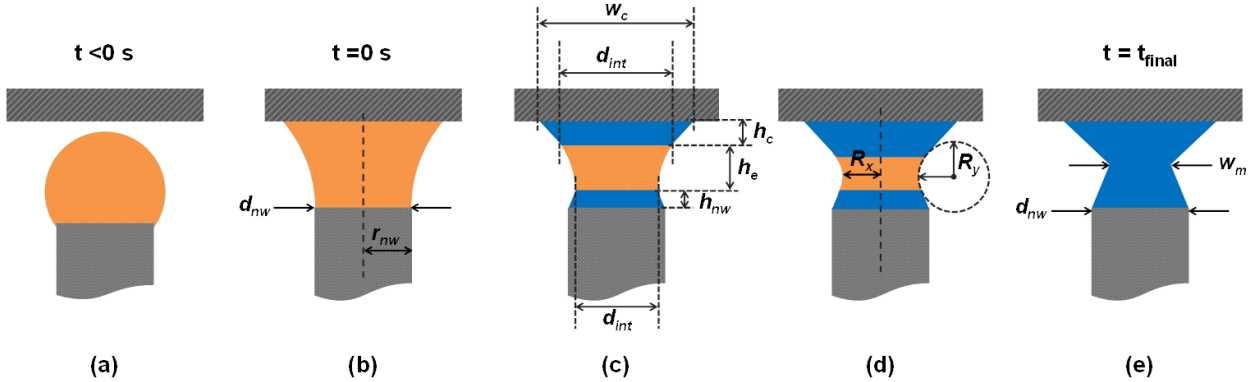

Figure 5.4 Schematic diagram showing the formation of a necked contact: **(a)** t=0 s when the eutectic riding on the tip of SiNW impinges on the receiving cantilever, the wire diameter, $d_{nw}=2r_{nw}$ is shown, **(b)** and **(c)** intermediate states of the contact formation process indicating the dimensional parameters, w_c, di_{nt}, h_c, h_e h_{nw}, and radii of curvature R_x and R_y, and **(d)** $t=t_{final}$, when the necked Si-Si contact formation is completed, the parameter w_m is shown.

The objective for measuring the dimensions indicated in Figure 5.4 was to calculate the volumes of deposited Si and the volume and surface area of the eutectic. Usually, these quantities were measured for each contact formation process at rate of one measurement per 0.25, 1, 10, or more seconds, depending on the contact geometry and ease of measurement. See Appendix C for details on the method used to estimate the volumes and surface areas from TEM images.

The shape of the contact geometry can be defined by a number, contact geometry ratio ξ, which is the ratio between the width of the middle of the contact (w_m) and the diameter of the free nanowire d_{nw} ($d_{nw}=2r_{nw}$, r_{nw} being the radius) at SiNW/eutectic interface at the moment of initial contact (t=0 s):

$$\xi = \frac{w_m}{2r_{nw}} \tag{5.18}$$

The parameters d_{nw} and w_m are shown in Figure 5.4 for a necked contact, in which case the contact geometry ratio is less than 1. For straight contacts, contact geometry ratio is almost 1, while for bulged contacts it is greater than 1. And for nano gaps, it is zero.

In the following section, for each contact geometry type, an image series showing the evolution of the contact geometry with time will be presented. Furthermore, plots of volume of the liquid AuSi eutectic and volume of deposited Si versus time are plotted. For discussion in the coming section, following factors are important to cover:

1. Possible driving forces for the thermomigration and electromigration, i.e., the temperature gradient along the wire and at the contact site and the current passing through the wire and the cantilever (Equation 5.3 and 5.4)
2. The possible presence of curvature driven migration of liquid eutectic, i.e., OR process can be tested by studying the shape of the AuSi eutectic
3. Formation of any droplets near the vicinity of the contact site to prove that the contact surface has sufficient equilibrium coverage of Au and no contribution to Au equilibrium surface coverage comes from the AuSi eutectic involved in making the Si-Si contact
4. Relationship between the volumetric rate of change of eutectic and the circumference of the growth interface (Equation 5.8)
5. Relation between the surface area of the eutectic and the deposition rate of Si. (Equation 5.10).
6. Relation between migration rate of eutectic and the deposition rate of Si to find the contribution of Si segregating from the eutectic (Equation 5.12)

Analysing these factors will help understand how the SiNW contacts vary in geometry and that their final structure depends on the difference between rate of AuSi eutectic shrinkage due to Au migration and deposition rate of Si.

5.5 Results from the contact geometry study

The formation of each contact type is discussed below, starting with straight contacts.

5.5.1 Straight contacts

Figure 5.5 shows the TEM image sequence of the formation of a straight contact with ξ close to 1 ($d_{nw} \approx w_m \approx 100$ nm).

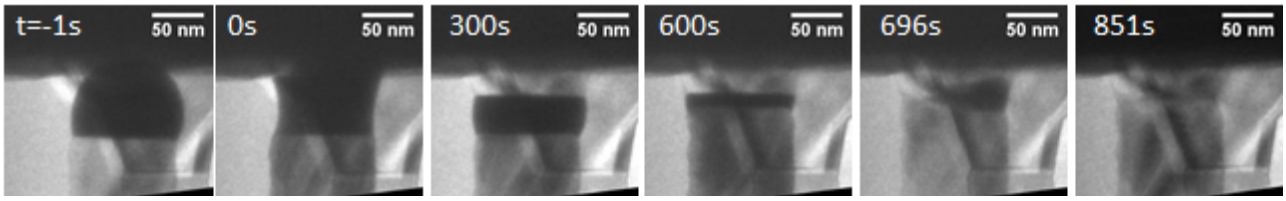

Figure 5.5 Sequence of TEM images showing the creation of a straight Si-Si contact

The contact formation process follows the description given in Section 5.3: The hemispherical AuSi eutectic droplet riding on the tip of 100 nm wide SiNW (at t=-1 s) was transformed into hyperboloid shaped geometry on contact with the receiving sidewall at t=0 s. Si deposition continued, catalysed by the AuSi eutectic liquid sandwiched between two Si surfaces. The contact was wider at its interface with the cantilever compared to the wire diameter (i.e. $w_c > d_{nw}$) because liquid eutectic at cantilever interface undergoes a transition in its shape as the contact formation process proceeded. This is similar to the early stages of nanowire growth, where the base of the SiNW is wider than the diameter of the wire [76]. Intermediate stages of contact formation are shown at t=300 and 600 s. It can be seen that the liquid eutectic shape transformed with time from its initial hyperboloid geometry (at t=0s) to a bulged convex shape. This transformation from a negative radius of curvature (R_y) to a positive curvature was not accompanied by change in direction of eutectic migration, indicating that the curvature driven migration process of OR was not dominant. The Si-Si contact was completed at t=696 s, while some AuSi eutectic stayed at the contact after its completion for more than 2 minutes. The presence of AuSi droplet after Si-Si contact formation indicated that there was sufficient surface coverage of Au atoms on the Si-Si contact to promote eutectic droplet formation for excessive Au.

This straight contact was achieved by setting both cantilevers at 0.8 mA heating current (32 mW in power), which resulted in wire and contact site temperature of ca. 485^{o}C. At this temperature, a thermal gradient of 0.4 K/µm existed over the cantilever, which could drive thermomigration of Au. Since the two ends of the wires were set to be at same temperature, it is assumed there was a small thermal gradient over the wires. However, since temperature readings are not accurate, a 10^{o}C offset can create a gradient of 4 K/µm over the 2.5 µm long wire. Disilane pressure was maintained around 13 µTorr. During the contact formation process, a current of 0.24 µA flowed through the wire in the direction of the origin cantilever due to a slight difference in the voltage supplied to the two cantilevers. This current through the wire was measured by V_R connected between the opposing legs of the cantilever. Current of 0.24 µA through the wire translates into a current density of 31 µA/µm^2 through the SiNW,

which was comparable to the current density of 23 μA/μm^2 through the cantilever due to the Joule heating current.

From the recorded videos, the volume of AuSi eutectic liquid and deposited Si was measured at a rate of one data point per second when geometries of deposited Si and AuSi eutectic were well defined. These results are plotted in Figure 5.6 and 5.7.

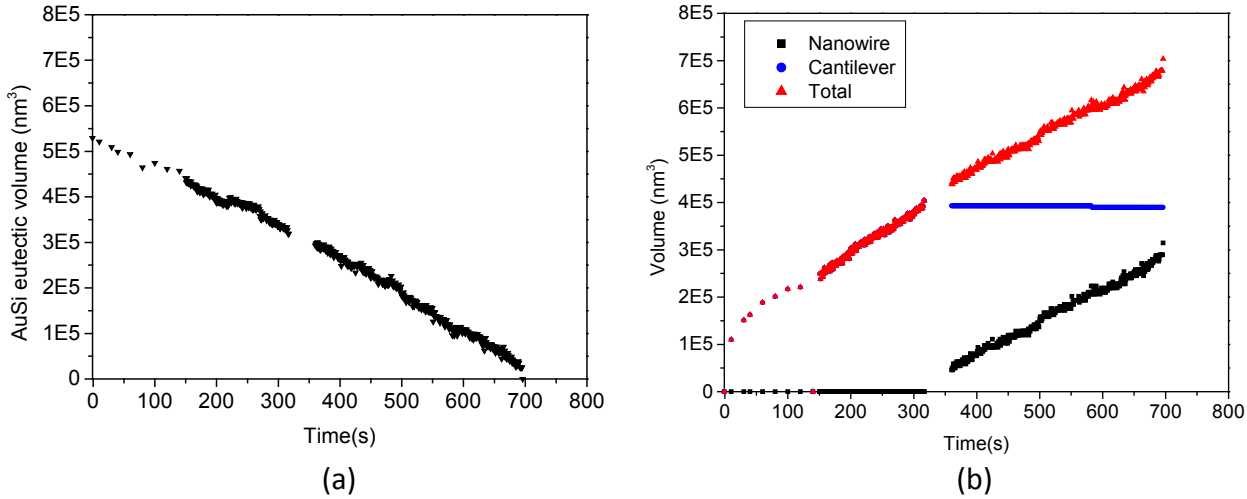

Figure 5.6 Volume plots vs. time for straight contact formation process **(a)** volume of AuSi eutectic and **(b)** volume of deposited Si. Si was deposited at only one liquid/solid interface at a time, the Si deposited at the cantilever side and at the nanowire side are also plotted to illustrate this observation.

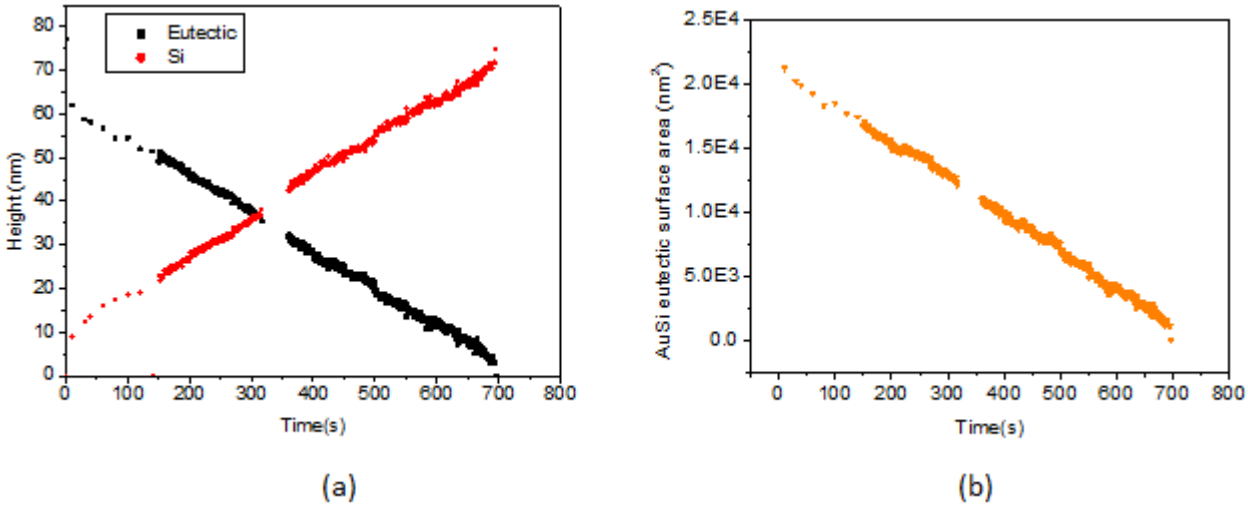

Figure 5.7 Plots of **(a)** AuSi eutectic and total deposited Si thickness and **(b)** eutectic surface area.

In Figure 5.6, it can be seen that the AuSi eutectic volume was decreasing linearly at a rate of 750 nm^3/s. At 485^{o}C, the eutectic composition has about 23 atomic % of Si, and the remaining 77% is Au, leading to Au migration rate of 0.77x750=577 nm^3/s. From Equation 5.8, with $r_{int} \approx r_{nw}$=50 nm, an Au migration velocity of ca. 700 nm/s was obtained, which is much larger than the theoretical values. With Equation 5.3 and 5.4, the theoretical thermo and

electromigration velocities can be calculated. Taking Q^* as -0.347 eV, E_{diff} as 1.9 eV, D_o as 0.12 m^2/s, Z^* as 1 and ρ as 6.3×10^{-8} Ohm.m (for Au), a theoretical thermomigration velocity of 0.02 nm/s and electromigration velocity of 2.1×10^{-4} nm/s is obtained, which is several order of magnitude lower than the experimental result. This discrepancy in migration velocities was true for all the contact geometries analysed in this work and could be most likely due to the diffusivity pre-exponential factor and activation energy not being the same as the values used in theoretical calculations. Moreover, the system being studied here is complex with different Au migration mechanism driven by different forces and the theory in Section 5.4, though it gives a sufficient knowledge of the concepts, is not realistic enough in getting the migration rates correct.

The Si deposition was, interestingly, taking place from only one interface at a time, but at almost equal rate. The amount of Si being deposited at the nanowire and the cantilever side are plotted in Figure 5.6 (b). As mentioned above, the eutectic composition was 23 atomic % Si, and as the AuSi eutectic volume was decreasing linearly with 750 nm^3/s, this leads to a likely Si volumetric deposition rate from segregation (dV_{seg}/dt) of 0.23x750=172 nm^3/s, if we assume that all segregated Si was deposited at the contact, i.e., $U=\beta$ (Equation 5.13). The observed Si deposition (Figure 5.6(b)) was linear in time with an almost constant rate of 780 nm^3/s, where 608 nm^3/s then must have been supplied by the precursor gas, disilane.

Following the discussion in Section 4.6 on tapering wires, the expected contribution to deposited Si from disilane via the VLS mechanism was calculated by knowing the volumetric rate of Si deposition per AuSi eutectic surface area (ϑ). The value of ϑ was evaluated to be ~0.047 nm/s. The expected Si deposition is compared with observed Si deposition in Figure 5.8.

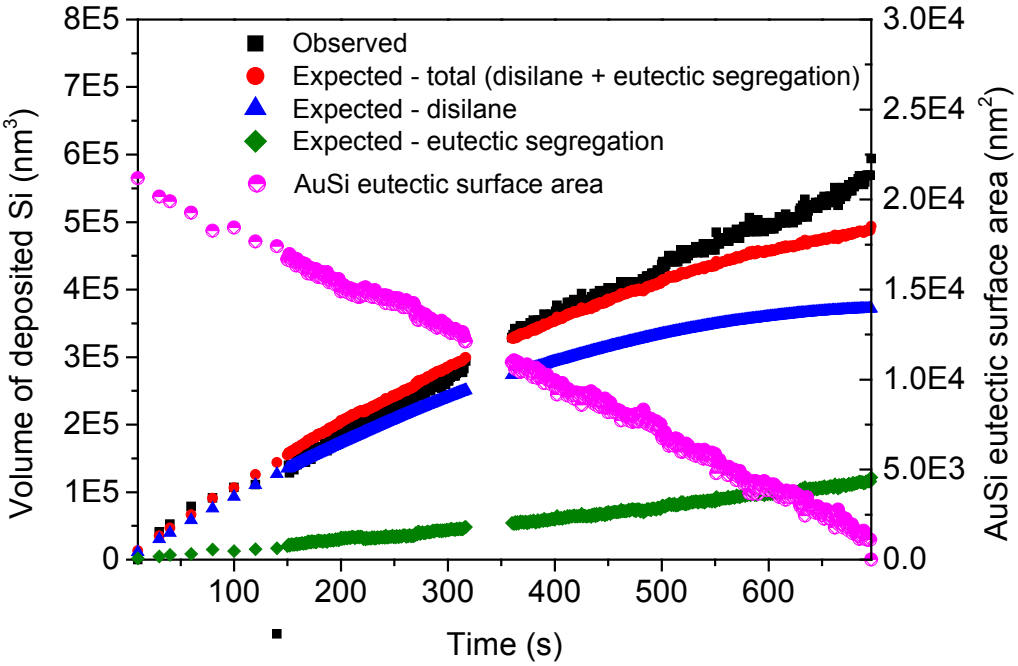

Figure 5.8 Comparison of observed and expected Si deposition volumes as function of time.

As the surface area of the shrinking eutectic is decreasing linearly over time, Si deposition from gas phase (dV_{gas}/dt), which has a proportional dependence on eutectic surface area (Equation 5.10), should hence be decreasing linearly over time as well. Hence, a decreasing Si deposition rate is expected for a shrinking eutectic surface area as can be seen in the expected Si deposition curve. However, the observed Si deposition rate is nearly constant for the entire contact formation event and diverges from the expected Si deposition volumes from around 500 s onwards. This implies that, in addition to Si supply from gas phase and by segregation from the eutectic, a third source could exist that supplies Si to the contact. This can also imply that in this system, eutectic is far from the equilibrium composition and there is much more Si than defined by the phase diagram in Figure 4.2.

5.5.2 **Bulged Si-Si contacts**

Bulged Si-Si contacts were created when, during the contact formation process, the contacts grew wider over time in the contact region compared to the SiNW diameter. As an example, the sequence of events that created a bulged contact for a SiNW with 165 nm diameter is shown in Figure 5.9. The geometry of eutectic become complex as the contact formation process proceeded. Hence volumes were calculated only when the geometry was well defined. The radius of curvature R_y changed from -95 nm for t=0 s to +100 nm for t=430 s, while the eutectic only shrinks, indicating OR was not responsible for the Au migration. If the images at 942 s and 943 s are compared, it can be seen that the eutectic shape went through dramatic restructuring; with part of Si from the wire dissolved into the eutectic. The restructuring of eutectic was common for all bulged contacts studied in this work.

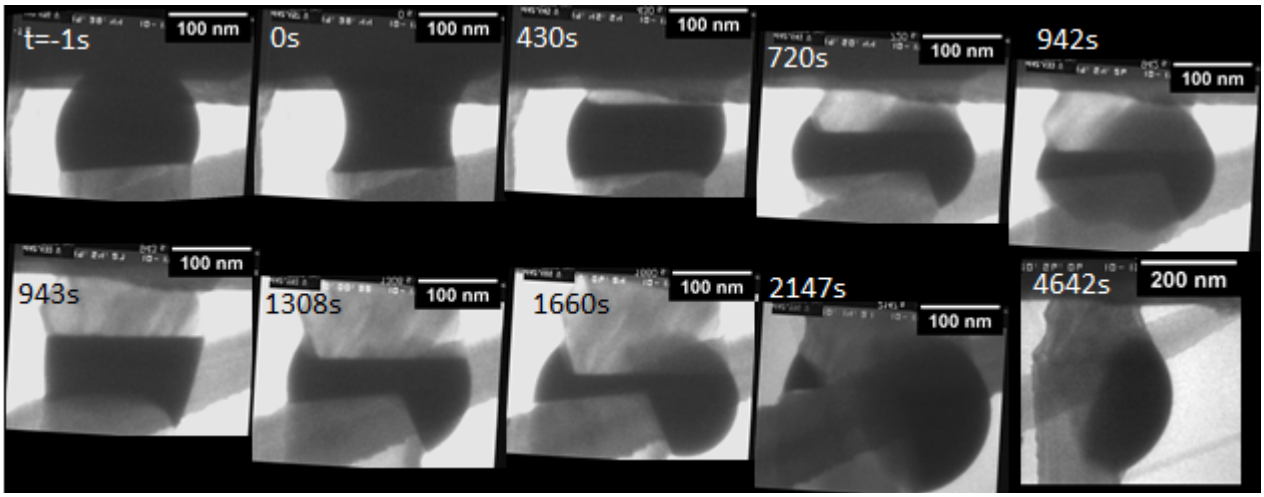

Figure 5.9 TEM image sequence showing the formation of a bulged Si-Si contact with ξ= 1.6

To create the bulged contact in Figure 5.9, the origin cantilever was set at a higher temperature than the receiving cantilever and electron current through the SiNW, responsible for Au electromigration, flowed towards the origin cantilever. To achieve these conditions, the receiving cantilever was supplied a lower Joule heating current than the origin cantilever. A current of 0.7 mA (28.3 mW) was set for the receiving cantilever, resulting in contact site temperature of ca. 480°C, while the base of SiNW on origin cantilever was at ca. 490°C with

0.79 mA (33.7 mW) heating current. Tough there is a difference of 5.4 mW between the supplied power to the two cantilevers; the temperature difference is only 10°C between the cantilevers. This was due to lowered contribution from the receiving cantilever to chip heating, as discussed in Section 3.5.3. The cantilever temperature gradient was ca. 0.3 K/µm while the gradient over the wire was ca. 4 K/µm, indicating that the strongest thermomigration contribution would move Au along the nanowire towards the origin cantilever.

Since the current supplied to the two cantilevers was different, the voltage difference across the SiNW was 1V which resulted in SiNW current of 22 µA in the direction of the receiving cantilever. The current density in the wire, at ~1000 µA/m^2 , was several times larger than 20 µA/µm^2 current density in the receiving cantilever. Hence, electromigration of Au was expected to be over the wire in the direction of origin cantilever.

The conditions described above resulted in AuSi eutectic shrinkage of 650 nm^3/s, while the Si deposition rate was of the order of 3200 nm^3/s, with disilane pressure in the range of 11 to 17 µTorr. Si growth proceeded only from the cantilever end, which was also observed for other bulged Si-Si contacts. The contribution to Si deposition rate by Si segregation from the eutectic was only 145 nm^3/s indicating that most Si came from the gas phase during the contact formation process which took 2147 s to complete. The Si deposition rate decreased to 2000 nm^3/s close to the completion of the contact from about t=1500 s onward. This can be linked to decrease in surface area of the eutectic, but the geometry of the eutectic was quite complex after t=575 s and the surface area could not be calculated accurately to determine its relationship with Si deposition rate. At the completion of the Si-Si contact, defined as when the two Si faces meet, most of the AuSi eutectic stayed at the contact site, and catalysed further deposition of Si over the contact. A droplet at the base of the wire at the origin cantilever was also present (see Appendix D, Figure D.2). This indicated that Au was leaving the contact site and moving to the nanowire base in the direction of electron current but Au was also entering the eutectic at contact site from the receiving cantilever.

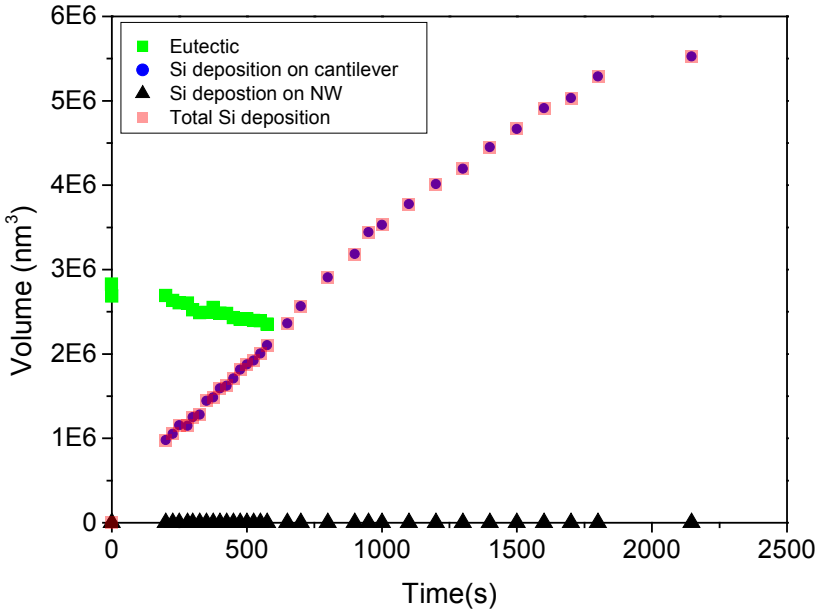

Figure 5.10 Volume plots for bulged contact formation process.

It was recorded that even at higher temperatures of 505°C at the contact site and 525°C for the nanowire base and nanowire current density in the range of 750 μA/μm^2; a bulged contact can be created, shown in Figure D.1 in Appendix D. The Au migration for this case appears to be towards the contact site, as in the early stages the eutectic volume increases at a rate of +152 nm^3/s, while Si deposition rate was about 1500 nm^3/s. A large thermal gradient that exists over the wire and the electron current through the wire would drive Au in the direction of the origin cantilever but the eutectic stays at the contact site.

5.5.3 **Necked Si-Si contacts**

Necked contacts are defined as such since they are narrower than the wire diameter, i.e., it has a narrow neck in the middle where two growth fronts meet at the completion of contact formation. Figure 5.11 shows the necked contact case, where the impinging wire was 70 nm in diameter with a growth rate of 13 nm/min for disilane pressure of 14 μTorr. Both the wire and the receiving surface were at a temperature of ca. 520°C. These temperatures were maintained by supplying a current of 0.73 mA (ca.32 mW) to each cantilever heater.

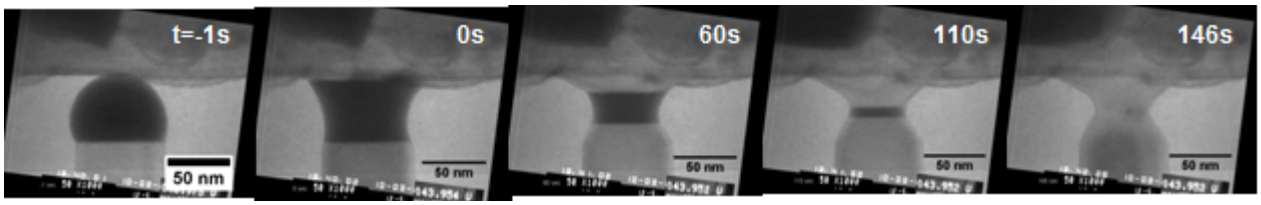

Figure 5.11 TEM image sequence for necked contact formation process.

From Figure 5.11, it can be seen that for necked contact formation, R_y remained negative throughout the contact formation process and its value changed from -57 nm (and -37nm for right hand side) at t=0 s to -28 nm after 60 s. This implied that the internal pressure of the eutectic was small around ca. 10 MPa at t=0 s and 2.6 MPa at 60 s compared to, for example, the internal pressure of 60 MPa for a eutectic droplet with radius of curvature of 40 nm (that is the case of the droplet at t=-1 s). The small internal pressure for the eutectic liquid in necked contact formation events, should transport more eutectic to the contact site if OR mechanism was present but the opposite is observed; indication that OR was not dominant.

For this case thermomigration was driven by a 0.7 K/μm gradient along the cantilever, while on contact a current of ca. 1.7 μA passed through the wire resulting in a current density of ca. 400 μA/μm^2. In addition to thermo and electromigration, Au diffusion due to concentration gradients, in particular, Au migration driven by preference for equilibrium surface coverage of Au on Si cannot be ignored. However, the presence of AuSi eutectic droplet in the vicinity of the contact site in Figure 5.11 indicates there was sufficient Au on the surface to promote droplet formation.

For the necked contact case, Au migration rate was higher hence the segregation rate was higher as well, which resulted in a Si growth rate of 22 nm/min during contact formation; much higher than the 13 nm/min recorded for the free SiNW before contact. The volumetric

rate for Au migration at 2400 nm^3/s was much higher than the 1400 nm^3/s rate of Si deposition; this resulted in the formation of a necked contact as the growth interfaces become narrower with time. The diameter of the necked section (w_m) is 40 nm compared to 70 nm for the nanowire. The volumes of eutectic and observed deposited Si are plotted in Figure 5.12(a) and the observed and expected Si deposition is compared in Figure 5.12(b). To determine the expected Si deposition from VLS mechanism, the volume of deposited Si per surface area of the eutectic per time (ϑ), as defined in Equation 4.11, was evaluated to be 0.067 nm/s. From Figure 5.12 (b) it can be seen that the observed and the expected deposited Si only agree in the early part of the Si deposition process and indicate that there is an unaccounted source of Si during the contact formation process.

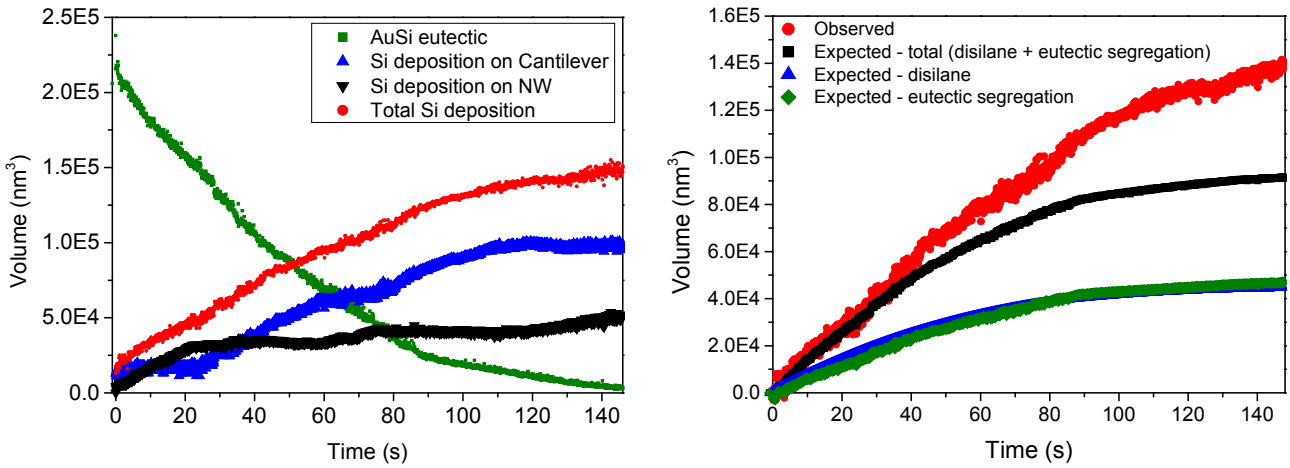

Figure 5.12 (a) Eutectic and deposited Si volumes as function of time and **(b)** comparison of observed and expected Si deposition volumes for necked contact formation process.

If the migration rates of Au are increased further compared to Si deposition, extreme necking occurs as shown in Figure 5.13, where the SiNW is 145 nm while the necked region is only 20 nm wide.

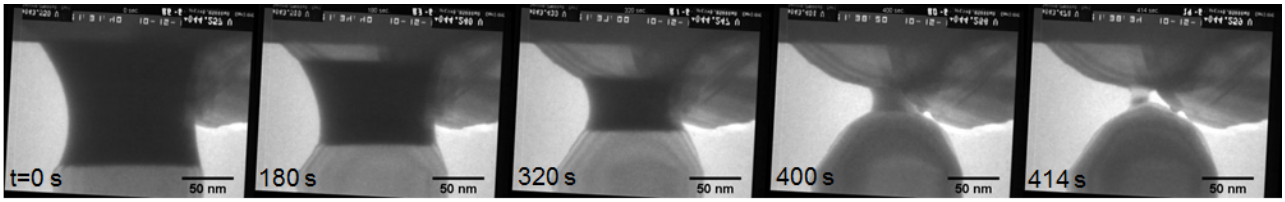

Figure 5.13 TEM images series showing the formation of an extremely necked contact

This structure was achieved by setting the receiving contact surface to 530°C with a gradient of 0.75 K/µm. Also, a voltage difference of 0.4 V existed across the SiNW since the origin cantilever was operating at 0.79 mA, while the receiving cantilever was at 0.85 mA (with a current density of $24\mu A/m^2$). These conditions gave an Au migration rate of 5200 nm^3/s and a Si deposition rate of 3500 nm^3/s. The increased Si deposition rate is attributed to the increased rate of Si segregation from the eutectic as Au migrated from the contact site.

However, the increased Si deposition rate was not sufficient to create a straight contact as the Au migrates at a faster rate before enough Si could be deposited.

For the extremely necked case, the observed and expected Si deposition volumes match as shown in Figure 5.14 (b). The value of ϑ in this case is 0.0474 nm/s. It is not clear what merits the agreement between the observed and the expected Si deposition in this case but not the necked and straight case discussed above.

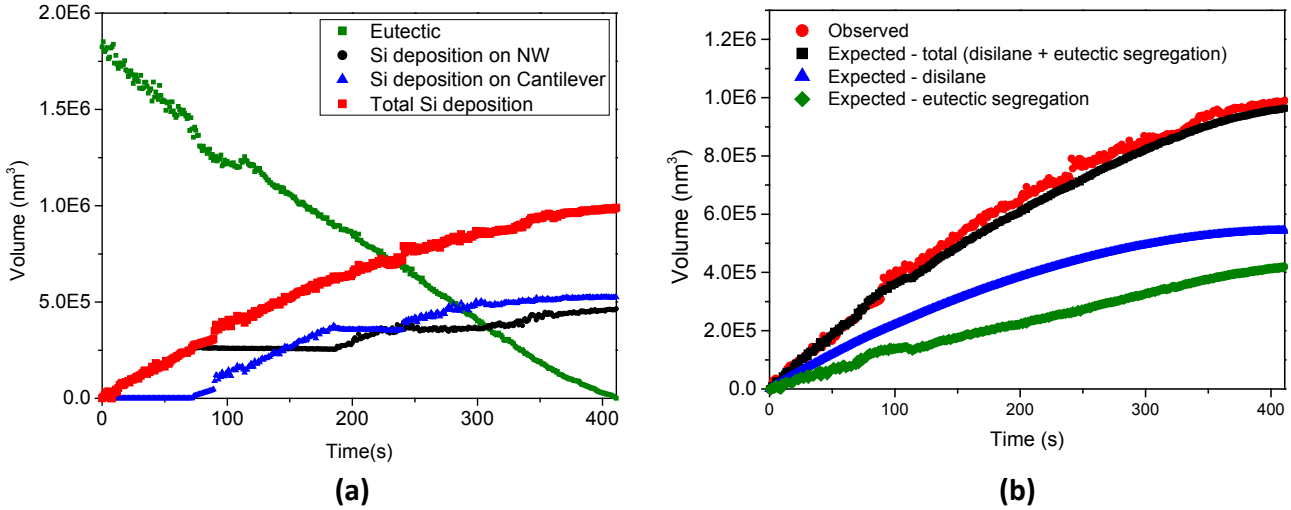

Figure 5.14 (a) Volumetric plots for extremely necked contact formation process of Figure 5.13 and **(b)** comparison between observed and estimated volumes of deposited Si.

In Figure 5.12 (a) and 5.14 (a), it can be seen that the growth proceeds from either the interface on the nanowire side or the cantilever side but only one at a time. In other words, growth halts on one interface during deposition on the other. In the overall dataset no clear correlation with temperature, interface diameter, wetting angles or bias voltage across the nanowire that could predict which interface would be growing was found. It is suggested that Si deposition from the supersaturated eutectic occurs wherever the lowest energy nucleation site for ledges is, and this location may switch from one interface to the other depending on the details of geometry of the changing interfaces.

5.5.4 **Nano gap**

Increasing the temperature and voltage across the nanowire even further created a nano gap, an example of which is shown in Figure 5.15.

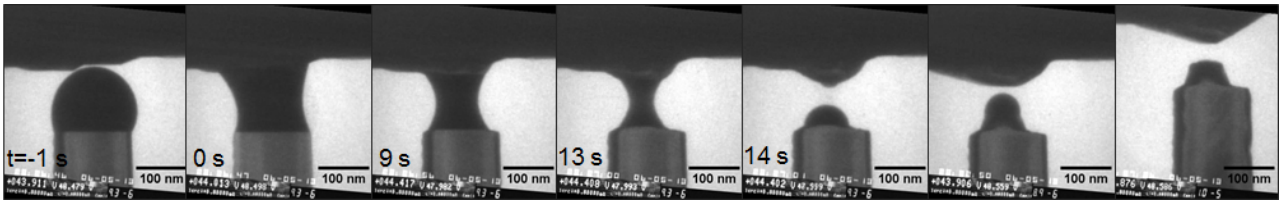

Figure 5.15 TEM image series for nano gap formation

To create this nano gap, the receiving cantilever surface at contact was at ca. 550°C, while the wire was growing at 520°C. Thermomigration was driven by a 1 K/µm temperature gradient along the cantilever and 30 K/µm along the wire, while electromigration was driven by voltage difference of 2.3 V across the nanowire resulting in a current density in excess of 3000 µA/m^2. Rapid shrinkage of AuSi eutectic was observed. The Au migration rate was 1.3x10^5 nm^3/s and it took only 14 s from the initial impact to the point where the hyperboloid shaped AuSi eutectic capillary bridge broke into two droplets, one residing on the cantilever surface and the second on the tip of the wire. According to [77], symmetrical concave capillary bridge stacked between plane surfaces will become unstable and break if $h_e/r_{int} > 1.33$ and $r_m/r_{int} < 0.55$, where h_e is eutectic height of the capillary bridge, r_{int} is the radius of the AuSi eutectic interface (here the smaller interface between cantilever and eutectic is considered) and r_m is the radius of the neck. The last recorded image before the neck breaks is at t=3.947s and is shown in inset in Figure 5.16 (a). For this image, $h_e/r_{int} = 3.05$ and $r_m/r_{int} = 0.50$. It should be remembered that the two Si/AuSi eutectic interface diameters are unequal and unlike the study in [77] the surface of the cantilever and nanowire are not uniform and have physical heterogeneities.

The deposition rates for Si is ca. 35000 nm^3/s, a high rate due to rapid Si segregation and it is 26% of the eutectic shrinkage rate; indicating that for nano gaps, Si only comes from eutectic segregation. The droplet left on the SiNW initiated more growth and made contact with the receiving cantilever again. Since the receiving cantilever conditions were unchanged, a gap was created again, though the gap size became narrower at 30 nm. The droplet left on the wire can be manipulated to create a necked contact if the conditions on receive surface are changed again to promote Si-Si contact (See Figure 7.5(b)).

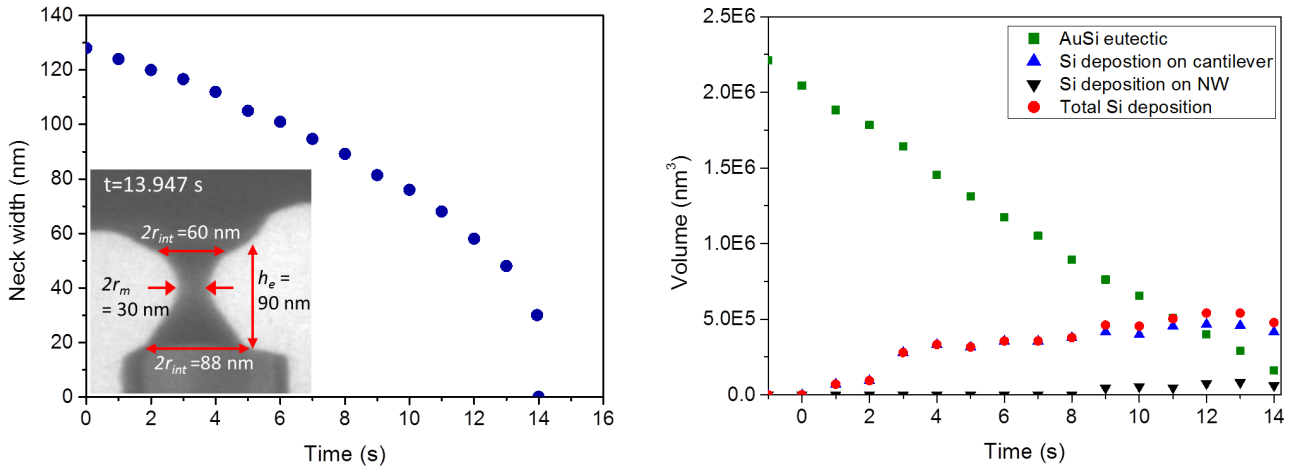

Figure 5.16 (a) Width of the AuSi eutectic neck ($2r_m$) as function of time. Inset shows the TEM image of the capillary bridge at t=13.947s before it breaks. **(b)** Volumetric plots for nano gap formed by increasing the receiving cantilever temperature and voltage.

The rapid shrinkage of AuSi eutectic to create the nano gap is driven by electromigration of Au and not by thermomigration. This was tested by creating a nano gap by reversing the power supply connection of the receiving cantilever. Details of the experiment are given in Append D, Figure D.3.

5.5.5 **Si-Au-Si contact**

If the contact formation process is interrupted, a sandwiched Si-Au-Si contact was created. The contact formation process was suspended by simultaneously cooling the two cantilevers. In Figure 5.17 , it can be seen that the eutectic is stretched from 35 to 65 nm as the cantilevers contract on cooling. Si-Au-Si contact can also be created when the receiving cantilever is cold and at a floating potential as demonstrated in [25].

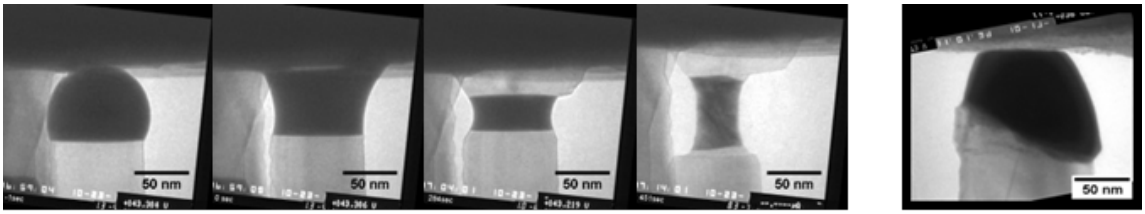

(a) **(b)**

Figure 5.17 Si-Au-Si contact formed by **(a)** terminating the contact formation process midway **(b)** contacting a cold cantilever.

5.6 **Summary**

The structures achieved in this contact formation study are shown in Table 5.1, in which it is summarized that the final geometry of the contact is defined by the competition between AuSi eutectic shrinkage rates and Si deposition rates. In order to avoid repetition, the summary for this chapter and quantitative analysis are presented in the manuscript “Creating new VLS silicon nanowire contact geometries by controlling catalyst migration” in Appendix E.

Table 5.1 Overview of achieved structures

Contact type	Formation conditions	Schematics	Example
Straight Si-Si	**Silicon deposition rate ≈ AuSi eutectic shrinkage rate** For straight contacts, both nanowire and contact site are at similar temperature below 490°C and small current flows through the wire.		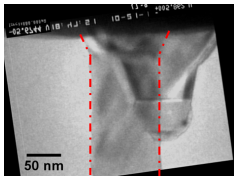
Bulged Si-Si	**Silicon deposition rate > eutectic shrinkage rate** The contact grows with increasing diameter. Created by setting a lower heating current and hence temperature on the receiving cantilever compared to origin. The electron current through the nanowire is towards the origin cantilever.		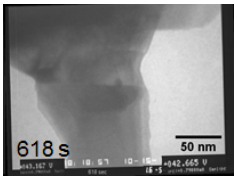
Necked Si-Si	**Silicon deposition rate < eutectic shrinkage rate** When Au migration rate is higher compared to Si deposition; the diameter of the two AuSi eutectic/Si interfaces shrink, leading to necking. Created by high current through the wires and increased contact site temperatures, around 520°C		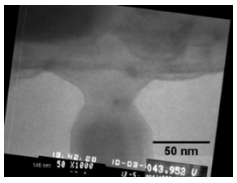
Extremely Necked Si-Si	**Silicon deposition rate << eutectic shrinkage rate** Created by setting a higher Joule heating current on the receiving cantilever compare to origin cantilever, which increases the contact site temperature and voltage across the nanowire, leading to enhanced electromigration of Au.		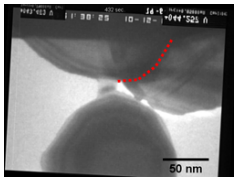
Nano Gap	**Silicon deposition rate << eutectic shrinkage rate** High contact site temperature and a large voltage difference across the wire (leading to electromigration) causes rapid Au migration and a gap is created as Si deposition rate cannot keep up with the AuSi eutectic shrinkage rate		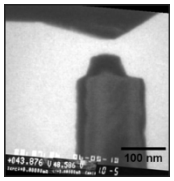
Si-Au-Si type 1	Contact formation process can be stopped any time before completion by cooling the cantilevers to create a Si-Au-Si contact. Eutectic stretches as the microcantilevers contract on cooling.	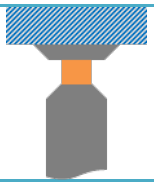	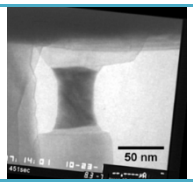
Si-Au-Si type 2	If the receiving microcantilever is cold and grounded, the eutectic freezes immediately upon contact. Si precipitate is formed on the nanowire side.	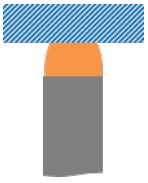	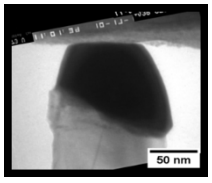

6 Contact geometries by electromigration of catalyst

In the contact formation process, electromigration can be the most dominating mechanism for Au migration. Since temperature and temperature gradients are difficult to measure with higher accuracy, elecrtomigration is the best candidate for a practical approach to controlling the contact geometry as current through the SiNW can be easily controlled.

A benefit of using electromigration to control the contact geometry is that direct observation, as in a TEM, is not essential to create controlled contact geometries. When a SiNW impinges on the contact site, the leakage current that flows through the SiNW, due to the voltage mismatch at the two end of the wire, can indicate the initiation of a contact formation process. A timed controlled increase in current through the SiNW can then reduce the volume of the eutectic to desired contact diameter. Such system can also be used to create controlled nano gaps, without direct observation, where the creation of the gap will be indicated by interruption of current flowing through the SiNW.

In this brief chapter, the different contact geometries that can be created by controlling the electromigration of Au are explored. Here it is demonstrated that by electromigration, nano gaps can be created at relatively low growth temperatures. Moreover, it is shown that electromigration can create contacts of desired diameters.

6.1 Creating controlled nano gaps

Nano gaps, so far, have been created by either shifting the temperature (and hence the voltage) of the receiving cantilever or by flipping the terminals of the receiving cantilever operating at the same temperature. In both scenarios, the creation of the nano gap is due to electromigration but without direct control of the exact current that passed through the wire. Here, the setup shown in Figure A.3 in Appendix A is used to control the current through the nanowire on contact, where the third sourcemeter (V_R) between the adjacent loops defines the reference voltage for one of the loops. When V_R is set to 0 V, the sourcemeter operates as an ammeter and the current though the wire on contact due to mismatch of supplied voltage to the two cantilevers can be measured. However, the value of V_R can be set above or below 0 V to pass a controlled current through the wire.

By adjusting V_R, a nano gap, shown in Figure 6.1 was created for 130 nm diameter wire. Both the wire and the contact site were at ca. 480^{o}C. V_R was shifted to 2 V, to pass a current of 11.5

μA (~850 μA/μm^2) through the wire with the electron current flowing in the direction of the wire and the formation of a eutectic droplet was observed on the surface of the wire (Figure 6.1(b)). Unlike the previous nano gaps, negligible deposition of Si from segregation of the eutectic was observed. The total Si deposited was ~40000 nm^3, which makes only 9% of the eutectic that was removed from the contact site by the time the gap was formed at t=57 s. This is most likely due to lower rate of migration of Au, compared to the cases in Section 5.5.4, which are orders of magnitude higher. The eutectic shrinks at a rate of ~7800 nm^3/s, which is 20 times less than the one recorded for the case in Figure 5.15.

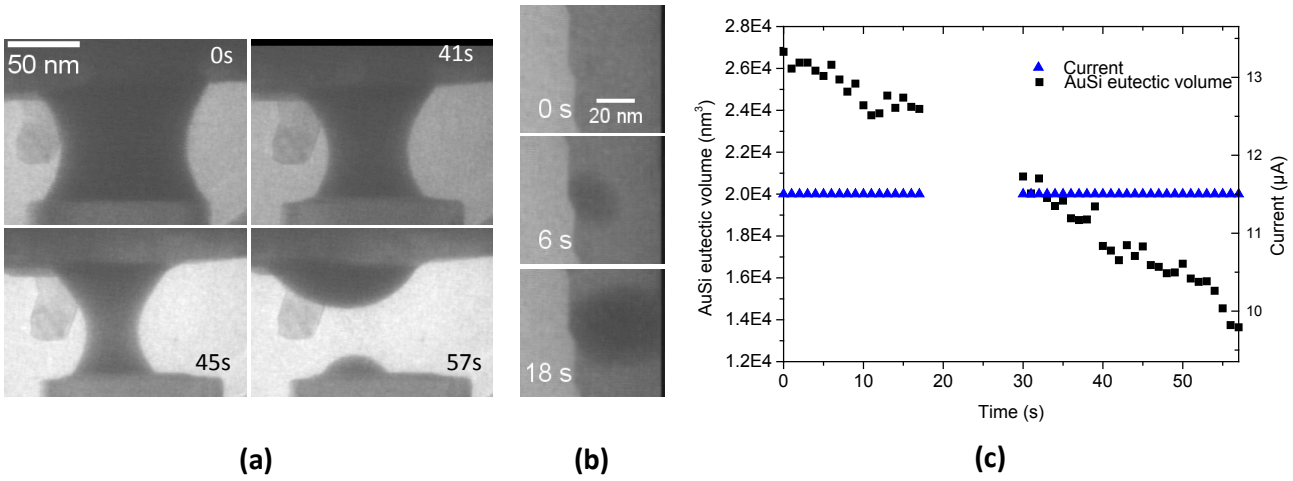

Figure 6.1 (a) Nano gap formation process by passing 11.5 μA current through the wire. Both ends of the wire were at 480^{o}C. **(b)** Formation of AuSi eutectic droplet on the wire surface when the Au from the contact site is forced to migrate over the wire surface in the direction of electron current, and **(c)** AuSi eutectic volume and current through the wire plotted against time for nano gap formation experiment.

For the above nanowire, the gap size was defined by the diameter of the wire; for larger wires, at the moment of initial contact, the growth interface at the nanowire side is further away from the cantilever. To create narrower gaps of desired dimension, contact formation must be allowed to continue so that the growth interfaces are closer to each other. Figure 6.2 shows the scheme where a 10 nm wide gap was created by elecrtomigration of Au for an 85 nm wide SiNW. To create this nano gap, contact formation was allowed to proceed until the two growth interfaces were 45 nm from each other. Then, at t=287 to 330 s, the disilane pressure was reduced from 14 μTorr to 2 μTorr and the incorporation of Si from gas phase was stopped. The voltage V_R was increased until a significant migration rate was observed. At 436 s mark, with V_R value of 1.5 V, a conventional current of 7.5 μA (current density of 1300 μA/μm^2) passed through the wire in the direction of the origin cantilever. Au was moved in the direction of the receiving cantilever at a rate of 5400 nm^3/s. Meanwhile Si was being deposited on the cantilever side due to segregation from the eutectic at a rate of 1600 nm^3/s, which is 29% of the eutectic rate and hence, shows agreement with the expected composition of the eutectic (23 at.% Si) at the temperature of 480^{o}C within error and knowing that the eutectic is supersaturated. The height of the Si deposited from segregation was 35 nm on the cantilever end, and the difference of 45 nm between the two growth interfaces was reduced to a 10 nm gap. The Au that was moved from the contact site ended at the middle of the wire as

AuSi eutectic droplet shown in Figure 6.2(a), t=497 s. The volume of this droplet is about $5x10^5$ nm^3 and it is only ~30% of the eutectic lost after electromigration started. This indicated that Au was migrating to other parts of the wire/cantilever system as well. Rapid electromigration of Au, as can be seen in Figure 6.2, proceeded for about 50 s, and as the location of the droplet was in the middle of a 2.5 µm long wire, it can be estimated that the Au migration velocity was about 25 nm/s. However, it is not know where the rest of migrated Au goes.

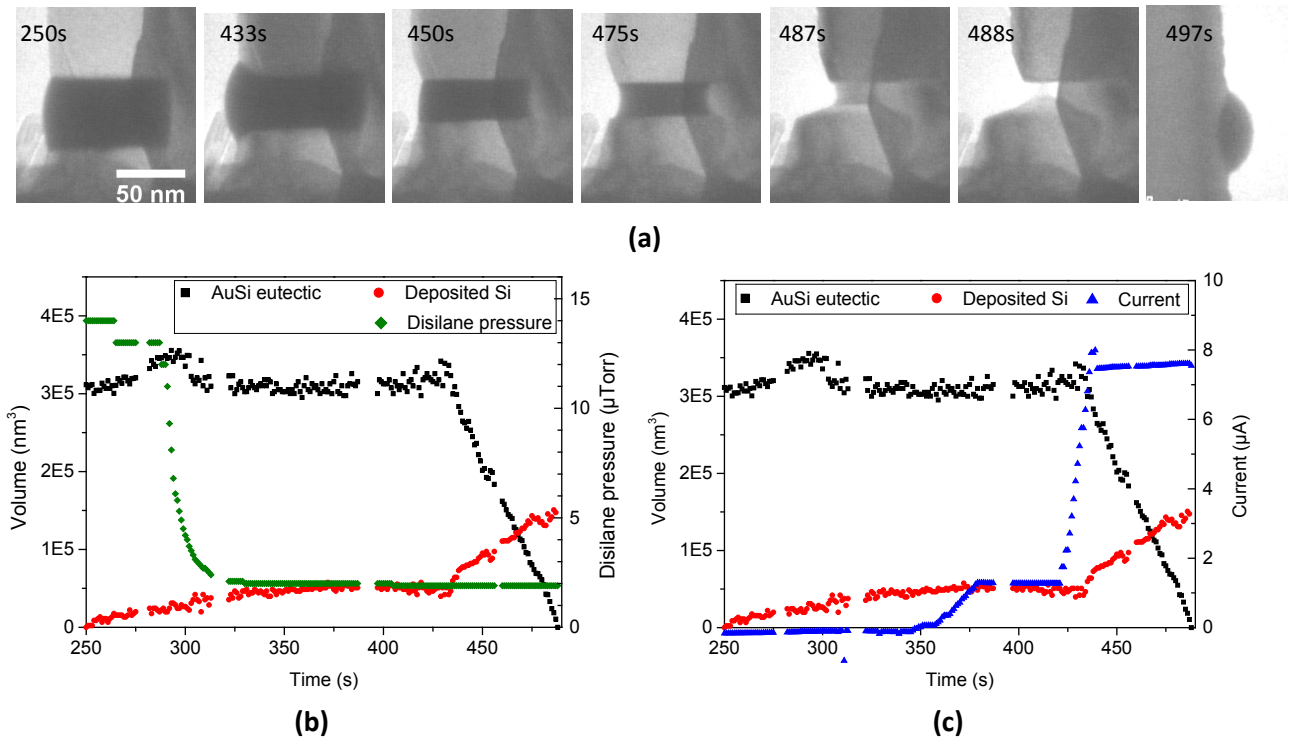

Figure 6.2 (a) TEM image series showing the formation of a 10 nm nano gap, **(b)** and **(c)** volumes of AuSi eutectic and deposited Si plotted along with **(b)** disilane pressure and **(c)** current through the wire against time. In **(b)** the relationship of Si growth to pressure and Si segregation can be seen; incorporation of Si from disilane occurred at high disilane pressure (10 to 14 µTorr) at 530 nm^3/s. When disilane was turned off, there was little if any Si deposition. However, when eutectic shrinks at a rate of 5400 nm^3/s due to electromigration current of 7.5 µA, the Si from segregation was being deposited at 1400 nm^3/s. The difference in the migration rate of Au and deposition rate of Si created the 10 nm gap.

6.2 Controlling contact diameter

Driving Au migration by electromigration can not only create nano gaps as shown above but can also reduce the contact to a desired diameter. Figure 6.3 shows an example, where using electromigration, the diameter of the contact was controllably reduced to 60 nm for a wire with a diameter of 100 nm.

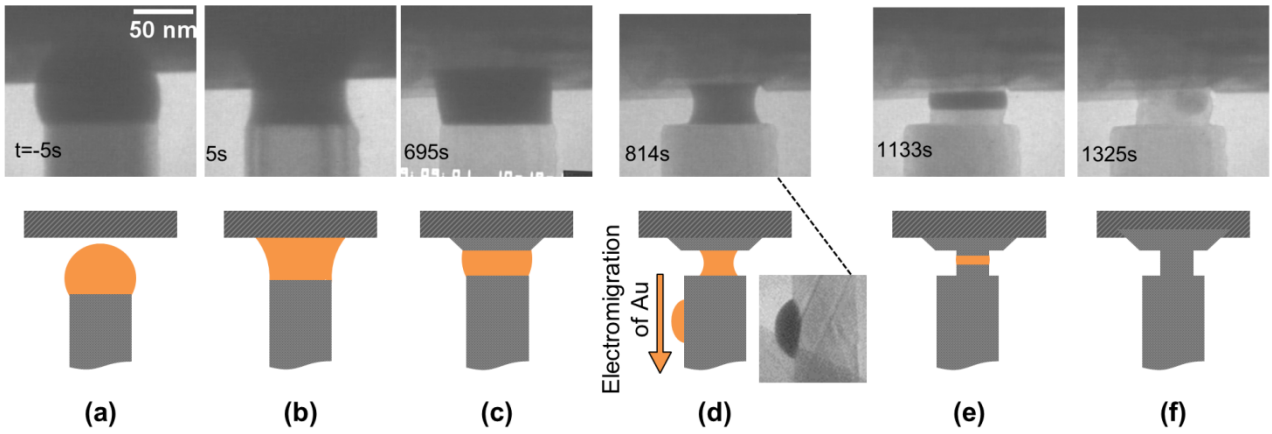

Figure 6.3 Controlled contact diameter created by Au electromigration: **(a)** SiNW before impinging on the receiving cantilever, **(b)** when wire makes contact with the receiving cantilever, **(c)** before passing controlled current through the wire, contact formation is proceeding to create a bulged contact. To reduce contact diameter, first Si growth is terminated by turning off disilane gas and **(d)** current is passed through the wire (with electron current in the direction of origin cantilever) that drives the Au migration over the wire surface, hence shrinking the eutectic volume at contact site and reducing the growth interface diameters, **(e)** disilane supply is restored and the reduced AuSi eutectic catalyses Si deposition to form a **(f)** contact with a smaller diameter compared to the wire.

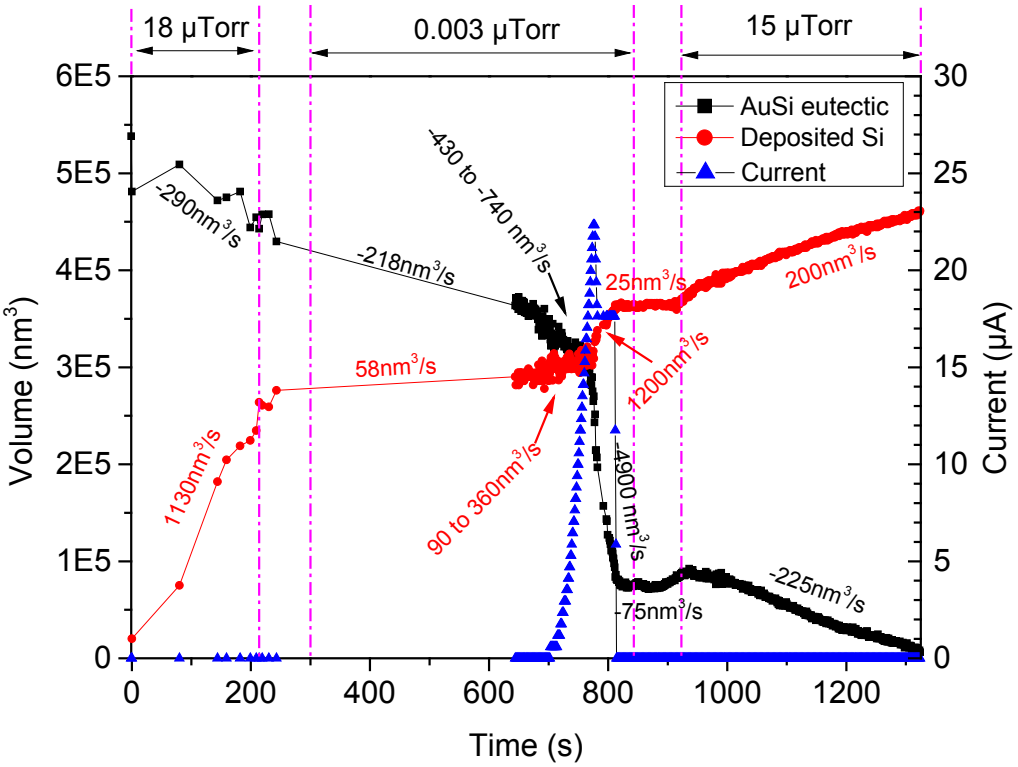

Figure 6.4 AuSi eutectic and deposited Si volumes plotted against time. The current through the SiNW during contact formation is plotted as well. During the contact diameter reduction experiment, disilane pressure was changed at different stages. Pressure values are indicated on the top. The shrinkage rates of eutectic and deposition rate of Si at different stages are indicated as well.

In the controlled contact diameter experiment of Figure 6.3, the SiNW and the contact site were at a temperature of ~475°C. In the early stage of the contact formation process (till t=214s) with V_R=0V, the eutectic shrinkage rate was 290 nm^3/s while Si deposition was at a much higher rate of 1130 nm^3/s with disilane pressure of 18 μTorr. If growth was allowed to proceed uninterrupted, the outcome of initial Au migration and Si deposition rates would have been a bulged contact. To reduce the contact diameter, first Si deposition was stopped by cutting the disilane supply while the cantilever temperatures were kept unchanged. The pressure was reduced from 18 to 0.003 μTorr and the system was kept in this state till t=702 s. There was migration of eutectic when disilane is turned off, at a slow rate of ~220 nm^3/s; indicating that the contact can be necked by lowering disilane pressure. Gradually, the voltage V_R across the SiNW was increased until a noticeable migration rate for eutectic was recorded. At a voltage difference of V_R=3 V across the SiNW, rapid eutectic shrinkage at a rate of 4900 nm^3/s was recorded. The electromigration of Au was driven by a current of 27 μA with density of 3700 $\mu A/\mu m^2$, and it moved Au in the direction of electron current over the SiNW towards the origin cantilever and reduced the eutectic volume in Figure 6.3(c) to one in Figure 6.3(d) in 45 s. At the same time, Si was being deposited at a rate of 1200 nm^3/s, which is 25% that of eutectic shrinkage and agrees with the composition of the eutectic at 475°C in the PD within error.

One of the two AuSi eutectic droplets that were created on the suspended part of the SiNW by migrating Au atoms along the wire during the diameter narrowing is show in Figure 6.3(d). Once the voltage across the SiNW was set to 0 V, disilane pressure was restored at ~15 μTorr and a narrowed Si-Si contact formation proceeded as shown in Figure 6.3 (e). During this phase, the eutectic shrinkage and Si deposition rate were similar, about 200 nm^3/s and resulted in the formation a straight contact with a reduced diameter of 60 nm (Figure 6.3(f)). Since the temperature and pressure were identical, a comparison of the deposition and migration rates for 60 nm section of the contact with initial rates (before applying current) for 100 nm shows that the Au migration has a dependence on the contact diameter and hence circumference where the Au atoms detach from the eutectic catalyst (also see case in Figure D.4, Appendix D).

The migration of Au over the SiNW appears to be through an Au monolayer on the nanowire surface as two non-moving droplets of eutectic, one shown in Figure 6.3(d), increased in size on the nanowire during the migration. The location of the droplets on the SiNW is given in Figure 6.5. When more electromigration of Au was allowed to happen once the contact was created, Au from the neighbouring nanowires migrated to the SiNW surface (See Figure D.5, Appendix D). These droplets were closer to the receiving cantilever end and could initialize SiNW growth on the wire surface. Such systems, with one branching nanowire growing on the surface of another nanowire are interesting for fabrication of nanoscale bio FET (field effect transistor) with nanotube probes [78].

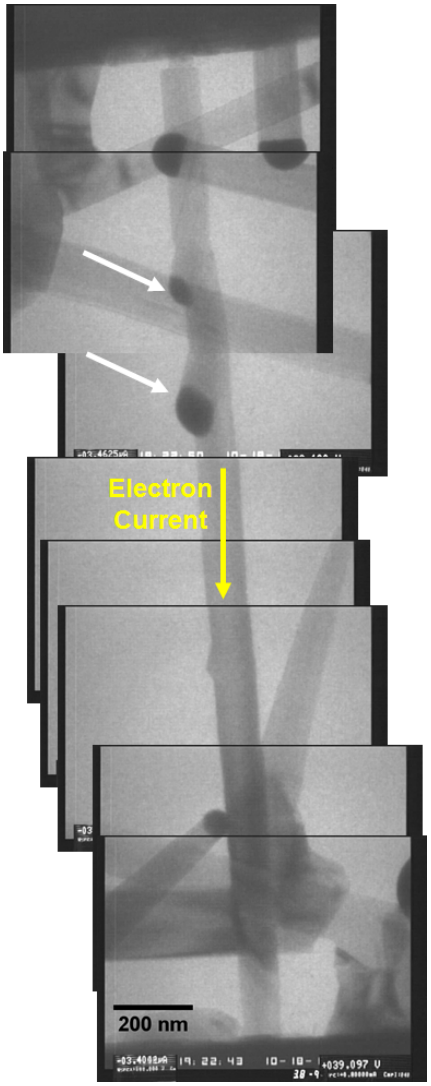

Figure 6.5 TEM images showing the SiNW for which the contact diameter was reduced by electromigration. Two AuSi eutectic droplets that appeared on the SiNW when eutectic was removed from the contact site and transported onto the SiNW can be seen.

6.3 Summary

Here it is demonstrated that electromigration was the most reliable method for creating controlled contact geometries. Au was removed from the contact site through electromigration by passing a current through the wire. The nanowire current was controlled by a sourcemeter connected between the adjacent cantilevers. With current densities in the range of 800 to 4000 $\mu A/\mu m^2$, Au could be shifted at rates of 3000 to 8000 nm^3/s to create contacts of desired geometry. Here nano gaps only 10 nm wide were created and the contact diameter was controlled to desired dimension. The Au that migrated from the contact site, if

moved on the surface of the wire, created AuSi eutectic droplets on the wire that increase in size as the electromigration of Au from the contact site continued. The Au migration was through the Au monolayer on the SiNW surface.

7 Electrical characterization of SiNW

In situ TEM electrical characterization can enhance our understanding of nanowires as we can establish quantifiable direct correlation between composition/ structure and the electrical characteristics. On completion of the self-assembled contact, the SiNWs were electrically connected between the two electrically isolated cantilevers. This enabled investigation of the electrical properties of the SiNWs *in situ* TEM. Since the wires were connected between microheaters, current-voltage (I-V) measurements on the wires were performed at high temperatures and the resistivity of the nanowires for different temperatures was obtained.

The creation of electrically connected pristine SiNW bridges *in situ* TEM allows real-time observation of the effect of introducing a reactant gas on the composition and structure of SiNW surface and the subsequent effect on its electrical properties. Such measurements will be very useful in the field of SiNW photovoltaics or biosensors where nanowire surface state plays a key role in degradation of functionality. Here, an opportunity to study the effect of oxidation on the I-V behaviour of the nanowires for different levels of surface oxidation, by gradually introducing oxygen in the TEM column, was explored. The electrical characteristics of the nanowires were then correlated with the surface composition of the oxide.

7.1 I-V characterization of SiNW

I-V characteristics measured for five nanowires, W1 to W5, are shown in Figure 7.1. These measurements were conducted at room temperature in *situ* TEM on silicon dioxide free SiNWs with roughly 1/3 monolayer of Au on the surface.

Theses nanowires exhibit a nonlinear (non-Ohmic) behaviour and are fairly symmetric between positive and negative values of the supply voltage. One possible explanation of the non-linear I-V of high aspect ratio and low doped nanowire is that the electrical transport is space charge limited (SCL) [79]. In bulk insulators and semiconductors, SCL current leads to a non-linear exponential relationship of $I \propto V^2$ and is associated with situations where the effective carrier concentration is low and transport is dominated by mobility. This situation can arise, for example, due to charge traps, low intrinsic doping or depletion widths at the contact that are larger than the channel length [79]. Thin nanowires have features that make them susceptible to SCL effects; due to large surface area of nanowires carrier-depletion due to surface states is expected to be more and electrostatic screening in high-aspect ratio systems is poor leading to ineffective screening of injected carriers.

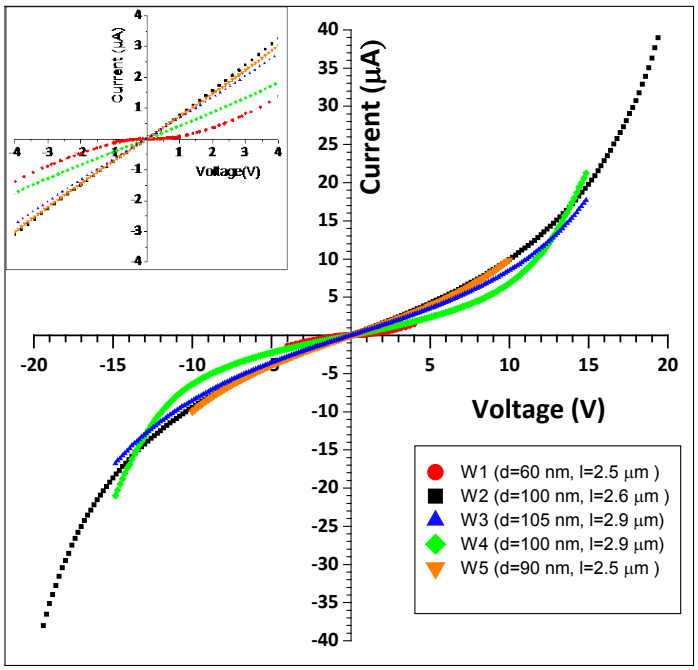

Figure 7.1 I-V data for the wires W1 to W5 measured at room temperature *in situ* TEM. Inset shows the I-V characteristics of the wires for voltage range of -4 to 4 V only. Wire diameter (d) and length (l) are mentioned in the legends.

For SCL effect to be present in the SiNWs, their I-V characteristics must obey the $I \propto V^2$relationship. I-V curves of the SiNW were fitted for the expression: $I = aV^b$ and the fitted parameters are presented in Table 7.1

Table 7.1. Values of the fitting parameter $\boldsymbol{a}$ and $\boldsymbol{b}$ for the relation: $\boldsymbol{I = aV^b}$

Wire name	Diameter d, (nm)	Length l, (µm)	a	b	R.sqr
W1	60	2.5	$9.373\text{x}10^{-8}$	1.948	0.998
W2	100	2.7	$1.153\text{x}10^{-7}$	1.927	0.984
W3	105	2.9	$2.663\text{x}10^{-7}$	1.528	0.994
W4	100	2.9	$2.521\text{x}10^{-8}$	2.468	0.981
W5	90	2.5	$4.167\text{x}10^{-7}$	1.381	0.994

From Table7.1, it can be seen that W1 with the smallest diameter fits well for the relationship $\propto V^2$. For other wires, the value of the exponent b ranges from 1.3 to 2.4, with the fits not following the I-V curves for small voltages. However, for saturated carrier velocity, the SCL relationship for semiconductors becomes: $I \propto V^1$, and in the ballistic regime (not likely for SiNWs with diameters of 60 to 100 nm) with no scattering $I \propto V^{3/2}$. Hence, depending on the case, a power law with exponent in the range 1-1.5-2 can indicate SCL transport but the situation is complex if the transport is not fully space charge limited, e.g. partly in the Ohmic regime, or if the 1/3 monolayer surface coating of Au provides a parallel conduction channel

that will have different characteristics than the silicon of the nanowire itself. SCL transport has a dependence on the length l of the device given as : $I \propto l^{-3}$ and for velocity saturation case as $I \propto l^{-2}$. Hence I-V measurements of SiNWs with significantly different lengths could help in determining SCL transport existence. Unfortunately, the gap between the adjacent cantilevers, in this work, ranged from 2.5 to 2.9 µm, which is not a big enough range. Attempts were made to probe the SiNWs of different length at the tip of the cantilever with a metal probe in a scanning electron microscope (SEM). However, the experiments were challenging and I-V measurements with wires that were touched with the probe did not give any useable results.

It was found that the best fit to the I-V curves with few fitting parameters was a hyperbolic sine function of the form $I = Asinh(V/V_o)$ and it is fitted for the Wire 2 case in Figure 7.2.

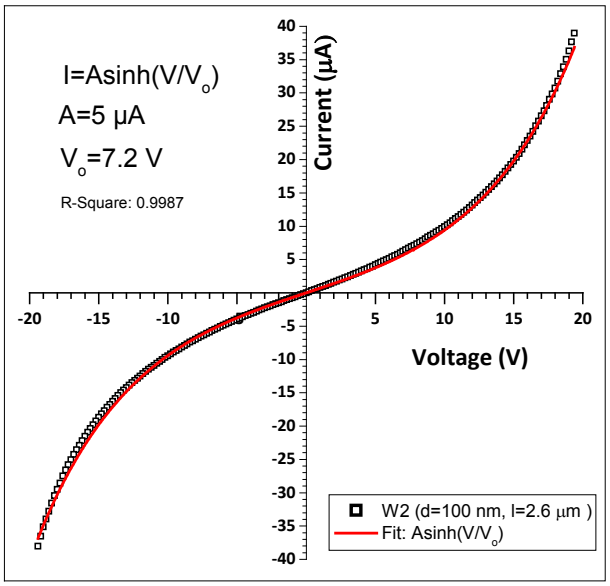

Figure 7.2 I-V characteristics of wire W2 with fit for the function: $I = Asinh(V/V_o)$

Though the hyperbolic sine function gives the best fit for the lowest number of fitting parameters, a description of a physical process that would result in such a relationship at room temperature is lacking. Currently, work is in progress at the MoWin Group to develop a model that can explain the adherence of the I-V characteristics to the hyperbolic sine function.

Four point measurements were performed on few wires at room temperature at low currents (in the range of 5 µA) to obtain a resistivity of ~0.32 Ωcm. If it was assumed that the nanowire behaved as bulked Si, with no surface effects and has a p-type dopant, for the obtained resistivity, the SiNW would have a doping concentration of ~5x10^{16} cm^{-3}. With increase in temperature, the carrier concentration is expected to increase (Figure 3.4(a)). A possible source of dopants is the boron atoms in the cantilever that can be incorporated in the SiNW through the AuSi droplet that forms initially on the cantilever surface. Another source of dopant is the disilane source which has a purity of 99.998% with trace amounts of diborane at 100 ppb which can serve as sufficient source of boron for doping a SiNW [25].

The incorporation of the catalyst metal in the interior of the VLS nanowire can alter the nanowire properties and is hence an unwanted consequence of epitaxial growth if it cannot be controlled. Fortunately, the solubility of Au in Si is extremely low: 10^{-9} Au atoms per Si atom at 600°C [63]. Hence, significant incorporation of Au atoms inside SiNWs is not expected.

7.2 I-V characteristics at high temperatures

To study the dependence of SiNW resistivity on temperature, I-V measurements were performed on bridging nanowires while the two cantilevers were operating in the growth temperature regime. This was accomplished by the sourcemeter V_R connected between the cantilevers. Figure 7.3 shows the I-V characteristics of the SiNWs at elevated temperatures.

The I-V measurements at high temperatures show that the behaviour becomes linear as temperature was raised, which is an expected result for nanowires that exhibit SCL transport [80]. From the IV measurements, the resistivity of SiNWs at different temperatures can be extracted and is plotted in Figure 7.4

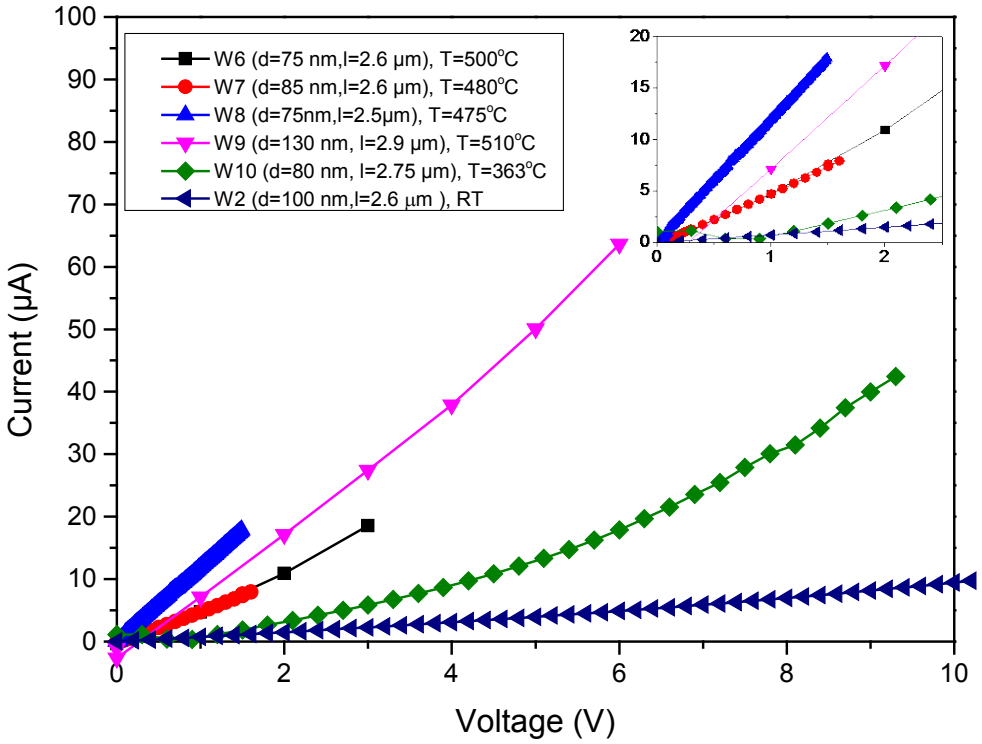

Figure 7.3 I-V characteristics of SiNW at different temperatures. W2 is at room temperature (RT), W10 is at eutectic temperature of 363°C, while W6 to W9 are in growth temperature regime. Inset shows the I-V characteristics up to 2 V.

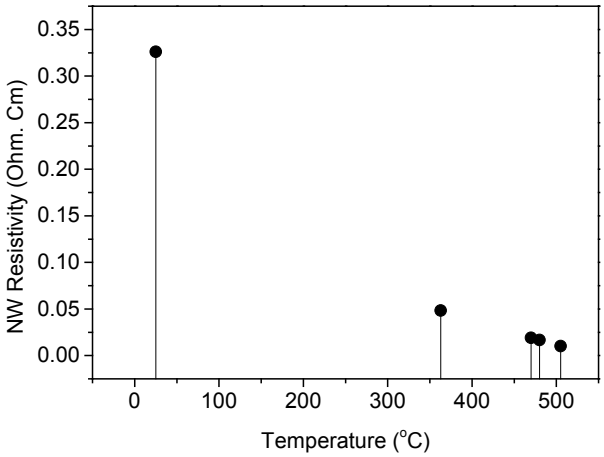

Figure 7.4 SiNW resistivity vs. temperature

7.3 Surface oxidation

The high surface to volume ratio of SiNW means that surface conditions play a very dominant role in defining electrical properties. This also means that issues like surface passivation become important for SiNWs. Si processed in ambient has a native oxide layer on the surface that will affect its electrical properties. Fabricating electrically connected oxide free SiNWs *in situ* TEM allowed the examination of I-V characteristics of the SiNW as its surface was gradually oxidized (Figure 7.5).

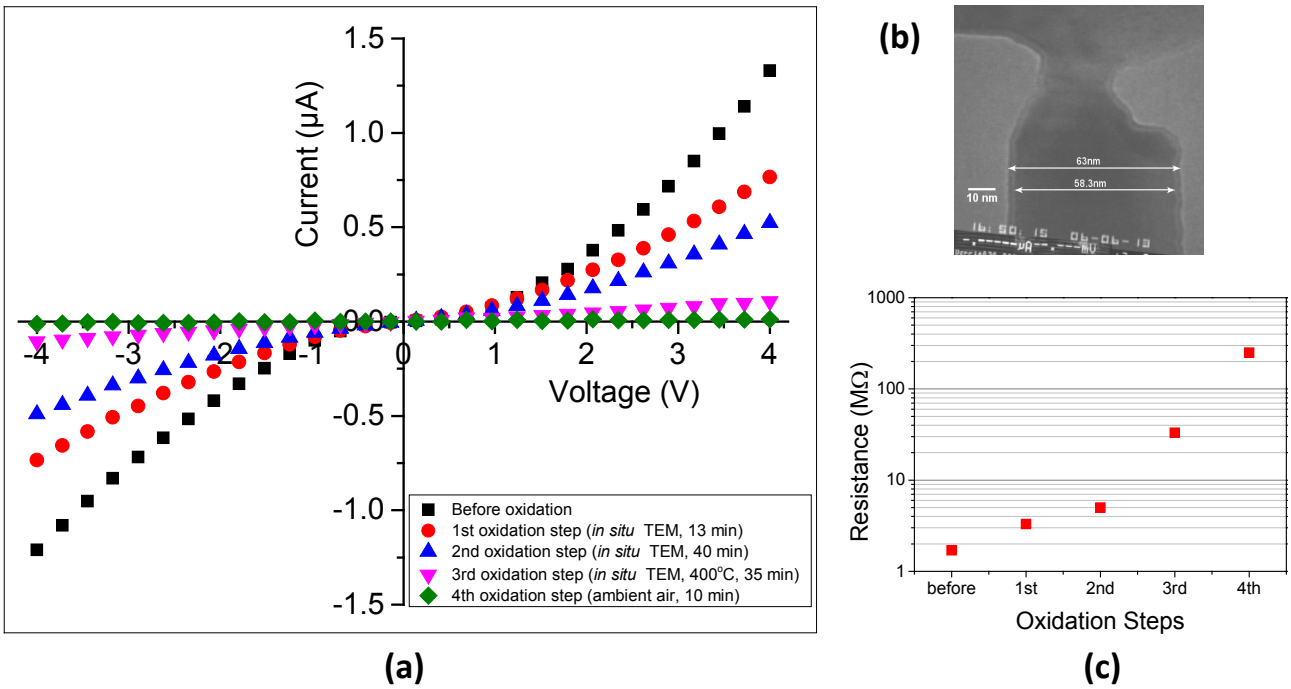

Figure 7.5 SiNW surface oxidation experiment: **(a)** I-V characteristics recorded after each oxidation step. **(b)** SiNW contact with oxide layer visible after 4th oxidation step and **(c)** resistance of SiNW after each oxidation step.

Four oxidations steps were performed on the nanowire W1, which is ~60 nm in diameter and 2.5 μm in length. The first three oxidation steps were in the TEM and the last was in ambient atmosphere. Details of each step are below:

- Oxidation step 1: For about 13 minutes, oxygen was introduced in the TEM. Oxygen pressure was in 10^{-7} Torr range.
- Oxidation step 2: About 40 minutes long. O_2 pressure was in 10^{-7} Torr range.
- Oxidation step 3: This oxidation step was also done *in situ* TEM. The two cantilevers were heated above eutectic temperature and oxygen was introduced in the TEM ($P=2x10^{-7}$ Torr). This oxidation step was about 35 minutes long.
- Oxidation step 4: The sample was taken out of the TEM for 10 minutes to grow a native oxide. Figure 7.5(b) shows the oxide layer after the 4^{th} oxidation step. The oxide layer was about 3 nm thin.

The significant decrease in the nanowire conductivity after each oxidation step can be attributed to oxide trapped charge that effect the electrostatic boundary conditions of the nanowire and can create a depletion region in the wire [81]. Also, the surface states at the Si/SiO_2 interface are amphoteric, i.e. they can act as acceptors and donors and the carriers that are trapped by the surface states are provided by the underlying Si, which means that the Si near the surface is depleted of carriers and a depletion region is formed near the Si surface. The presence of a depletion layer will cause the conductive channel cross section of the SiNW to be smaller than its physical cross section and the resistance of the wire will decrease [81].

The second effect that can increase the conductance of SiNWs is that the roughly 1/3 Au monolayer on the SiNW breaks into islands on oxidation as shown in Figure 7.6. It is likely that the monolayer of Au on SiNW provided a second pathway for current flow on the nanowire surface in addition to transport through the bulk.

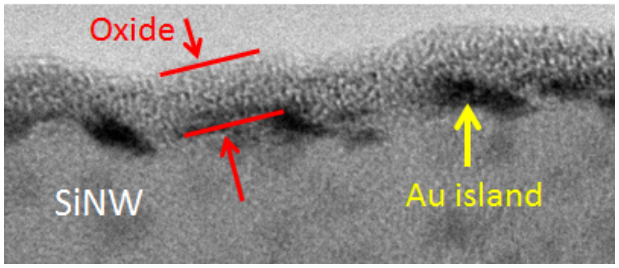

Figure 7.6 TEM image of SiNW surface after exposure to the ambient atmosphere. A 3-5 nm native oxide and the underlying Au islands on SiNW surface can be seen.

7.4 High electric field experiments

The voltage V_R can be increased to as large as ±150 V, to create a high electric field between the two cantilevers. This setup was used to examine the relationship of eutectic droplet shape to electric field strength and to study the destruction of SiNWs by high voltages.

7.4.1 **AuSi eutectic droplet deformation by electric field**

In the VLS mechanism, the structure of the nanowire is adjusted by changing two parameters: temperature and pressure. However, by adding a third parameter, the electric field, growth parameters like diameter change, contact angle of catalyst droplet and kinking can be modified independently. Here, by applying an electric field using the reference voltage V_R to one of the cantilevers, the droplet shape and consequently the nanowire growth was changed. Figure 7.7 shows the deformation of the droplet when the voltage V_R was shifted between -70 to +70 V.

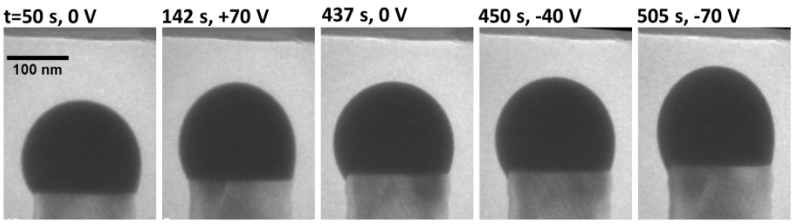

Figure 7.7 Droplet deformation induced by electric field during nanowire growth at 510°C and 5 µTorr disilane pressure.

The deformed equilibrium shape of a droplet is determined by balancing the surface tension and the electric field. Figure 7.8 shows the dependency of the droplet aspect ratio of the case in Figure 7.7 on the applied voltage. A rapid response of the droplet to the direction and strength of the applied field was observed.

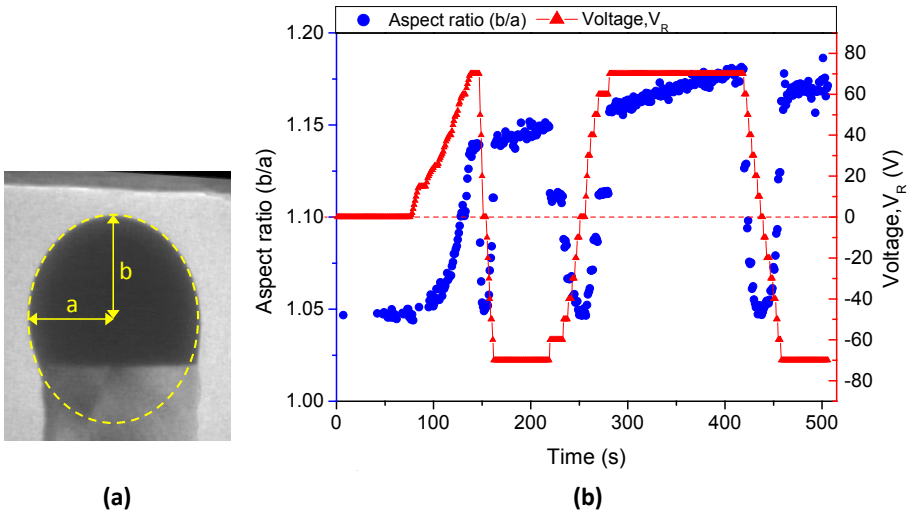

Figure 7.8 (a) Physical dimensions defining the aspect ratio b/a are shown for a deformed droplet **(b)** aspect ratio (b/a) and applied voltage (V_R) as function of time.

Figure 7.9 show that the electric field can stretch the droplet axially with the result to modify the contact angle and therefore the wire diameter. This modification is reversible and it makes possible to modulate the diameter of the wire. The increased surface area of the

droplet and the reduced growing surface of the wire can increase the growth rate; hence an accurate model is necessary to control the modulation.

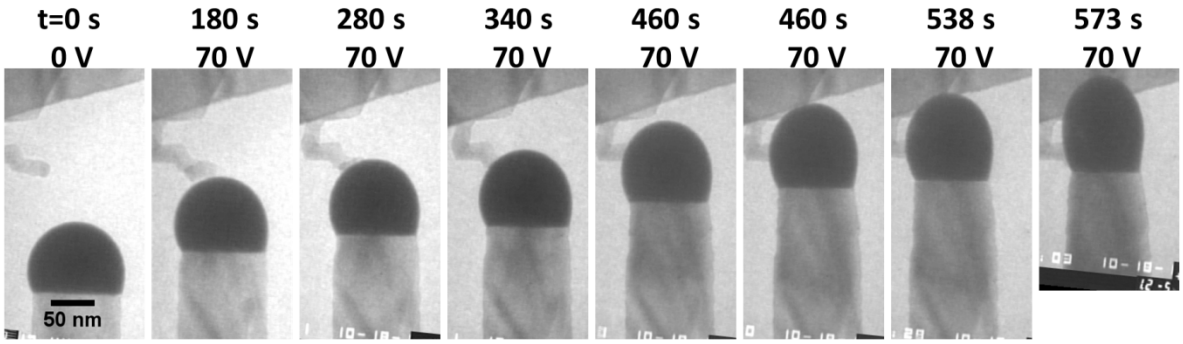

Figure 7.9 Sequence of images showing a wire growing at 480°C and 1.2 µTorr disilane pressure with an applied voltage of V_R=+70 V. As the wire approaches the counter electrode (receiving cantilever), its diameter is getting smaller. At t=0s, the wire diameter is 100 nm, which is reduced to 75 nm at t=573 s.

Using high voltage, the AuSi droplet can be stretched sideways and the wire can be kinked in a specific direction. Other methods like introducing oxygen in the system or heating-cooling cycle are used to kink the wires but they cannot force the wire to be kinked in a specific direction. This method could also be used to grow wire in unfavorable directions, e.g., <100>. An initial experiment on changing the direction of growth is shown in Figure 7.10. The wire is growing at 500°C and 17 µTorr disilane pressure. The voltage V_R is set at 150 V and the receiving cantilever is at 70 degree with respect to the growth direction of the wire. The induced electric field caused the growth to switch partially from one <111> direction to another as explained in Figure 7.10.

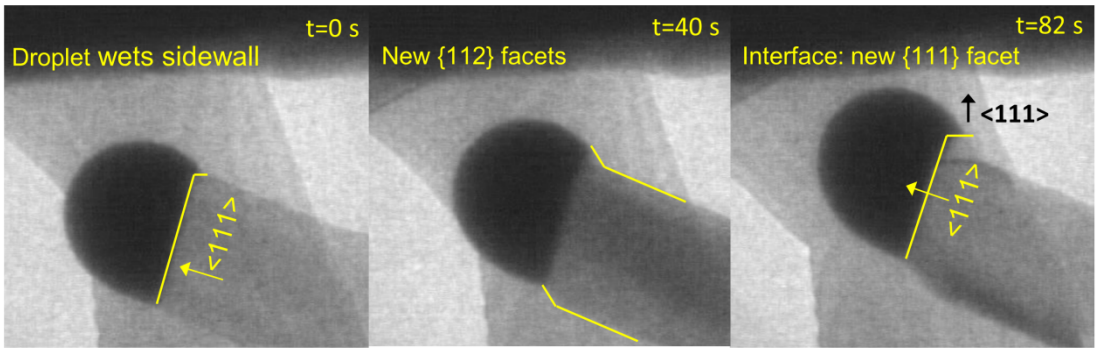

Figure 7.10 Sequence of images showing a SiNW approaching the receiving cantilever at 70 degree angle with V_R at 150 V. The induced field causes the kinking of SiNW. The direction of growth is changing from one <111> direction to another <111> direction. This happens through three stages: **(a)** the droplet is pulled sideways and wets the sidewall of the nanowire, **(b)** the wire develops new {112} lateral facets and **(c)** finally the growing interface becomes perpendicular to the new lateral facets.

At present, further work is being done in collaboration with Federico Panciera at IBM and Michael M. Norton at University of Pennsylvania to use numerical simulation to calculate the electric field around the catalyst droplet and solve the modified Young-Laplace equation in order to obtain the equilibrium shape of the droplet. This will help to define the optimal conditions to induce longitudinal and lateral stretching of the droplet in order to modify the nanowire growth direction through controlled kinking and the wire diameter.

7.4.2 **Plateau - Rayleigh instability of SiNWs**

When subjected to high electric discharge, the SiNW will instantly melt into liquid state but instantly freeze afterwards creating a morphology that is defined by Plateau - Rayleigh instability. TEM images of the SiNW before and after being melted by electrostatic discharge and "flash freezing" are shown in Figure 7.11.

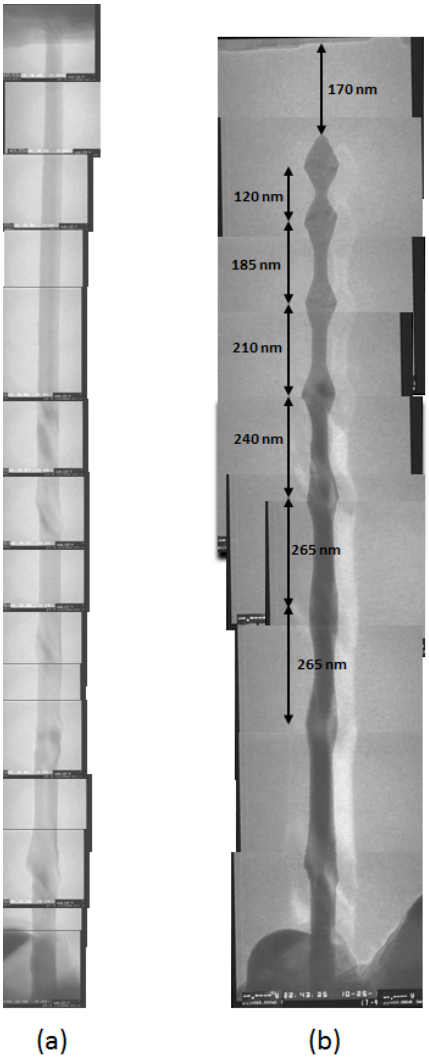

Figure 7.11 **(a)** Before and **(b)** after TEM images of SiNW that melts by high electric discharge and freezes instantly. The wire was liquid during the discharge and froze immediately and the resulting morphology is a "snapshot" of the geometry of the molten SiNW defined by Plateau-Rayleigh instability. The wavelengths of the disturbances are between 120 to 265 nm.

For Plateau–Rayleigh instability, the fastest growing mode occurs when $kr_{nw} = 0.697$, where r_{nw} is the radius of the wire and k is the wave number of disturbance. That is when the wavelength of the disturbance is $\lambda = 9.02r_{nw}$. As the wire is tapering with diameters from 40-60 nm, wavelength of the spatial instability of 180-270 nm is obtained, which is in almost perfect agreement with the observation in Figure 7.11, except for the first undulation at the free end. The characteristic beak up time (τ) for the instability is given as :

$$\tau = 2.91\sqrt{\frac{\rho r_{nw}^3}{\gamma}} \tag{7.1}$$

where ρ is the density and γ is the surface tension. The characteristic break up time was calculated to be between 1-2 ns, given the same variation in diameter.

7.5 Summary and outlook

The SiNWs, at room temperature, exhibit non-Ohmic I-V characteristics. For 60 nm wires, this nonlinear behaviour agrees with SCL transport. However, for wider wires it is not clear if SCL effects are present. Interestingly, hyperbolic sine function provides a better fit to the I-V curves but at the moment, it cannot be explained by any physical model. Work is being done, at present, in author's research group to understand this hyperbolic sine trend of I-V characteristics. It is further demonstrated that oxidation can significantly increase the resistance of the nanowires. However, the role that breaking of the Au layer has on SiNWs resistance is unclear. Currently, work is in progress using analytical TEM technique of electron holography to image and determine the depletion regions in the nanowire. However, this is a challenging experiment for a complicated SiNW surface. Electric field was used to control the diameter and growth direction of SiNWs. The morphology of molten SiNWs is defined by Plateau- Rayleigh instability.

8 Conclusions

Nanowires have been extensively studied as the active component in electronic, thermoelectric, sensing and optoelectronic devices with the hope that integration of nanowires will improve the capabilities of these systems. [1]–[6]. The most prominent bottom-up technique for fabricating nanowires is the epitaxial chemical vapour deposition process called the vapour-liquid-solid (VLS) mechanism[64]. The VLS mechanism relies on the super saturation of catalytic liquid alloy between a metal catalyst and the growth material. The continued precipitation and nucleation of the growth material at the bottom of the liquid droplet creates the nanowire geometry with catalyst droplet at the tip.

Fabrication of silicon nanowires (SiNWs) by VLS mechanism has been extensively investigated [60]. To understand the kinetics of the growth process, *in situ* transmission electron microscopy (TEM) has proved to be a valuable tool [34]. In this work, SiNWs were grown in *situ* TEM using Au as the catalyst and disilane as the precursor gas. Due to the imaging requirements of the TEM, the pressures in the column were kept in the range of 10 μTorr that corresponded to growth rate of about 10 nm/s. The growth rate of SiNWs has an Arrhenius dependence on temperature, linear relation to disilane pressure and is independent of wire diameter. SiNWs grown *in situ* TEM had a hexagonal cross section, usually grew in the <111> direction and had periodic "sawtooth" like facets on the sidewalls. The sidewalls have a 0.4 to 0.46 monolayer of Au coverage [66]. The Au for the sidewall is provided by the catalyst droplet at the tip; hence the maximum achievable length of the wires is limited by the volume of eutectic droplet. The coverage of SiNW and the substrate between them by Au enabled Ostwald ripening diffusive process to change the catalyst droplets volume during growth. Ostwald ripening created wires either increasing in diameter due to increase in droplet volume or tapering due to shrinkage of the catalyst. The nanowires studied in this work were 40 to 160nm in width and 2.3 to 3 μm in length.

In situ TEM was used to follow the life of a SiNW from initiation of growth to creation of the contact formed when the wire impinges on a surface, followed with electrical characterization of the wire and ending with destruction of the wire by high voltage. To accomplish this task, SiNWs were grown between two adjacent silicon microcantilever heaters operated through the Joule heating effect. Growth temperatures were in the range of 470 to 530^{o}C, which were achieved by electrical power in the range of 28 to 33 mW. The microcantilever heaters were designed to confine growth temperatures to the upper section of the cantilevers. The thermal gradient over the upper portion of the cantilever depends on the absolute temperature as thermal conductivity of silicon has temperature dependence: thermal gradient ranged from 1 K/μm for maximum temperature of 560^{o}C to about 0.2 K/μm when maximum temperature at the tip is 475^{o}C. Thermal gradient was an important factor to consider during the contact formation experiments and more so for as one of the modes of Au migration: thermomigration is driven by temperature differences. However, for unequal temperatures,

the thermal gradient over the nanowire was much larger than over the cantilevers.

The main focus of the work was to study the contact formation mechanism that follows when a VLS SiNW impinges on an opposing Si surface. This was accomplished by connecting a SiNW grown from a microcantilever heater to the adjacent cantilever. When the impinging wire makes contact with the receiving cantilever, the AuSi eutectic droplet wets the sidewall and its shape is transformed from a semi spherical to a hyperboloid sandwiched between the SiNW and sidewall, which will catalyse further epitaxial growth until a Si-Si contact is created. SiNW cantilevers were effective platforms for studying contact formation process as the temperature profile and voltage distribution of the receiving cantilever was controlled. It was demonstrated that by adjusting the temperature and the voltage across the nanowire, the geometry of the final contact could be controlled by tuning the balance between the migration and diffusion of Au and deposition of Si.

Controlling the balance of Si deposition vs. Au migration and diffusion created a variety of geometries including Si to Si contact, a nano gap or a Si-Au-Si contact. Different types of Si-Si contacts were created: straight contacts originate when AuSi shrinkage and Si deposition rate are almost similar, bulged Si-Si contacts are created when Si deposition rates are much higher than AuSi volume loss, while necked contacts are created when AuSi shrinkage rates are higher than Si deposition. The Si deposition rates were in the range of 500 to 3500 nm^3/s for Si-Si contacts, depending on wire diameter, contact surface temperature and pressure. Si deposition rate are also influenced by the Au migration since removal of Au from the AuSi resulted in the segregation and deposition of Si at the contact site. This situation was obvious in the process of creating nano gap contact geometries, which are created by rapid Au migration due to electromigration. The Au migration rate for creating nano gaps is two orders of magnitude higher than migration rates for creating Si-Si contacts. Migration rate is fast enough that there was not sufficient time to create the Si-Si contact and the segregation of Si from the eutectic is also fast, resulting in deposition rates that can be an order of magnitude higher than Si-Si contacts.

Electromigration of Au can be controlled to alter to the contact geometry. It was established electromigration is the most dominant and the best candidate for controlling contact geometry by catalyst migration. It was observed that not only Au but AuSi eutectic can also migrate in the direction of electron current, which has been demonstrated by previous studies on electromigration. In addition to creating nano gaps, the cross sectional area of the contact was controlled by removing a part of the eutectic and allowing the remaining eutectic to catalyse further growth.

Once the SiNW contacts are created, I-V measurements can be performed on the SiNWs. It was found that the I-V behaviour is extremely non-linear following a hyperbolic function (*sinh*) fit. It is demonstrated that the electrical properties of the SiNW can be changed by changing the surface conditions. The surface of SiNW was oxidized to increase its resistance from 10 to 100s of MΩ.

The shape of the eutectic droplet can be deformed by high electric fields. This gives an additional parameter to control the growth direction and diameter of SiNWs.

8.1.1 **Outlook and future work**

Integration of thermally, electrically and mechanically connected SiNWs grown by VLS mechanism in device architecture *in situ* CVD reactor requires the contact formation process studied in this work. This work demonstrates that the contact formation process has intricate kinetics and by controlling the surface conditions, the geometry of the contact can be controlled as required by the device design. The geometries are interesting for different applications: Si-Si contacts are clearly essential for all electrically connected devices whereas the nano gap architecture can be used for field emission sensors. The introduction of an ammeter in the system can enable identification of a contact event without visual inspection. Hence, it might be possible to create different contact geometries on a single device without need for visual tracking.

An electrically connected SiNW bridge created *in situ* TEM is an interesting platform for studying surface treatment effects on the electrical properties. To complete the electrical characterization of Au decorated SiNWs further experiments are required: starting with performing the *in situ* oxidation experiment again but creating the oxide layer while simultaneously measuring the SiNW resistance and this is followed by removing the oxide to test if the post oxide growth resistance can be restored. At present, current efforts on understanding the non-linear I-V behaviour involves studying the SiNWs *in situ* an analytical TEM by electron holography to map the electric field of biased SiNWs. However, the first experiments demonstrated that Au decorated wires are challenging samples for holography experiments. Research is also underway to fabricate Au free SiNWs by e-beam lithography and measure these wires after removing the oxide to compare their properties to VLS SiNWs.

The microcantilever heaters proved to be very stable platforms for growing 3 μm long nanowires. Using the fact that growth temperature on microheaters is localized, post processing integration of individual SiNW grown by VLS method to CMOS devices and lab-on-chip with polymer fluid channels can be made possible. This is not possible with standard epitaxial growth systems like CVD reactors where the entire device is exposed to growth temperature that far exceeds the limit for CMOS (450^{o}C) and polymers (100-150^{o}C).

Eutectic sandwiched between Si is also a very interesting platform for studying the fundamental properties of electromigration of metals at high temperatures. This is because the 2D projected geometry of eutectic stacked between two silicon surfaces can be estimated easily, while droplet shapes lying on a substrate are harder to judge in a TEM.

Appendix A

Microcantilever designs

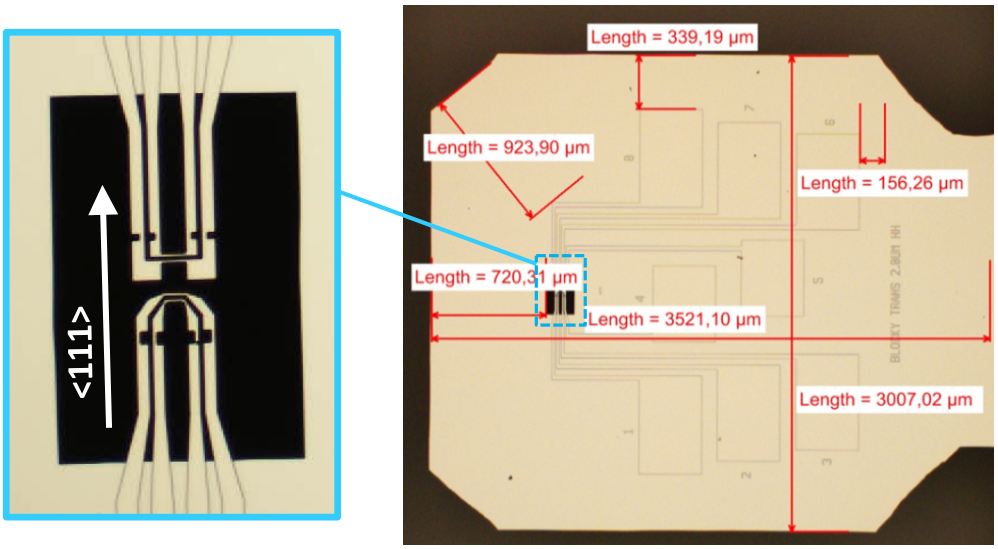

Figure A.1 Chip with "loop in loop" microcantilever design. The <111> crystal direction is indicated.

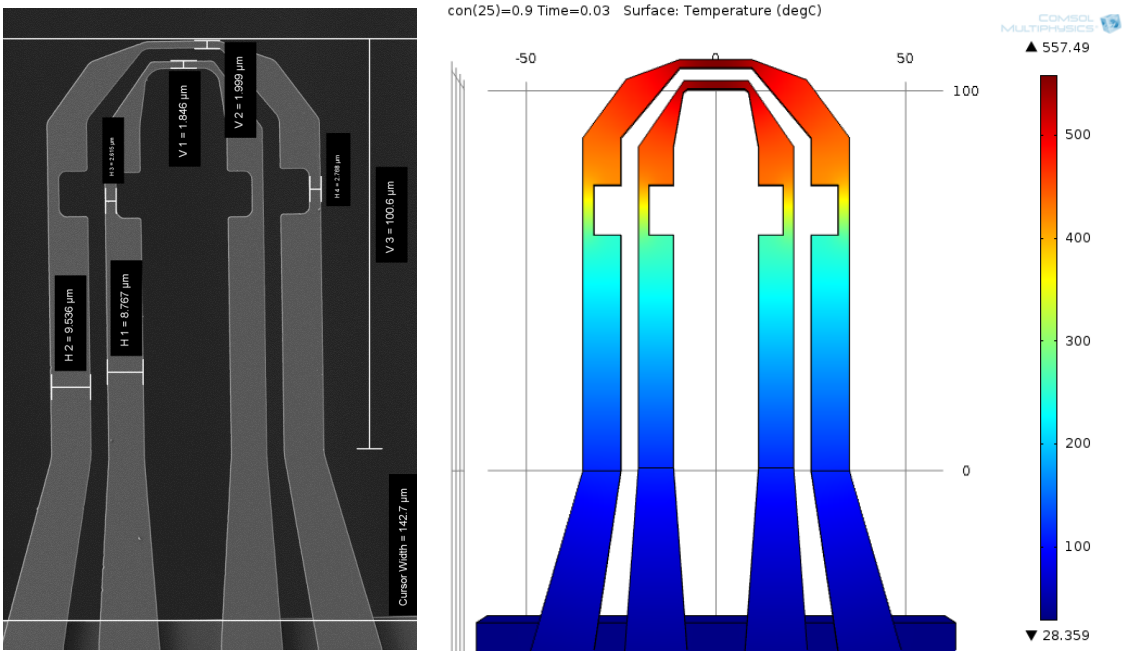

(a) (b)

Figure A.2 (a) SEM image of one of the loop in loop cantilever design. **(b)** COMSOL simulation result of the temperature profile of the loop in loop design.

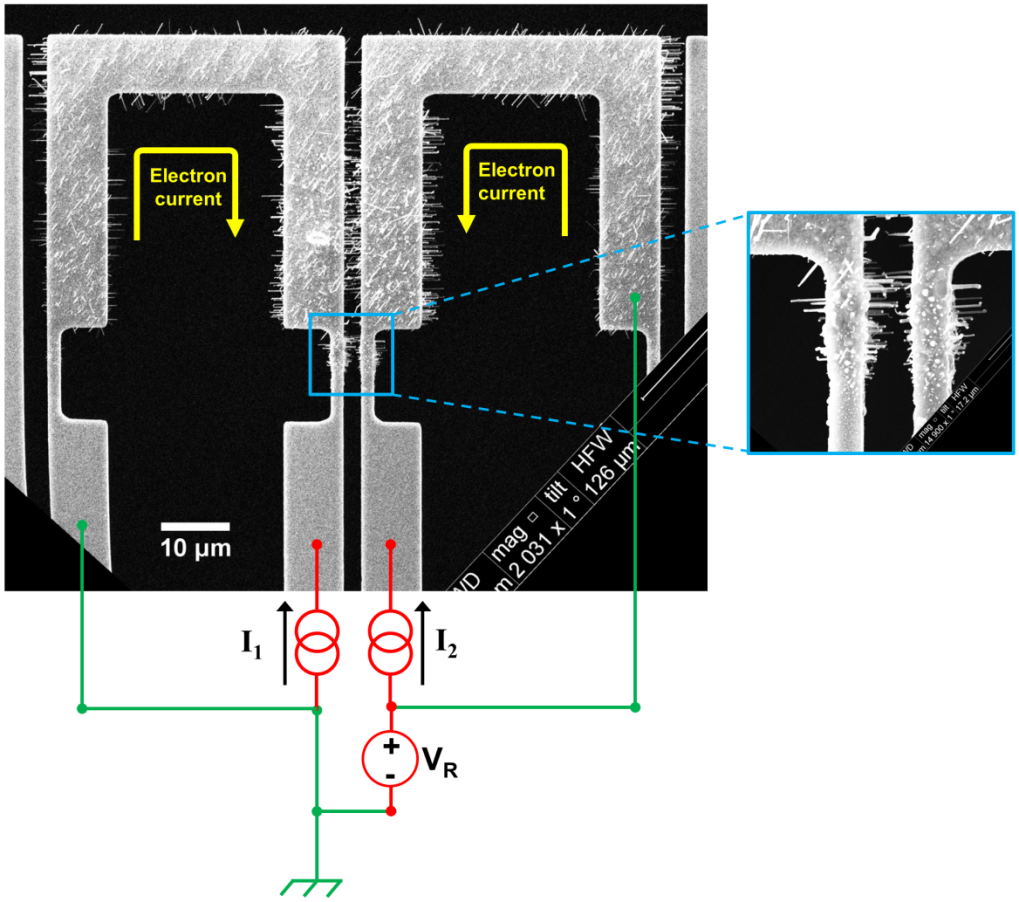

Figure A.3 SEM image of microcantilever heaters with SiNWs grown on them. The cantilever heaters were operated by constant current source as shown by the connections. The direction of the electron current is opposite to the conventional current. The difference in nanowire density between the microcantilever legs connected to the ground and positive terminal can be seen. Electromigration will move Au towards the positive terminal depleting the cantilever legs connected to the ground/negative terminal. The Keithley SourceMeter V_R is used to set reference voltage for the cantilever on the right. With V_R set to 0V, it operates as an ammeter and measures the current through the bridging SiNW but values of V_R can be changed to control the amount of current through the wire and control electromigration of the catalyst.

Appendix B

Process flow for microcantilever heater fabrication

Table B.1 Process sequence for fabricating microcantilever heaters

Process step	Sketch of the structure
1. SOI substrate Device Layer: Si(110), p-type(boron), about 0.08 Ω-cm (0.05-0.15 Ω-cm from supplier), 4 ±0.5 µm BOX: 500 nm Handle Wafer: Si(100), p-type (boron), 5-20 Ω-cm, 500±10 µm	
2. UV lithography (device layer, mask 1, negative resist) a) HMDS priming for 32.5 min. in oven at 150°C b) Spin coating of AZ 5214E resist in SSE spinner. Resist thickness is 1.5 µm. 90°C soft bake on hotplate. c) Exposure in EVG620 Aligner. Before exposure align the wafer flat with Mask 1. Exposure recipe: Hard contact with 20 s wait time, followed by 1.5 s exposure. d) Post exposure bake on hot plate at 120 °C for 120 s e) Flood exposure in EVG620 for 15 s f) Develop in AZ 351B developer diluted 1:5 in water. Development time is 70 to 90 s.	
3. Device layer etching Dry etching machine: RIE-1 Process parameters Step 1: Descum Pressure: 100 mTorr Power: 30 W O_2 flow: 20 sccm N_2 flow: 99 sccm, Time: 12 s Step 2: Si etch (OH_POLYA) Pressure: 80 mTorr Power: 30 W SF_6 flow: 32 sccm, O_2 flow: 8 sccm Time: 15 min to 17 min	

4. Resist strip Machine: Plasma Asher Power: 1000 W O_2 flow: 400 sccm N_2 flow: 70 sccm Time: 30 min	
5. RCA Clean	
6. LPCVD nitride deposition Machine: 6" Furnace, Recipe: 4NITDAN Pressure: 200 mTorr Temperature: 780°C/790°C DSC flow: 40 sccm NH_3 flow: 160 sccm Deposition time: 33 min Thickness: 112 nm Refractive index: 1.98	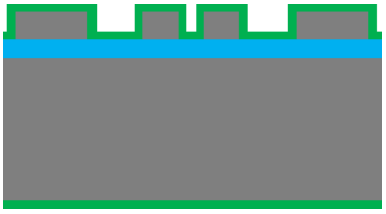
7. Coat protective resist on device layer a) HMDS priming for 32.5 min. in oven at 150°C b) Spin coating of AZ 4562 resist in SSE spinner. Resist thickness is 10 µm. 100°C proximity (gap 1mm) soft bake.	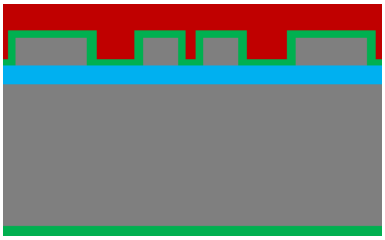
8. UV Lithography (Handle wafer, mask 2, positive resist) a) HMDS priming for 32.5 min. in oven at 150°C b) Spin coating of AZ 5214E resist in SSE spinner. Resist thickness is 1.5 µm. 95°C proximity soft bake (gap 1 mm) for 90 s c) Exposure in EVG620 Aligner. Exposure time: 3 s d) Develop in AZ 351B developer diluted 1:5 in water. Development time is 70 s.	

9. Nitride Dry Etching Dry etching machine: RIE-1 Process parameters Step: Descum Pressure: 100 mTorr Power: 30 W O_2 flow: 20 sccm N_2 flow: 99 sccm, Time: 12 s Step: Nitride etch (OH_PolyA) Pressure: 80 mTorr Power: 30 W SF_6 flow: 32 sccm, O_2 flow: 8 sccm Time: 3 min 40 s to 4 min	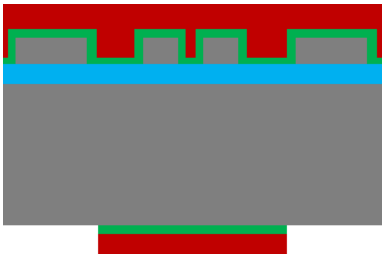
10. Resist strip Plasma Asher parameters: Power: 1000W O_2 flow: 400 sccm N_2 flow: 70 sccm Time: 60 min	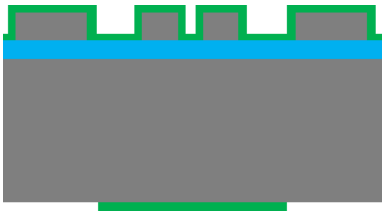
11. KOH etching of handle wafer Etching solution: 28 wt% KOH at 80°C Time: 6 hrs 9 min Etch rate of Si(100): ca. 1.47 µm/min.	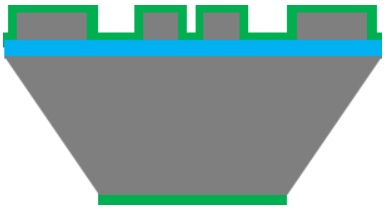
12. Nitride removal Etching solution: 85 wt% H_3PO_4 at 180°C Time: 30 min	
13. BOX removal Etching solution: BHF Time: 10 – 17 min	

14. Reduce cantilever {111} sidewall roughness Mehtod 1: Etching solution : ca. 28 wt% KOH at RT Time: 20s or Method 2: Etching solution: ca. 28 wt% KOH at 60°C Time: 5 to 6sec	
15. Drying the wafer Use critical point dryer Or Dip wafer in BHF for 30 s, rinse in DIW for 5 min and leave to dry in air for 30-45 min with cantilevers pointing up.	

After the chips had been fabricated in the cleanroom, post processing was required before they could become usable in UHV-TEM. Table B.2 summarizes the post processing.

Table B.2 Post processing of fabricated microcantilever heater chip

Process step	Sketch of the structure
1. Attach individual chips to PCB Remove the chip from the wafer and attach it to PCB using EP0-TEK H77 epoxy. Epoxy curing regime in oven: 1 hr at 100°C followed by 2 hr at 120°C	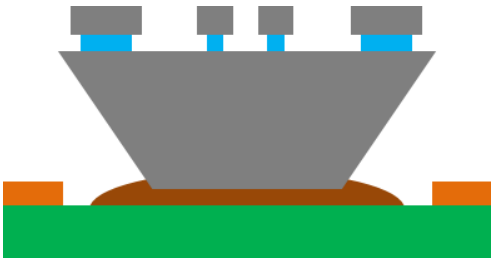
2. Deposit metal on contact pads Deposit 10 nm Ti adhesion layer followed by 80-100 nm Au layer through a shadow mask using e-beam evaporator (Wordentec)	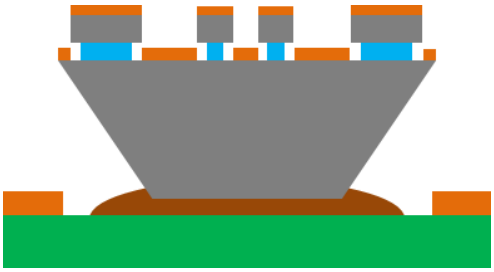
3. Wire bond contact pads to PCB Machine: TPT-H05 wire bonder. Method: Wedge bonding with Al wire	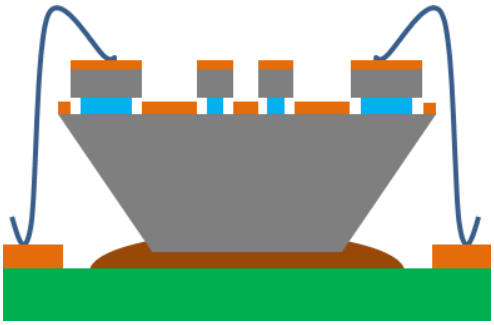

Appendix C

Digitizing videos and calculating volumes and surface areas

C.1 Digitization of videos

In the UHV-TEM setup, the videos were recorded on MiniDV cassettes which were then digitized using video capture equipment and Microsoft Move Maker software. The movies were digitized in 720x480 pixel format at 29.97 fps. Later, freeware software VirtualDub was used to set the correct pixel size of the movies which is 640x480 pixels. VirtualDub was also used to edit and extract short movies from the digitized tapes. Normally, the movies were reduced to 1 fps for normal contact analysis and 0.25 fps for relatively fast processes like nano gap formation. The edited videos were analysed in ImageJ. When the contrast was good and isolation of eutectic was possible by threshold tool of ImageJ, automated particle analysis tool was used piecewise to measure AuSi eutectic and deposited Si dimensions. Videos in which good enough contrast for automated isolation of eutectic was not possible by ImageJ threshold tool, manual measurements were recorded.

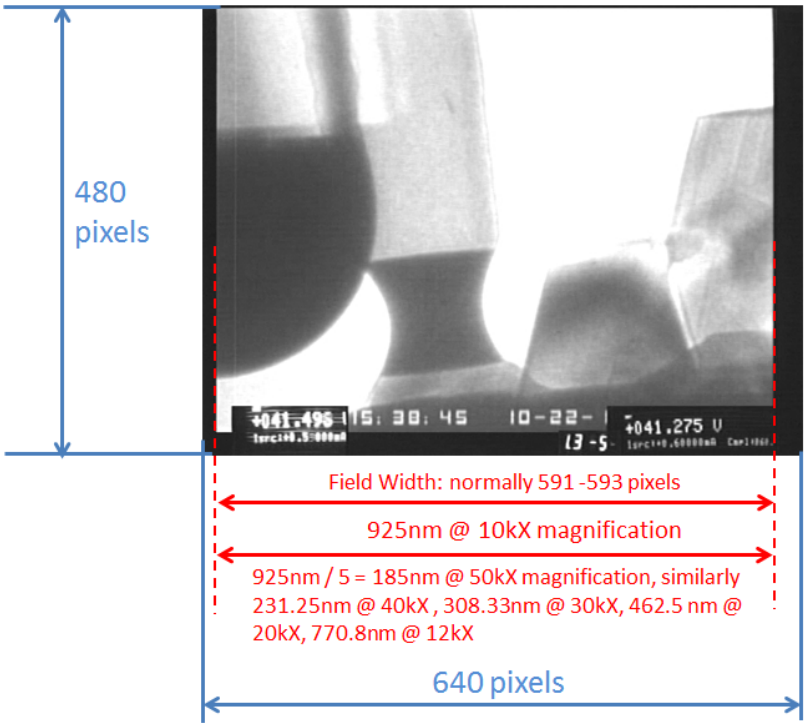

Figure B.1 The correct pixel ratio of the images and horizontal field width for different magnifications.

C.2 Volume and surface area estimation

The volumes are calculated by estimating the geometries to be simple forms. The geometries used in this work are presented in Table C.1, where formulas for the volume (V) and lateral surface area (S) are summarized. The figures and formulas are reproduced from [82] except for the hyperboloid.

Table C.1 Geometries used in volume and surface area estimates of AuSi eutectic and deposited Si during contact formation

Geometries	Formulas	Example (eutectic)
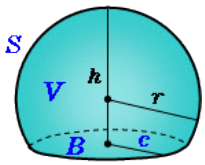	Partial Sphere $V = \frac{\pi}{6}h(3c^2 + h^2) = \frac{\pi}{3}h(3rh - h^2)$ $S = \pi(c^2 + h^2) = 2\pi rh$	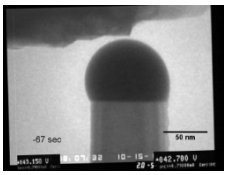
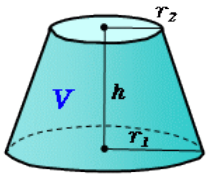	Circular Truncated Cone $V = \frac{1}{3}\pi(r_1^2 + r_1r_2 + r_2^2)h$ $S = \pi(r_1 + r_2)\sqrt{(r_1 - r_2)^2 + h^2}$	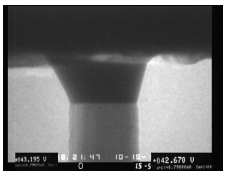
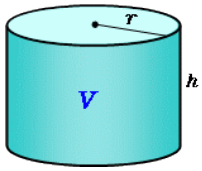	Cylinder $V = \pi r^2 h$ $S = 2\pi rh$	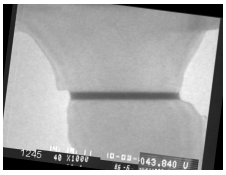
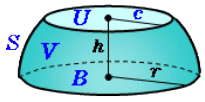	Partial Hemisphere $V = \frac{1}{3}\pi h(3r^2 - h^2)$ $S = 2\pi rh$	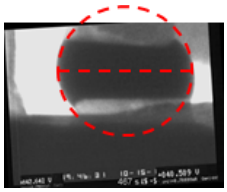
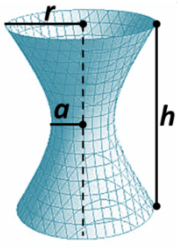	Circular Hyperboloid $V = \frac{1}{3}\pi h(2a^2 + R^2)$ $S \approx$ *surface area of two opposing truncated cones* $S \approx 2\pi(a + r)\sqrt{(r - a)^2 + \left(\frac{h}{2}\right)^2}$	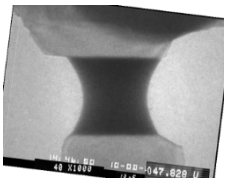

In some cases, the geometry could not be accurately defined by a single shape and a combination of shapes was used to measure the volume and surface areas. In Table C.1, the volume of eutectic, for example, for partial hemispheres is estimated by imaging two partial hemispheres. Similarly, Figure C.2 shows a contact formation process, where the volume of the eutectic was evaluated by considering it to be a combination of a circular hyperboloid and a truncated cone.

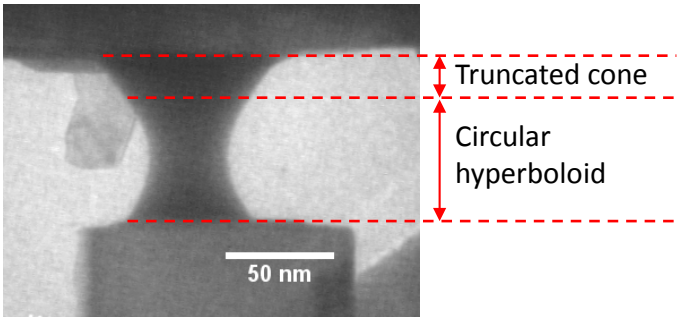

Figure C.2 AuSi eutectic volume is estimated by considering it to be a combination of a truncated cone and a circular hyperboloid

In cases, where the geometry was too complex or the eutectic was partly wetting the sidewalls of the nanowire, as shown in Figure C.3, the volumes (and surface areas) were not calculated and excluded from the data.

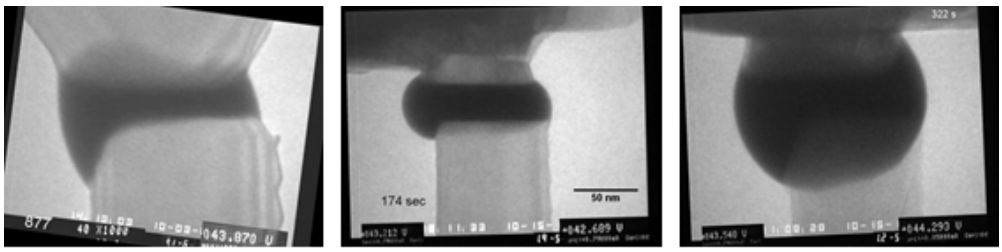

Figure C.3 (a)-(c) Examples of complex geometries of the eutectic, where estimating eutectic volume and lateral surface area is difficult. Such geometries were ignored.

Appendix D

SiNW contact formation examples

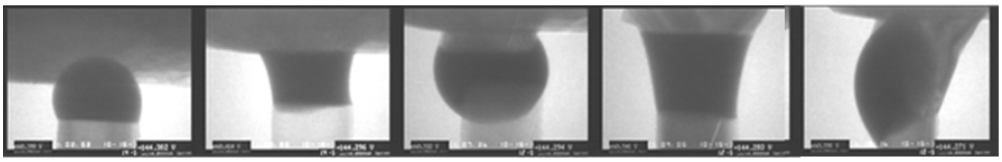

Figure D.1 Bulged contact created when the tip was at 507°C and base of the wire is at 525°C and 750 μA/μm² current was passing through the wire towards the receiving cantilever (electron current towards origin cantilever). This shows that even when temperatures are above 500°C, bulged contacts are created if electromigration is in the direction towards the base of the wire on origin cantilever.

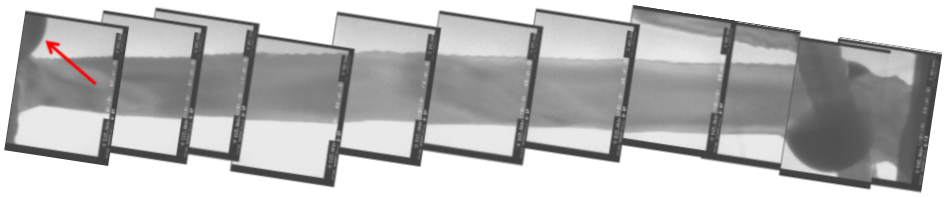

Figure D.2 Bulged contact described in section 5.5.2. AuSi eutectic droplet stays at the contact site but as can be seen (indicated by an arrow) an eutectic droplet was formed at the base of the wire as well. This showed the dominance of electromigration as electron current is in the direction of the base.

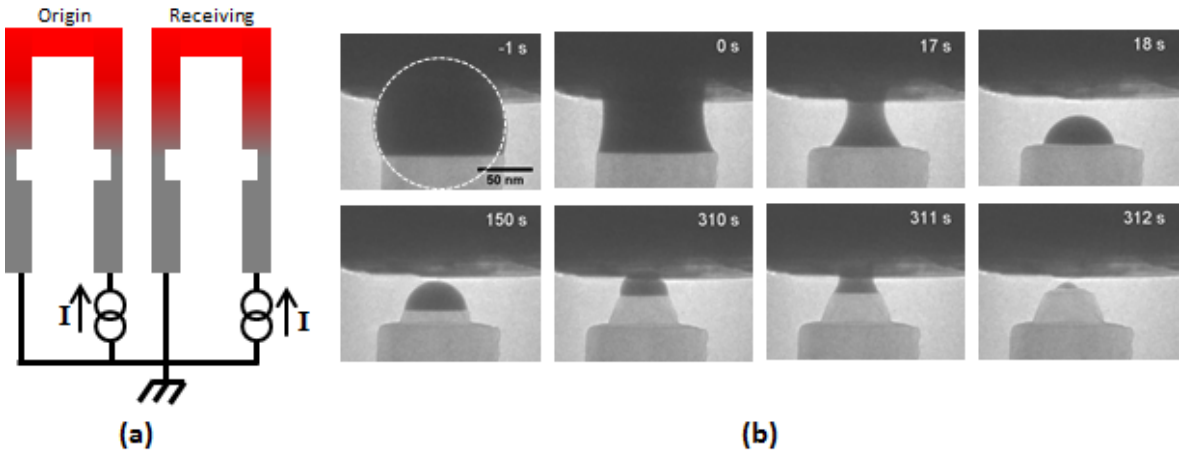

Figure D.3 Nano gap contact created by flipping the power supply connection of the receiving cantilever. **(a)** Schematic diagram showing the electrical setup. Compared to Figure A.3, the receiving cantilever connections are reversed, which will create a voltage difference across the bridging SiNW > 2 V and drive electromigration of Au. Both the cantilevers are supplied a heating current of I=0.78 mA (~30 mW) which sets wire and contact site temperature of ~485°C. **(b)** Sequence of TEM images showing the nano gap formation process. On contact, the eutectic volume reduces at 37000 nm³/s, while Si is deposited by segregation at a rate of 9300 nm³/s, which is 25% of eutectic shrinkage rate. At t=18 s, the AuSi eutectic capillary bridge breaks and the droplet left on the SiNW catalyses further growth and contacts the receiving cantilever again at t=311 s and hence a narrower gap is created.

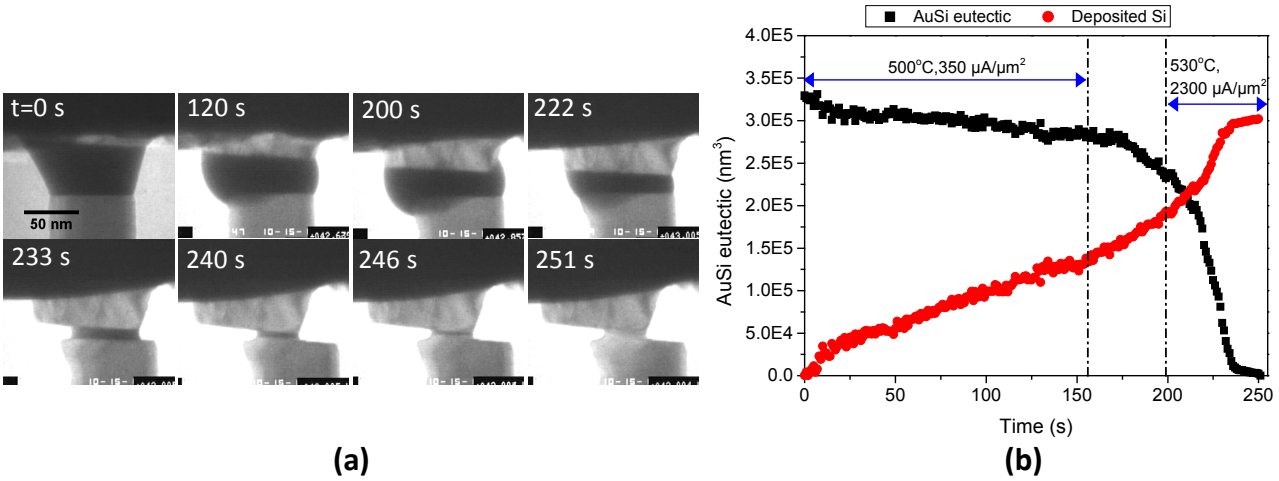

Figure D.4 **(a)** Sequence of TEM images and **(b)** plots of AuSi eutectic and deposited Si volumes as function of time showing an expected bulged contact transformed into necked geometry by increasing the Joule heating current (hence temperature and voltage) of the receiving cantilever during contact formation process. Up till t=156 s, temperature at contact site was 500°C , disilane pressure was 14 μTorr and a current density of 350 μA/μm² was passing through the nanowire. These conditions would have resulted in a bulged contact as AuSi eutectic was shrinking at a much slower rate of 200 nm³/s compared to Si deposition rate of 850 nm³/s. To promote necking, the current of the receiving cantilever was gradually increased from 0.79 mA to 0.88 mA from 157 to 199 s resulting in contact site temperature of ~530°C and nanowire current density increased to 2300 μA/μm² at t=199 s. The new conditions were kept until the necked contact was formed at t=251 s. The dependence of Au migration on diameter can be seen: when the neck was being created the eutectic was lost at a rate of 9000 nm³/s, but when the neck was produced, reducing the interface diameter to 40 nm from 110 nm, the migration proceeded at a rate of 400 nm³/s.

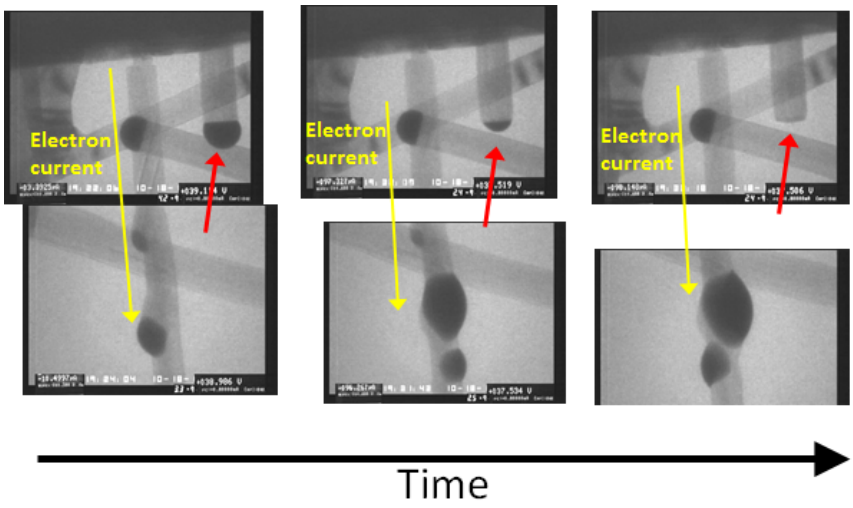

Figure D.5 Sequence of TEM images showing the growth of AuSi eutectic droplets on the SiNW bridge discussed in Section 6.2. Au was driven towards the bridging SiNW surface by electromigration in the direction of electron current (indicated by yellow arrow). Au that was transferred to this SiNW surface came from the cantilever and the neighbouring wires. A nanowire on the receiving cantilever (indicated by red arrow), close to the bridging nanowire lost its AuSi eutectic droplet completely with time as its Au moved to the neighbouring bridging wire.

Appendix E

Creating new VLS silicon nanowire contact geometries by controlling catalyst migration

Sardar B Alam[1], Federico Panciera[2, 3], Ole Hansen[1, 4], Kristian Mølhave[1] and Frances M Ross[3]

1. Department of Micro- and Nanotechnology, Technical University of Denmark, Kgs. Lyngby, Denmark.
2. Department of Engineering, University of Cambridge, Cambridge, United Kingdom.
3. IBM T.J.Watson Research Center, Yorktown Heights, NY, United States.
4. Center for Individual Nanoparticle Functionality, Technical University of Denmark, Kgs. Lyngby, Denmark.

ABSTRACT: The formation of self-assembled contacts between vapor-liquid-solid grown silicon nanowires and flat silicon surfaces was imaged *in situ* using electron microscopy. By measuring the structural evolution of the contact formation process, we demonstrate how different contact geometries are created by adjusting the balance between silicon deposition and Au migration. We show that electromigration provides an efficient way of controlling the contact. The results point to novel device geometries achieved by direct nanowire growth on devices.

KEYWORDS: Nanowire integration, Si nanowire growth, CVD, *in situ* manipulation, TEM, cantilever

The vapor liquid solid (VLS) mechanism[1], a metal catalyzed chemical vapor deposition (CVD) process, is a prominent and versatile bottom-up technique for fabricating silicon nanowires, enabling the creation of large arrays of nanowires with controlled structure. Nanowires grown by the VLS mechanism have a wide range of possible applications: in electronics[2]; solar cells[3]; batteries[4], optoelectronic devices including light emitting diodes[5] lasers[6] and photodetectors[7]; thermoelectric devices[8], electromechanical devices like resonators[9] and piezoelectric generators[10], as well as biological[11] and chemical sensors [12]. The performance of silicon nanowire-based devices depends not only on the nanowire characteristics but also the way in which the nanowires interface with the rest of the circuit, i.e. the intricate details of the electrical connections between each nanowire and the larger scale device.

Recent studies[13–15] have opened the possibility of creating VLS Si nanowire based devices where the nanowire grows towards and touches an opposing surface to form a self-assembled contact. This mechanical and electrical connection is formed catalytically by the metal-Si eutectic droplet at the tip of the wire and can result in an epitaxial Si-Si junction[14]. Recently, such self-assembled contacts have enabled one-step integration of VLS nanowires into transistors[16], mechanical resonators[17,18] and sensors [19] by direct growth on devices heated in a CVD reactor. Nanowire growth can also be achieved at locally heated regions of a microchip system in a gas environment[20,21]. The direct integration of VLS nanowires in device architectures circumvents the integration issues that arise with transferring VLS grown nanowires from a substrate to the device[22,23]. But for direct integration of nanowires in practical applications using self-assembled contact formation, as well as for developing new types of devices, it is important to understand the process that creates the contacts and define techniques to control the contact geometry.

Here we present real time observations, made *in situ* in a transmission electron microscope (TEM), of the physical processes that occur during the formation of self-assembled nanowire contacts. *In situ* TEM not only allows real time observation of the contact formation process but also enables tracking the outcome of variation of different parameters, with the aim of controlling the type of contact created.

We demonstrate that the geometry of the contact between a nanowire and a large scale structure (i.e. a flat surface) can be controlled by varying the contact

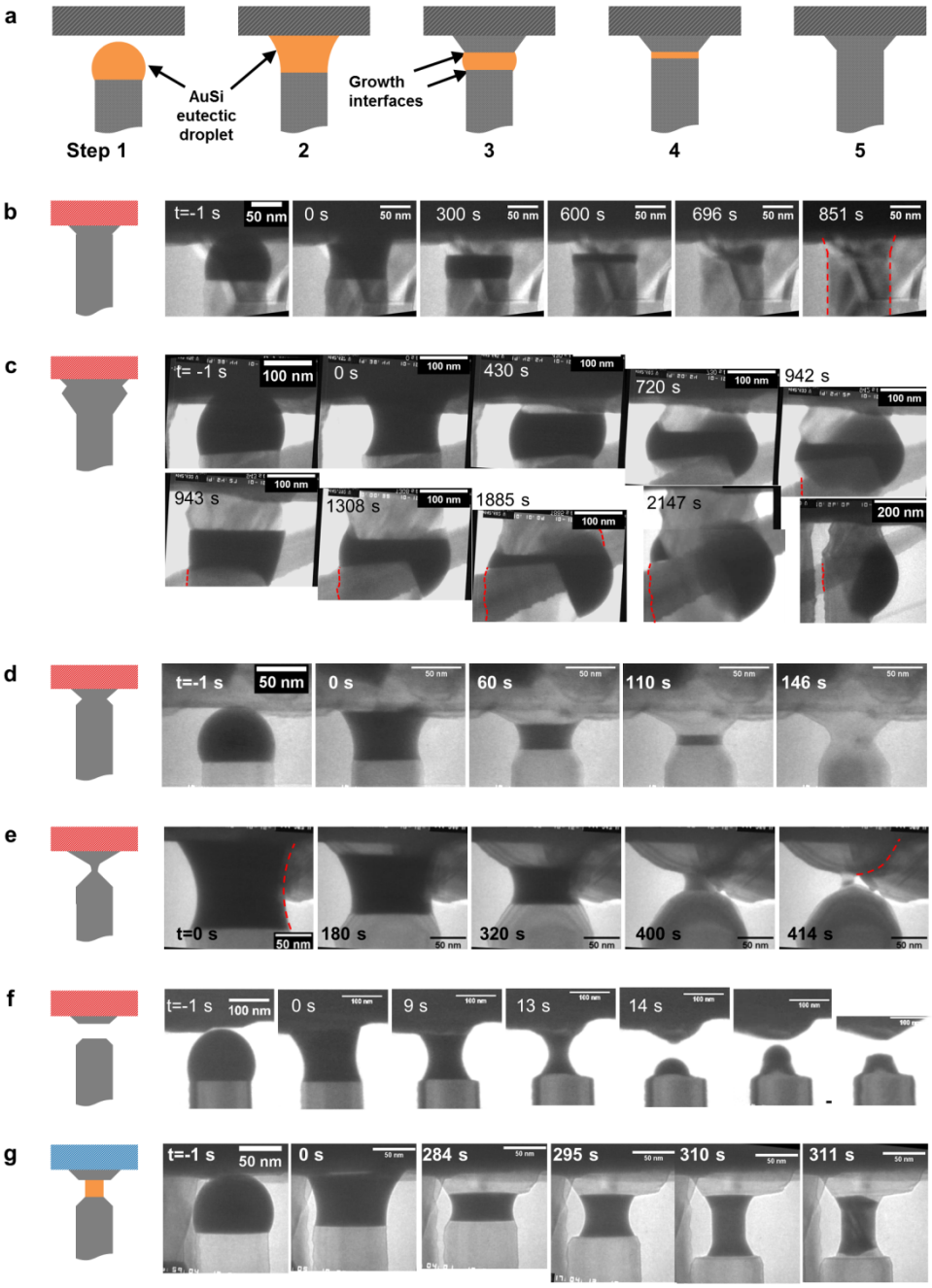

Figure 0.1 (a): Schematic steps in contact formation: (1) t< 0 s, free nanowire approaches the receiving cantilever, (2) t=0 s, moment of contact, when the AuSi catalyst wets the receiving cantilever, (3) t>0 s, Au migrates from contact site while Si is being deposited, and (5) process completion, when final Si-Si contact is created. (b)-(h): Examples of each observed type of contact geometry. (b) Straight contact, created when Si deposition rate ≈ AuSi eutectic shrinkage rate. (c) Bulged Si-Si contact, with Si deposition rate > AuSi eutectic shrinkage rate. (d) Necked Si-Si contact, with Si deposition rate ≲ AuSi eutectic shrinkage rate. (e) Extremely necked Si-Si contact, with Si deposition rate < AuSi eutectic shrinkage rate. (f) Gap, where Si deposition rate << AuSi eutectic shrinkage rate. (g) Si-Au-Si contact created by cooling the system during contact formation; in this nanowire the eutectic is stretched from 35 to 65 nm as the cantilevers contract on cooling at 310 s.

surface temperature and the current through the nanowire during contact creation. These parameters control the Si growth rate and the migration and diffusion of the liquid catalyst at the instant when the nanowire contacts the surface. We show that the balance of growth vs. migration and diffusion gives rise to a variety of contact geometries relevant to electronic and nanomechanical devices.

To form contacts *in situ*, silicon nanowires were grown on silicon cantilever heaters to bridge from one cantilever to an adjacent cantilever[20]. The cantilevers, fabricated on silicon-on-insulator chips, have {111} sidewalls on which nanowires grow perpendicularly in the <111> direction, and are separated by gaps of 2-3 micrometers (see SI). Chips containing cantilever arrays were cleaned with HF vapor, transferred to the UHV system, and 2-5 nm Au was evaporated before vacuum transfer to the UHV-TEM, a Hitachi H-9000 [24]. Pairs of adjacent cantilevers were heated by two independent power sourcemeters operating in constant current mode. On heating to temperatures in the range 470-530°C and flowing disilane (Si_2H_6) at pressures of 1-20 x 10^{-6} Torr, the Au agglomerated and formed AuSi droplets that catalyzed nanowire growth, yielding diameters in the range 40-160 nm. Self-assembled contact formation is initiated when a nanowire grown from one cantilever (referred to as the "origin cantilever"), impinges on the opposing flat sidewall of the adjacent cantilever (the "receiving cantilever"), Figure S1. During or after contact formation, current could be passed through the bridging nanowire by using a third sourcemeter connected between the cantilevers; this sourcemeter could also measure any current that flowed on contact due to small voltage differences between the cantilevers.

Schematics of the observed contact formation process and the different geometries created by adjusting the conditions are shown in Figure 1(a). By controlling the pressure, the temperatures of each cantilever, and the current through the nanowire, we created Si-Si contacts with straight, necked and bulged profiles, as defined by comparing the width at the contact to the nanowire diameter. Particular choices of conditions also formed nano gaps and Si-Au-Si contacts.

The contact formation process, illustrated in the schematic in Figure 1(a) for a straight contact and shown in Movie 1 for a straight and Movie 2 for a necked contact, proceeds as follows: when the impinging wire (step 1) makes contact with the receiving cantilever at t=0 s (step 2), the AuSi eutectic droplet wets the sidewall of the destination cantilever and its geometry is transformed to a hyperboloid sandwiched between the nanowire and sidewall. This sandwiched droplet catalyzes further epitaxial growth (step 3-4) until a Si-Si contact is created (step 5). There are two liquid-solid interfaces from which epitaxial growth could proceed: one growth front is at the AuSi eutectic /nanowire interface, while the second growth front is at the eutectic/cantilever interface (step 2-4). Meanwhile, several processes (coarsening, electromigration) may drive Au away from the contact site, as discussed below. The process is completed when either the two Si interfaces meet or Au migration breaks the connection and forms a gap.

The observations in Figure 1 indicate that the contact morphology is determined by the competition between the rate of migration of Au away from the contact site and the rate of Si deposition. To create a Si-Si contact, sufficient AuSi eutectic should remain at the contact site to ensure catalyzed Si growth proceeds. If the Au migration rate is higher than the Si deposition rate, the two growth interfaces reduce in area as the eutectic volume decreases and a necked contact forms. If Au migration is even faster, Au diffuses away before the Si grows far enough to make contact and a nano gap is created. On the other hand, if the Au migration rate is much lower than the Si deposition rate, a bulged contact is created where the contact is wider than the nanowire. In the bulged case, the growth interfaces increase in area as the liquid is squeezed between the two progressing Si growth fronts. When Au migration and Si deposition rates are comparable, straight contacts are created, with the diameter of the contact structure almost the same as the wire. There is still some widening of the contact at its interface to the cantilever, as the contact angle of the liquid eutectic upon contact increases as contact formation proceeds. The resulting morphology is similar to the early stages of nanowire growth, where the base of the nanowire is wider than its eventual diameter [25].

If the contact formation process is interrupted by cooling, a sandwiched Si-Au-Si contact can be created. The contact in Figure 1(g) was created when the contact formation process was interrupted by simultaneously shutting off the heating current to the two cantilevers. Si-Au-Si contacts can also be created when the receiving cantilever is cold, as previously demonstrated[15].

In order to control the contact morphology, we need to understand and control the factors determining the rates of Si growth and Au migration. Under the conditions used here, the Si growth rate in a freestanding nanowire is well known to be proportional to pressure, independent of diameter, and have an Arrhenius dependence on temperature[26]. During the contact process, a complex geometry with two growth fronts is present, but we find that the growth rate overall actually follows fairly simple kinetics. When the droplet first touches the cantilever, Si continues to deposit. Its growth rate is similar to the pre-contact rate for contacts that end up straight or bulged. In necked contact cases, higher growth rates (by up to 2x) can be seen, as discussed below. Growth then proceeds from either interface, but only one at a time (Figures 1(d) and 2(a)). In other words, growth halts on one interface during deposition on the other. In the overall dataset we found no clear correlation with temperature, interface

diameter, wetting angles or bias voltage across the wire that could predict which interface would be growing. We suggest that Si deposition from the supersaturated eutectic occurs wherever the lowest energy nucleation site for ledges is, and this location may switch from one interface to the other depending on the details of geometry of the changing interfaces. Adding the two growth curves from each interface gives an approximately constant rate of deposited Si (Figure 2(a)). The rate eventually decreases with time as the collection area of the catalyst (AuSi surface area) decreases during the contact process. However, the Si growth rate does not depend only on the liquid surface area. In addition to Si collected from the gas phase at the AuSi surface, there is an additional source of Si, the atoms originally in the AuSi eutectic. These are precipitated as the eutectic volume shrinks due to Au migration. This effect is analogous to the enhanced growth seen in nanowires that are tapering due to a shrinking catalyst droplet[26] and are also the reason necked contacts have higher growth rate than prior to contact. At the growth temperatures used here, the Si content of the eutectic is around 23 to 25% on the Si rich side of the phase diagram[27]. Although the Si in the eutectic is not enough to bridge the hyperbolic geometry made upon the initial wetting, the migration of Au should therefore provide a noticeable additional contribution to the growth rate to achieve solid Si contacts. Figure 2(b) shows the evolution of the AuSi volume with time for the contact process shown in Figures 1(d) and 2(a). In the early stages of the contact formation process (t<60 s), the eutectic volume decreased at a rate of 2400 nm^3/s; the total Si deposition rate was 1300 nm^3/s, of which ~570 nm^3/s is from Si segregation from the eutectic.

Given the approximately constant Si growth rate, one would expect the total time to complete the Si-Si contact (when the two growth fronts meet) to be approximately proportional to wire diameter. This is simply because when a larger wire touches the opposing cantilever at t=0 s, the growth interface is proportionally further from the cantilever surface because the droplet is proportionally larger. Figure 2(c) confirms an approximately linear relationship, once the measured times to contact are corrected for the pressure and temperature of each experiment[26].

It is now clear how the geometry of the contact depends on the balance of Au migration rate and Si deposition rate. For example, the formation of a nano gap depends on whether the Au migration rate is fast enough to move all the AuSi liquid from the contact region before the time, given approximately in Figure 2(c), which would have been required to complete the contact between the interfaces. And the necked morphology of the contact in Figure 2(a, b) is a consequence of shrinking of the growth interface diameters as the eutectic volume decreases at a higher rate than silicon deposition. Bulged contacts are expected when Au migration is slow, giving more time to incorporate Si from the gas phase.

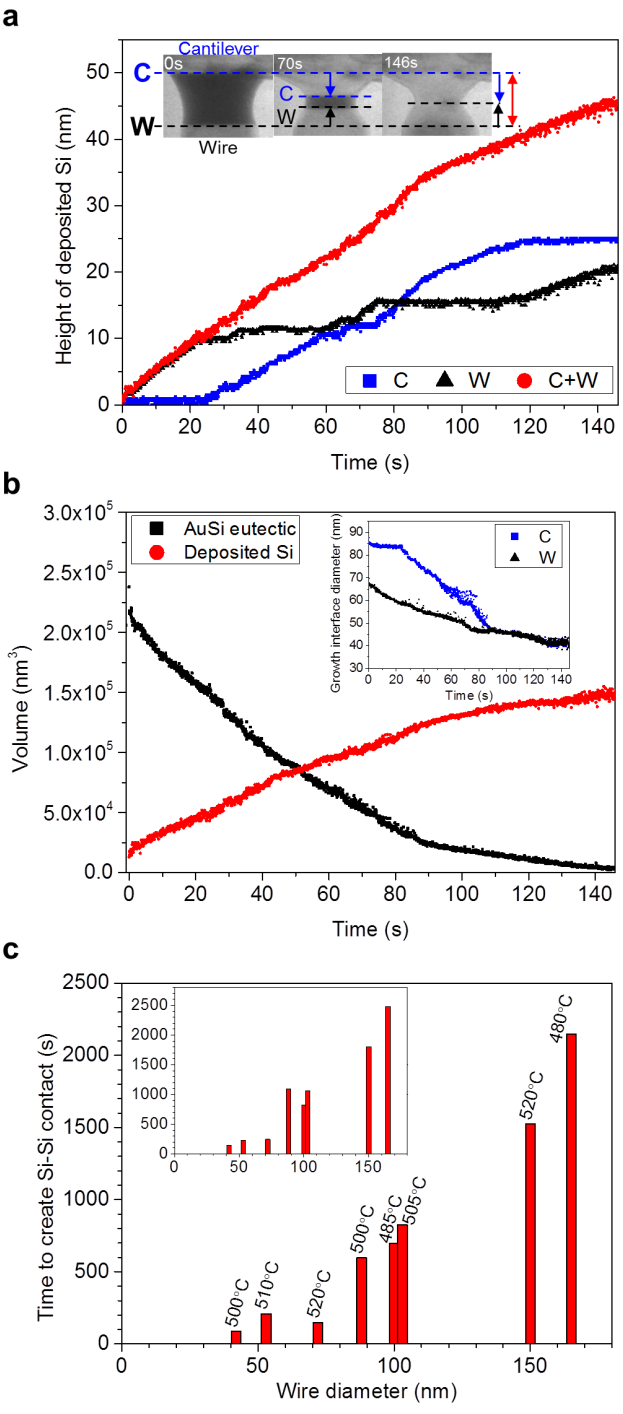

Figure 2 **(a)** Thickness of the Si deposited at the cantilever and nanowire side (C and W) for the necked contact case depicted in Figure 1(d), and the total thickness of Si deposited showing an approximately constant rate; **(b)** Volume of AuSi eutectic and volume of deposited Si for the same contact. The inset shows the diameters at the two AuSi-Si interfaces decreasing in

width, creating a necked contact. (**c**) Time to complete Si-Si contact plotted against nanowire diameter. The contact is said to be complete when the two growth fronts meet. Since the data were obtained at different pressure and temperature, the inset shows the same plot but with times scaled to conditions of $1x10^{-5}$ Torr disilane and 500°C, using the linear dependence on pressure and Arrhenius dependence on temperature[26].

These qualitative conclusions are quantified in Figure 3(a) which shows the relationship between Au migration (the rate of change of AuSi volume measured at the start of the contact process), Si deposition (the volumetric deposition rate, also measured at the start of the contact process) and morphology (ratio of diameter at the middle of the final contact to initial nanowire diameter). The geometry of the self-assembled contact correlates with the ratio. Nano gaps form above the 1:1 line, necked and straight contacts at the line, and bulged contacts below the line. Although, according to the discussion above, nanowire diameter should play a role in determining the morphology, it appears not to be a controlling factor. This is presumably because the range of variation in diameter is only a factor of 4 in these experiments, while the Si deposition and Au migration rates span a much larger range. The Si deposition rate spans two orders of magnitude and is overall consistent with the expected Arrhenius dependence (Figure 3(b)). The migration rate spans four orders of magnitude, and is not well correlated with temperature at the contact site; it will be discussed in more detail below. Clearly a highly enhanced Au migration process is involved in the necked and gap contact cases.

The data in Figure 3 provides insights into which parameters to control in order to create a particular contact geometry for a given nanowire. We first consider the Si deposition rate. This can be increased by raising the temperature, but this is perhaps not a straightforward approach because temperature will also affect Au migration, making it hard to predict the result. Changing the pressure is a better strategy, as pressure has little direct effect on Au migration rate[83]. Figure 4(a1-a4) shows a case where pressure was reduced to allow time for Au to migrate, initiating a necked structure under conditions that were previously forming a bulged contact. However, the range of pressures that can be applied yet still obtain reasonable Si growth rates is relatively limited. Instead, migration of Au appears to be the best parameter to control, because as shown in Figure 3 it can evidently display a large range of values in different experiments. But what drives the Au migration? Several different mechanisms are possible:

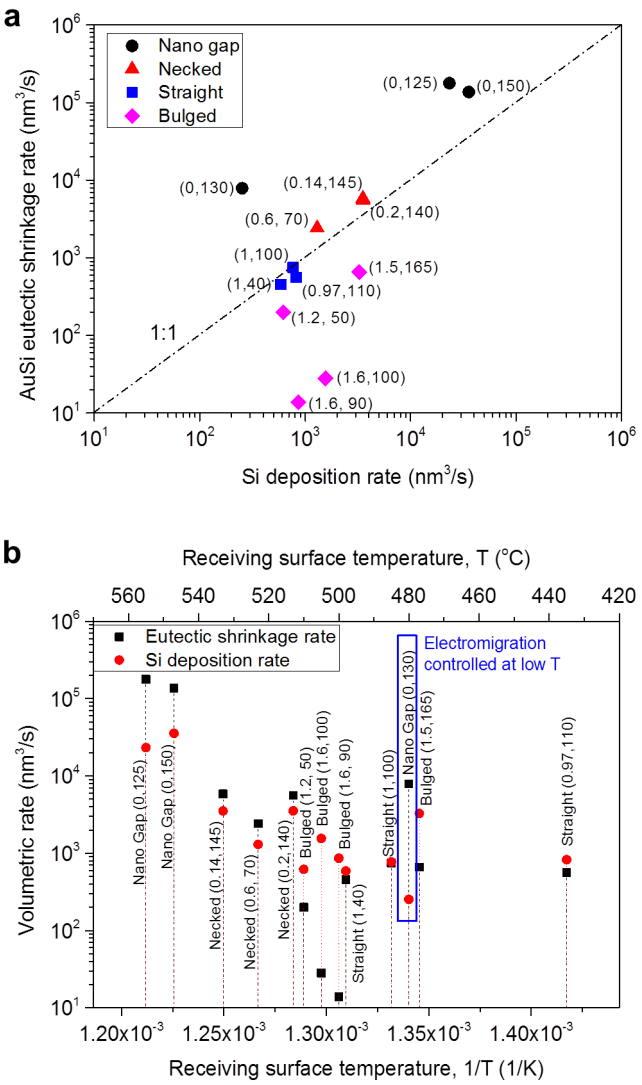

Figure 3 (a) Eutectic shrinkage rate and Si deposition rate shown for different nanowires with a 1:1 guiding line. These values are calculated at the initial time of contact. The geometry of the eventual contact is shown by color and shape. The initial conditions appear to correlate with the final structure. Each data point also shows (ratio of contact width to wire diameter, wire diameter). (b) The same data plotted against inverse temperature. The comparison of the two rates (whether the black dot is above or below the red) correlates with morphology, as expected from (a). The electromigration experiment marked with blue is discussed in the text.

Ostwald ripening, diffusion driven by a surface coverage concentration gradient, thermomigration, and electromigration. We discuss these mechanisms in the SI and conclude that for the conditions of the experiments, electromigration is the dominant

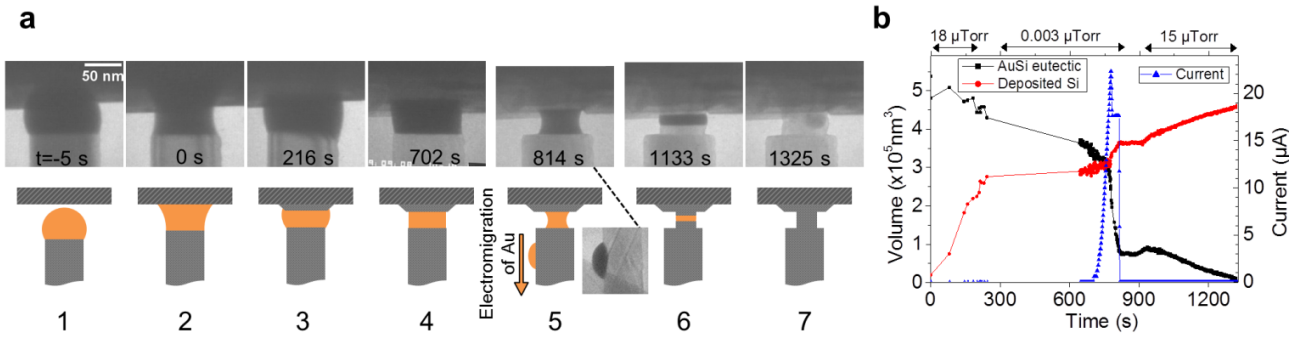

Figure 4 Controlled contact diameter created through pressure and electromigration: (a) Structure and schematic, and (b) Volumetric and nanowire current data. (a1) Before contact. (a2) t=0 s, initial contact and early stage of contact formation, with the eutectic shrinking at 290 nm^3/s and Si deposition at 1130 nm^3/s.. Nanowire and contact site are at 475 ± 10°C, pressure 18 µTorr. (a3) Bulged contact starting to form. The disilane was then reduced to 10^{-9} Torr. (a4) Contact evolves towards a necked geometry, with the eutectic shrinking at 200 nm^3/s, and Si growth rate slow (and impractical) (~50 nm^3/s). (a5) Voltage applied across nanowire. At 3V (27 µA, current density 3700 $µA/µm^2$), eutectic shrinkage was rapid, 4900 nm^3/s, with 1200 nm^3/s Si deposition from segregation. This voltage pulse removes a volume of AuSi that would have taken 16 min in the absence of electromigration. The Au was observed moving in the direction of the electron current along the nanowire towards the origin cantilever (inset image). (a6) Voltage back to 0 V, disilane pressure restored at ~15 µTorr; a narrowed Si-Si contact formed. During this phase the eutectic shrinkage and Si deposition rate were similar, about 200 nm^3/s, leading to a straight contact with 60nm diameter. (a7) Final contact geometry.

mechanism. Electromigration can explain the observation in Figure 3(b) of the very different migration rates seen in otherwise similar experiments: small voltage differences (see SI) between the origin and destination cantilever, arising from slight differences in cantilever resistance even when the heating currents are the same, can drive a ~1 µA current through the nanowire at the moment of contact, forcing Au motion.

The dominance of electromigration allows us to control the contact structure in a practical way. We install a sourcemeter between the adjacent cantilever legs (See Figure S1 and S2(b)) to control the current through the bridging nanowire after the moment of first contact. In Figure 3(b), a current flow of 11 µA after initial contact led to a nano gap in the low temperature of the plot where the migration rate is otherwise low. In Figure 4(a5) and 4b, a pulse of current, several minutes after contact, moved Au and reduced the contact area from 100 nm to 60 nm diameter. The current pulse gives a clear corresponding reduction in eutectic volume and increase in Si by segregation. It is interesting to note that control via electromigration in principle does not require direct observation in a TEM as currents through the wire are indicators of contact process initiation. It is clear from this example that the use of current flow to drive electromigration is a versatile approach to creating complex contact geometries.

To summarize, *in situ* observations show the formation of contacts between Au catalysed silicon nanowires and a flat Si surface, and demonstrate that the final geometry of the contact structure is governed by the relationship between the Si deposition rate and the rate at which the eutectic volume shrinks with time. By controlling the pressure, temperature and current through the nanowire, we can control the balance between Si growth and the eutectic shrinkage due to Au diffusion and electromigration to create contact structures of desired geometries including straight, necked and bulged Si-Si contacts, nano gaps and Si-Au-Si contacts. These contact geometries are interesting for different applications. Si-Si contacts are essential for all electrically connected devices, where well defined thermal, electrical and mechanical contact properties are required from the contacts. The nano gap architecture can be used for field emission sensors and the smaller droplet left in the gap on the nanowire can be further manipulated to create smaller nanowires with smaller nano gaps. Such an approach can be useful for developing field effect devices like gas sensors. Si-Au-Si contacts enable the formation of Ohmic contacts and are useful in diffusion studies.

We find that electromigration is the most reliable method for creating controlled contact geometries. A benefit of using electromigration is that direct observation, as in the TEM experiments here, is not essential to create controlled contact geometries. When a nanowire impinges on the contact site, a current driven through the nanowire by a small applied voltage could be used to indicate the progress of contact formation. A timed current pulse can then reduce the AuSi volume to control the contact diameter. Similarly, nano gap formation can be detected, without direct observation, by monitoring the interruption of current through the nanowire.

The Si cantilever heaters with localized hot regions used here are an interesting option for post processing integration of individual VLS nanowires into temperature-sensitive CMOS devices and labs-on-chip with polymer fluid channels. The high temperatures required for nanowire growth are localized so that the main device remains within its temperature limits (450°C for CMOS and 100-150°C for many polymers). The pristine, oxide-free nanowires that are electrically connected at their two ends in the UHV-TEM also make an interesting platform for surface functionalization studies that, for example, can benefit the fields of biosensors and nanowire based solar cells.

SUPPORTING INFORMATION

The supporting information includes two movies (Movie 1 and Movie 2); information on the design, fabrication, operation and calibration of cantilever heaters, additional details of the method used to grow Si nanowires *in situ* TEM; discussion on Au migration mechanism, and further experimental evidence of dominance of electromigration over other processes. This material is available free of charge via the Internet at http://pubs.acs.org.

Acknowledgements

This work was part of the FTP Nano Live project, which was funded by The Danish Council for Independent Research(Case No.10-083797). This work was (partly) supported by The Danish National Research Foundation's Center for Individual Nanoparticle Functionality, CINF (DNRF54).

REFERENCES

(1) Wagner, R. S.; Ellis, W. C. *Appl. Phys. Lett.* **1964**, *4* (5), 89.
(2) Cui, Y.; Zhong, Z.; Wang, D.; Wang, W. U.; Lieber, C. M. *Nano Lett.* **2003**, *3* (2), 149–152.
(3) Tian, B.; Zheng, X.; Kempa, T. J.; Fang, Y.; Yu, N.; Yu, G.; Huang, J.; Lieber, C. M. *Nature* **2007**, *449* (7164), 885–889.
(4) Chan, C. K.; Peng, H.; Liu, G.; McIlwrath, K.; Zhang, X. F.; Huggins, R. A.; Cui, Y. *Nat. Nanotechnol.* **2008**, *3* (1), 31–35.
(5) Svensson, C. P. T.; Mårtensson, T.; Trägårdh, J.; Larsson, C.; Rask, M.; Hessman, D.; Samuelson, L.; Ohlsson, J. *Nanotechnology* **2008**, *19* (30), 305201.
(6) Duan, X.; Huang, Y.; Agarwal, R.; Lieber, C. M. *Nature* **2003**, *421* (6920), 241–245.
(7) Hayden, O.; Agarwal, R.; Lieber, C. M. *Nat. Mater.* **2006**, *5* (5), 352–356.
(8) Dávila, D.; Tarancón, A.; Fernández-Regúlez, M.; Calaza, C.; Salleras, M.; Paulo, A. S.; Fonseca, L. *J. Micromechanics Microengineering* **2011**, *21* (10), 104007.
(9) Li, M.; Bhiladvala, R. B.; Morrow, T. J.; Sioss, J. A.; Lew, K.-K.; Redwing, J. M.; Keating, C. D.; Mayer, T. S. *Nat. Nanotechnol.* **2008**, *3* (2), 88–92.
(10) Wang, Z. L.; Song, J. *Science* **2006**, *312* (5771), 242–246.
(11) Zheng, G.; Patolsky, F.; Cui, Y.; Wang, W. U.; Lieber, C. M. *Nat. Biotechnol.* **2005**, *23* (10), 1294–1301.
(12) Skucha, K.; Fan, Z.; Jeon, K.; Javey, A.; Boser, B. *Sens. Actuators B Chem.* **2010**, *145* (1), 232–238.
(13) Chaudhry, A.; Ramamurthi, V.; Fong, E.; Islam, M. S. *Nano Lett.* **2007**, *7* (6), 1536–1541.
(14) Sharma, S.; Kamins, T. I.; Islam, M. S.; Williams, R. S.; Marshall, A. F. *J. Cryst. Growth* **2005**, *280* (3-4), 562–568.
(15) Kallesøe, C.; Wen, C.-Y.; Booth, T. J.; Hansen, O.; Bøggild, P.; Ross, F. M.; Mølhave, K. *Nano Lett.* **2012**, *12* (6), 2965–2970.
(16) Quitoriano, N. J.; Kamins, T. I. *Nano Lett.* **2008**, *8* (12), 4410–4414.
(17) Fernandez-Regulez, M.; Sansa, M.; Serra-Garcia, M.; Gil-Santos, E.; Tamayo, J.; Perez-Murano, F.; Paulo, A. S. *Nanotechnology* **2013**, *24* (9), 095303.
(18) Feng, X. L.; He, R.; Yang, P.; Roukes, M. L. *Nano Lett.* **2007**, *7* (7), 1953–1959.
(19) Kamins, T. I.; Sharma, S.; Yasseri, A. A.; Li, Z.; Straznicky, J. *Nanotechnology* **2006**, *17* (11), S291.
(20) Kallesøe, C.; Wen, C.-Y.; Mølhave, K.; Bøggild, P.; Ross, F. M. *Small* **2010**, *6* (18), 2058–2064.
(21) Mølhave, K.; Wacaser, B. A.; Petersen, D. H.; Wagner, J. B.; Samuelson, L.; Bøggild, P. *Small* **2008**, *4* (10), 1741–1746.
(22) Edgar, C. W.; Islam, M. S. 2005; Vol. 6003, p 60030P – 60030P – 11.
(23) Erdem Alaca, B. *Int. Mater. Rev.* **2009**, *54* (5), 245–282.
(24) Ross, F. M. *Rep. Prog. Phys.* **2010**, *73* (11), 114501.
(25) Schmidt, V.; Wittemann, J. V.; Gösele, U. *Chem. Rev.* **2010**, *110* (1), 361–388.
(26) Kodambaka, S.; Tersoff, J.; Reuter, M. C.; Ross, F. M. *Phys. Rev. Lett.* **2006**, *96* (9).
(27) Okamoto, H.; Massalski, T. B. *Bull. Alloy Phase Diagr.* **1983**, *4* (2), 190–198.
(28) Kim, B. J.; Tersoff, J.; Kodambaka, S.; Jang, J.-S.; Stach, E. A.; Ross, F. M. *Nano Lett.* **2014**, *14* (8), 4554–4559.

Supporting Information

Creating new VLS silicon nanowire contact geometries by controlling catalyst migration

Sardar B Alam[1], Federico Panciera [2, 3], Ole Hansen [1, 4], Kristian Mølhave [1] and Frances M Ross [3]
1. Department of Micro- and Nanotechnology, Technical University of Denmark, Kgs. Lyngby, Denmark.
2. Department of Engineering, University of Cambridge, Cambridge, United Kingdom.
3. IBM T. J. Watson Research Center, Yorktown Heights, NY, United States.
4. Center for Individual Nanoparticle Functionality, Technical University of Denmark, Kgs. Lyngby, Denmark.

S1 Cantilever design and fabrication

The design of the cantilever heaters and the experimental setup used in this work is presented in Figure S1. The free standing Joule heated silicon cantilever heaters do not obstruct the electron beam; the temperature of each cantilever could be independently controlled by separate power supplies; and furthermore, electrical characterization could be performed on SiNWs *in situ* after the contact was created, as both cantilevers were electrically isolated from each other and from the Si substrate by a silicon dioxide layer.

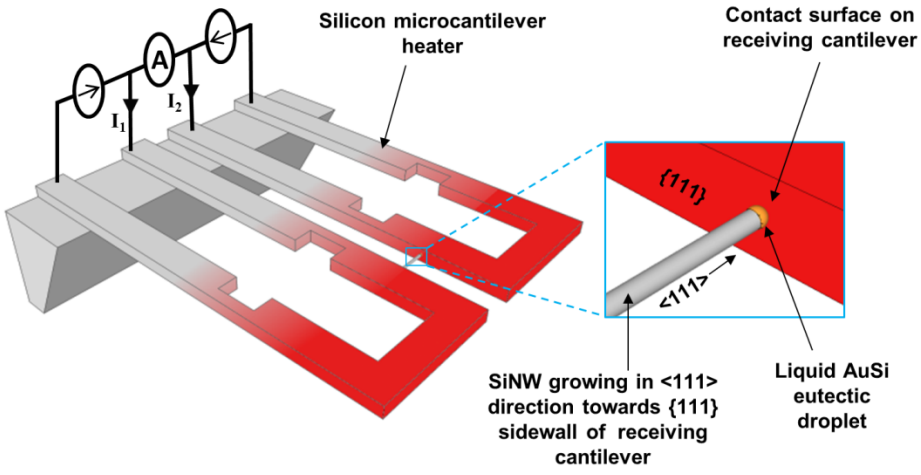

Figure S1 Schematic illustration of the contact formation experiment.

Silicon cantilever heaters were fabricated by a previously used process flow[1]. In this process, the cantilever structures were etched in the device layer of an SOI wafer using reactive ion etching. The device layer was 4±0.5 µm in thickness, had a resistivity of 0.085 Ωcm (boron - $3x10^{17}cm^{-3}$) and <110> orientation, which implied that the opposing sidewalls of the adjacent cantilevers were the desired {111} planes as SiNW prefer to grow in the <111> direction (See Figure S1). After fabrication, the cantilevers were etched in 28% KOH bath for 20 s at room temperature to ensure that the {111} planes of opposing sidewalls were exposed.

The cantilevers were heated to temperatures of 470 to 550°C in UHV-TEM through Joule heating by applying electrical power of about 28 to 40 mW to each cantilever loop. The

electrical power was supplied by two Keithley 2400 SourceMeters which were setup as constant current sources, with supplied current in the range of 0.65 to 1 mA.

The electrical connections were made as shown in Figure S1. There is a slight difference in the voltage distribution over the cantilevers, even when the two cantilever loops operate at same current level, due to slight dissimilarity in the two cantilever loop resistances. Typical resistance of each cantilever is about 42 kΩ with variability about ±1 kΩ. Hence, the two power supplies had an output voltage difference not exceeding ± 0.5 V when operating as constant current sources. Thus, a bridging nanowire could be biased with a <0.3 V voltage and a current in μA range could pass through the wire. This leakage current is obviously higher if the two loops operate at different current levels (and hence, voltage). To measure the current through the nanowire a third Keithley 2400 SourceMeter was connected between the adjacent legs of the two cantilevers. The voltage on this meter (V_R) could be shifted from 0 V (ammeter mode) to a desired voltage if controlled current through the nanowire was required while heating the two cantilever heaters. This setup was used to control the current that passed through the nanowire during contact formation process. Equivalent circuit diagrams with and without the third source/meter are shown in Figure S2(a) and S2(b) respectively.

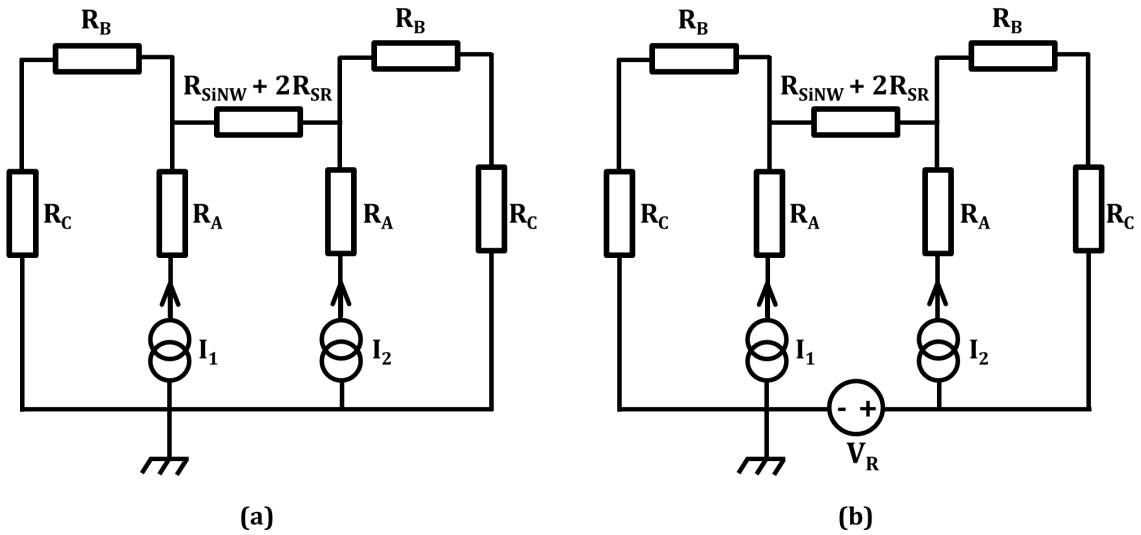

Figure S2 Equivalent circuit diagrams for the cantilever experiments (a) without the third SourceMeter and (b) with the voltage supply/ammeter V_R which sets the reference voltage for I_2 instead of ground. R_{SiNW} is the resistance of the nanowire connected between the two cantilevers and R_{SR} is Maxwell spreading resistance contribution from the contact between the wire and the cantilever. The other resistances shown in the equivalent circuit represent different section of the cantilever heater. Resistances A, B, and C depend on the local temperature and vary slightly between cantilevers.

S2 *In situ* TEM VLS growth

In order to grow nanowires on the cantilever chip, the native oxide was removed from the cantilever surface by vapors from an aqueous 10% HF solution for 10 minutes. The chip was then immediately transferred (within 2 minutes) to the TEM load lock, where it was baked at 100 to 150°C under a tungsten lamp, for several hours (preferably overnight), to degas and remove moisture. Later the sample was transferred to a Knudsen cell Au evaporation system housed in the sample preparation chamber section of the TEM without breaking the vacuum;

thus maintaining an oxide free surface. Using the Knudsen cell evaporator, less than 5 nm of the Au VLS catalyst was deposited on the top and bottom of the cantilever chip at a grazing angle (about 10-15°) to ensure Au coverage on the cantilever side walls. Sufficient Au coverage was essential for non-tapering "healthy" wire growth[2].

After Au deposition, the chip under UHV was transferred directly to the UHV-TEM (Hitachi H-9000). To grow the nanowires by VLS mechanism, the precursor gas disilane (Si_2H_6) was introduced in the UHV-TEM column at pressures of 1-20 x 10^{-6} Torr. Growth rates are low, usually in the range of 5 to 15 nm/min for typical growth temperatures of 470 to 520°C. The nanowires of interest were the ones that traversed the gap between the two adjacent cantilevers (Figure S.1) and reached the sidewall of their opposing cantilever. The gap size between the cantilevers varied from 2.3 to 3 μm, which meant several hours of growth were required before the contact event could be studied.

Images in the UHV-TEM were produced at 300 kV accelerating voltage with the beam current being 1.5 nA. Bright field (BF) imaging mode was mostly used. The images were recorded on MiniDV cassettes at a frame rate of 29.97 fps and were later digitized with each frame size of 640 x 480 pixels. Dimensional analysis was performed using Image J, an imaging processing program. A post-growth image of two cantilevers is shown in Figure S3.

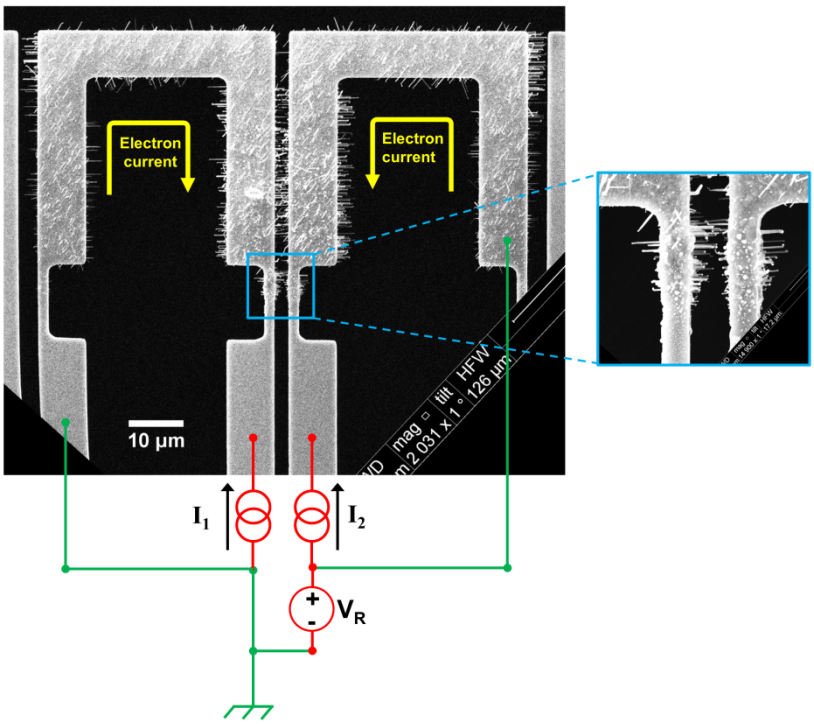

Figure S3 SEM image of cantilever heaters after nanowire growth. The cantilever heaters are operated by constant current source as shown by the connections in this case. The direction of the electron current is opposite to the conventional current. The SourceMeter V_R is used to measure the current through the bridging nanowire. With V_R set to 0V, it behaves as an ammeter but values of V_R can be changed to control the amount of current though the nanowire bridge.

S3 Captions for the movies

Movie M1 shows formation of a straight contact. Horizontal field width is 200nm.Movie shown speeded up 20 times.
Movie M2 shows formation of a necked contact. Horizontal field width is 126nm. Movie shown speeded up 10 times.

S4 Temperature calibration

The temperature of the cantilevers was calculated from the growth rate of nanowires [1,3]. The growth rate is linearly dependent on pressure, and for temperature has an Arrhenius dependence given by [3]:

$$\frac{dl}{dt} = BPe^{-\frac{E_a}{k_B T}} \tag{S.1}$$

which can be re-written as:

$$T = -\frac{E_a}{k_B}\frac{1}{\ln\left(\frac{dl/dt}{BP}\right)} \tag{S.2}$$

where dl/dt is the growth rate in nm/s, E_a is the activation energy, P is the pressure in Torr, k_b is the Boltzmann constant and B is the pre-exponential factor given by nm/s per Torr. Kodambaka et al. [3] fitted the dl/dt vs. T plot for wires grown *in situ* UHV-TEM at a pressure of 10^{-6} Torr to get an activation energy of E_a =0.53±0.02 eV. B can be evaluated to be $3.78\text{x}10^{7}$ nm/(s Torr). The growth rate has a linear dependence on pressure (over at least three order of magnitudes, 10^{-8} to 10^{-5} Torr) [3] and hence E_a and B can be used for other pressure values as well by linear scaling.

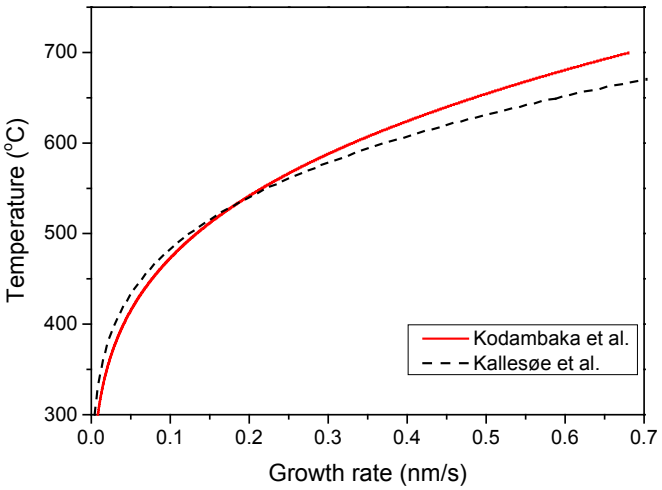

Figure S4 Temperature vs. growth rate for disilane pressure of 10 μTorr. For comparison, temperature curves obtained in [1] are plotted as well and they show small difference in temperatures compared to [3].

Kodambaka et al.[3], used an infrared pyrometer for determination of temperature, which had a relative error of ±20°C for the same sample and an absolute error of ca. 50°C. Here relative

temperature error is more important as temperature gradients are the driving force in situations like thermomigration. It is also worth mentioning that measuring change in length of the nanowire from recorded videos to determine growth rate can introduce some error due to uncertainty in the measurement. This error was reduced by measuring growth rate over at least 1 minute and preferably 3-5 minutes under stable pressure conditions to get an average rate

To determine the conditions of the contact formation process, not only the temperature of the impinging wire but more importantly the temperature of the contact surface on the receiving surface must be measured. The impinging nanowire and the nanowire used for calibrating the receiving surface temperature are ideally at symmetrical locations on their respective cantilevers. Examples of such scenarios are shown in Figure S5. When both cantilevers were heated by equal Joule heating current, the temperatures measured from the growth rate of such nanowire pairs were very similar with only ±10^{o}C temperature difference between them. This suggested that the cantilever heaters on a given chip for equal heating current can be considered close to identical in their temperature profile and the cantilever tip measurements in Fig S6 also indicate reasonable reproducibility in temperature. Hence, in the case of equal currents, if the contact surface temperature is not known, it can be inferred from the impinging nanowire.

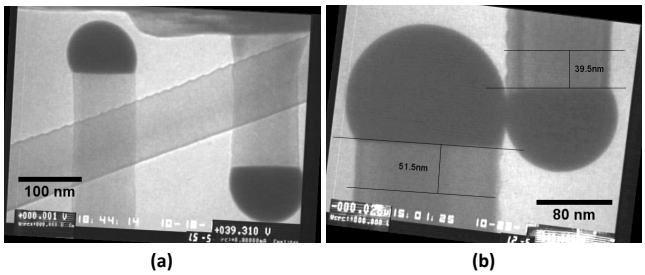

Figure S5 SiNWs growing in symmetric location on their respective cantilevers are ideal for calibrating the nanowire origin and receiving cantilever temperatures.

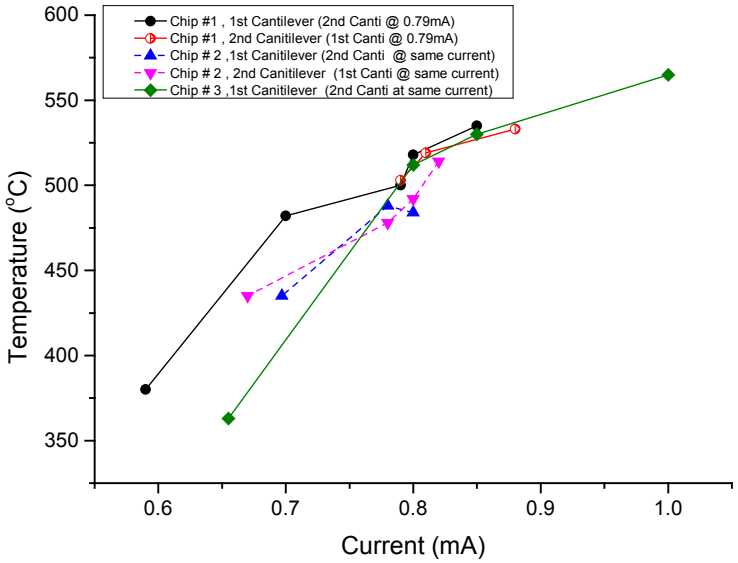

Figure S6 Temperature at cantilever tip plotted against current for three different chips. The cantilevers are normally operated between 0.68 and 0.85 mA.

S5 Factors influencing Au migration

There are a number of mechanisms that can contribute to the migration of Au from the contact site.
(1) Au diffusion due to surface coverage concentration variations is not likely given the overall presence of AuSi eutectic droplets in the vicinity of the contact sites.
(2) In freely growing nanowires, the curvature pressure driven diffusion mechanism of Ostwald ripening (OR) has been identified as a dominant Au migration mechanism during nanowire growth [2]. But this generally is true at higher temperatures. In Fig 1, even highly curved droplets are stable for a considerable part of the time of the longer contact events (such as in the bulged case) that should be unstable by the OR mechanism, while hyperboloid droplets should be OR stable but here can be very short lived despite almost zero mean curvature. Hence, OR is likely not the dominant effect in these short time image sequences.
(3) Thermomigration and (4) Electromigration:
Thermomigration is known for Au on Si [4] and also influences eutectic migration in suspended nanowires[5], but in that work is shown not to be important at the contact site for Joule heated nanowires. In our experiments, it can be difficult to separate thermomigration and electromigration effects because changes in temperature between the two ends of a bridging nanowire are associated with changes in voltage across the nanowire.
We believe that electromigration is the dominant effect, because it appears dominant in the cantilevers as a whole, see below. Furthermore, a high Au migration rate is correlated with applied current flow in Figure 4. We observed that electromigration drives Au in the direction of electron current, as expected [4].

S5.1 Electromigration dominates thermomigration for Au on cantilevers

From Figure S3 a rough estimate can be made for the electromigration of Au on Si under the present conditions. Over approx. 5 hrs of growth, the Au film recedes in the wider section from the outermost constriction in the direction of the electron current, leaving little nanowire growth on that region. The wide section has a current density of 23 $\mu A/\mu m^2$ and from the outer section sidewalls gold has been almost removed from about 20 μm. Since few nanowires are seen on the side facet in the depleted region, the electromigration is apparently also able to remove gold from the eutectic droplet of growing wires, that taper in and have no obvious gold left at the tips in the depleted region.

At the current density found here, electromigration is stronger than thermomigration as the gold is moving with the electron current towards and into the thin region where temperature drops, opposite any thermomigration. This can be seen by comparing the narrower regions of both legs of the cantilever. The narrower region (notch) on the leg connected to the positive terminal has a high density of short wires (we measure a temperature of 430 to 450^{o}C for wires on and above the uppers part of the notch). While the notch on the grounded leg has no wires. This implies a transport mechanism, i.e., electromigration that takes most of the gold to the positive terminal and most gold ends up on the notch. Gold cannot transport below the notch towards the chip body at a high rate as the temperatures below the notch are less than the AuSi eutectic temperature (363^{o}C).

In the bridging nanowires, both current densities and thermal gradients are easily 10 times higher than on the cantilevers. But, if they follow the same dependence, electromigration is likely the major contribution to the observed phenomena, while thermomigration could play a role in cases where no electromigration is present.

References

(1) Kallesøe, C.; Wen, C.-Y.; Mølhave, K.; Bøggild, P.; Ross, F. M. *Small* **2010**, *6* (18), 2058–2064.
(2) Hannon, J. B.; Kodambaka, S.; Ross, F. M.; Tromp, R. M. *Nature* **2006**, *440* (7080), 69–71.
(3) Kodambaka, S.; Tersoff, J.; Reuter, M. C.; Ross, F. M. *Phys. Rev. Lett.* **2006**, *96* (9).
(4) Ichinokawa, T.; Haginoya, C.; Inoue, D.; Itoh, H.; Kirschner, J. *Jpn J Appi Phys Vol* **1993**, *32*, 1379–1384.
(5) Liu, Q.; Zou, R.; Wu, J.; Xu, K.; Lu, A.; Bando, Y.; Golberg, D.; Hu, J. *Nano Lett.* **2015**, *15* (5), 2809–2816.

References

[1] M. S. Dresselhaus, Y.-M. Lin, O. Rabin, M. R. Black, and G. Dresselhaus, "Nanowires," *Springer Handb. Nanotechnol. ISBN 978-3-540-01218-4 Springer-Verl. Berl. Heidelb. 2004 P 99*, vol. 1, p. 99, 2004.

[2] Y. Li, F. Qian, J. Xiang, and C. M. Lieber, "Nanowire electronic and optoelectronic devices," *Mater. Today*, vol. 9, no. 10, pp. 18–27, 2006.

[3] E. C. Garnett, M. L. Brongersma, Y. Cui, and M. D. McGehee, "Nanowire Solar Cells," *Annu. Rev. Mater. Res.*, vol. 41, no. 1, pp. 269–295, Aug. 2011.

[4] F. Patolsky and C. Lieber, "Nanowire nanosensors," *Mater. Today*, vol. 8, no. 4, pp. 20–28, Apr. 2005.

[5] P. Yang, R. Yan, and M. Fardy, "Semiconductor Nanowire: What's Next?," *Nano Lett.*, vol. 10, no. 5, pp. 1529–1536, May 2010.

[6] P. R. Bandaru and P. Pichanusakorn, "An outline of the synthesis and properties of silicon nanowires," *Semicond. Sci. Technol.*, vol. 25, no. 2, p. 024003, Feb. 2010.

[7] W. Lu and C. M. Lieber, "Semiconductor nanowires," *J. Phys. Appl. Phys.*, vol. 39, no. 21, pp. R387–R406, Nov. 2006.

[8] S. Franssila, *Introduction to Microfabrication*. John Wiley & Sons, 2010.

[9] K. A. Dick, "A review of nanowire growth promoted by alloys and non-alloying elements with emphasis on Au-assisted III–V nanowires," *Prog. Cryst. Growth Charact. Mater.*, vol. 54, no. 3–4, pp. 138–173, Sep. 2008.

[10] R. S. Wagner and W. C. Ellis, "VAPOR-LIQUID-SOLID MECHANISM OF SINGLE CRYSTAL GROWTH," *Appl. Phys. Lett.*, vol. 4, no. 5, p. 89, 1964.

[11] R. S. Wagner and C. J. Doherty, "Controlled Vapor-Liquid-Solid Growth of Silicon Crystals," *J. Electrochem. Soc.*, vol. 113, no. 12, pp. 1300–1305, 1966.

[12] Y. Cui, Z. Zhong, D. Wang, W. U. Wang, and C. M. Lieber, "High Performance Silicon Nanowire Field Effect Transistors," *Nano Lett.*, vol. 3, no. 2, pp. 149–152, Feb. 2003.

[13] B. Tian, X. Zheng, T. J. Kempa, Y. Fang, N. Yu, G. Yu, J. Huang, and C. M. Lieber, "Coaxial silicon nanowires as solar cells and nanoelectronic power sources," *Nature*, vol. 449, no. 7164, pp. 885–889, Oct. 2007.

[14] C. K. Chan, H. Peng, G. Liu, K. McIlwrath, X. F. Zhang, R. A. Huggins, and Y. Cui, "High-performance lithium battery anodes using silicon nanowires," *Nat. Nanotechnol.*, vol. 3, no. 1, pp. 31–35, Jan. 2008.

[15] C. P. T. Svensson, T. Mårtensson, J. Trägårdh, C. Larsson, M. Rask, D. Hessman, L. Samuelson, and J. Ohlsson, "Monolithic GaAs/InGaP nanowire light emitting diodes on silicon," *Nanotechnology*, vol. 19, no. 30, p. 305201, Jul. 2008.

[16] X. Duan, Y. Huang, R. Agarwal, and C. M. Lieber, "Single-nanowire electrically driven lasers," *Nature*, vol. 421, no. 6920, pp. 241–245, Jan. 2003.

[17] O. Hayden, R. Agarwal, and C. M. Lieber, "Nanoscale avalanche photodiodes for highly sensitive and spatially resolved photon detection," *Nat. Mater.*, vol. 5, no. 5, pp. 352–356, May 2006.

[18] D. Dávila, A. Tarancón, M. Fernández-Regúlez, C. Calaza, M. Salleras, A. S. Paulo, and L. Fonseca, "Silicon nanowire arrays as thermoelectric material for a power microgenerator," *J. Micromechanics Microengineering*, vol. 21, no. 10, p. 104007, Oct. 2011.
[19] M. Li, R. B. Bhiladvala, T. J. Morrow, J. A. Sioss, K.-K. Lew, J. M. Redwing, C. D. Keating, and T. S. Mayer, "Bottom-up assembly of large-area nanowire resonator arrays," *Nat. Nanotechnol.*, vol. 3, no. 2, pp. 88–92, Feb. 2008.
[20] Z. L. Wang and J. Song, "Piezoelectric nanogenerators based on zinc oxide nanowire arrays," *Science*, vol. 312, no. 5771, pp. 242–246, 2006.
[21] G. Zheng, F. Patolsky, Y. Cui, W. U. Wang, and C. M. Lieber, "Multiplexed electrical detection of cancer markers with nanowire sensor arrays," *Nat. Biotechnol.*, vol. 23, no. 10, pp. 1294–1301, Oct. 2005.
[22] K. Skucha, Z. Fan, K. Jeon, A. Javey, and B. Boser, "Palladium/silicon nanowire Schottky barrier-based hydrogen sensors," *Sens. Actuators B Chem.*, vol. 145, no. 1, pp. 232–238, Mar. 2010.
[23] A. Chaudhry, V. Ramamurthi, E. Fong, and M. S. Islam, "Ultra-Low Contact Resistance of Epitaxially Interfaced Bridged Silicon Nanowires," *Nano Lett.*, vol. 7, no. 6, pp. 1536–1541, Jun. 2007.
[24] S. Sharma, T. I. Kamins, M. S. Islam, R. S. Williams, and A. F. Marshall, "Structural characteristics and connection mechanism of gold-catalyzed bridging silicon nanowires," *J. Cryst. Growth*, vol. 280, no. 3–4, pp. 562–568, Jul. 2005.
[25] C. Kallesøe, C.-Y. Wen, T. J. Booth, O. Hansen, P. Bøggild, F. M. Ross, and K. Mølhave, "In Situ TEM Creation and Electrical Characterization of Nanowire Devices," *Nano Lett.*, vol. 12, no. 6, pp. 2965–2970, Jun. 2012.
[26] N. J. Quitoriano and T. I. Kamins, "Integratable Nanowire Transistors," *Nano Lett.*, vol. 8, no. 12, pp. 4410–4414, Dec. 2008.
[27] M. Fernandez-Regulez, M. Sansa, M. Serra-Garcia, E. Gil-Santos, J. Tamayo, F. Perez-Murano, and A. S. Paulo, "Horizontally patterned Si nanowire growth for nanomechanical devices," *Nanotechnology*, vol. 24, no. 9, p. 095303, Mar. 2013.
[28] X. L. Feng, R. He, P. Yang, and M. L. Roukes, "Very High Frequency Silicon Nanowire Electromechanical Resonators," *Nano Lett.*, vol. 7, no. 7, pp. 1953–1959, Jul. 2007.
[29] T. I. Kamins, S. Sharma, A. A. Yasseri, Z. Li, and J. Straznicky, "Metal-catalysed, bridging nanowires as vapour sensors and concept for their use in a sensor system," *Nanotechnology*, vol. 17, no. 11, p. S291, Jun. 2006.
[30] C. W. Edgar and M. S. Islam, "Recent developments and current challenges in interfacing and integrating 1D semiconductor nanowires in devices and circuits," 2005, vol. 6003, p. 60030P–60030P–11.
[31] B. Erdem Alaca, "Integration of one-dimensional nanostructures with microsystems: an overview," *Int. Mater. Rev.*, vol. 54, no. 5, pp. 245–282, Sep. 2009.
[32] C. Kallesøe, "Integration and post-processing of epitaxial nanowires with silicon technology," Technical University of Denmark, Kgs.Lyngby, Denmark, 2009.
[33] C. Kallesøe, C.-Y. Wen, K. Mølhave, P. Bøggild, and F. M. Ross, "Measurement of Local Si-Nanowire Growth Kinetics Using In situ Transmission Electron Microscopy of Heated Cantilevers," *Small*, vol. 6, no. 18, pp. 2058–2064, Sep. 2010.
[34] F. M. Ross, "Controlling nanowire structures through real time growth studies," *Rep. Prog. Phys.*, vol. 73, no. 11, p. 114501, Nov. 2010.

[35] E. P. Butler, “In situ experiments in the transmission electron microscope,” *Rep. Prog. Phys.*, vol. 42, no. 5, p. 833, May 1979.
[36] J. B. Wagner, F. Cavalca, C. D. Damsgaard, L. D. Duchstein, and T. W. Hansen, “Exploring the environmental transmission electron microscope,” *Micron*, vol. 43, no. 11, pp. 1169–1175, 2012.
[37] R. P. Feynman, “There’s plenty of room at the bottom,” *Eng. Sci.*, vol. 23, no. 5, pp. 22–36, 1960.
[38] “What It Is and How It Works | Nano.” [Online]. Available: http://www.nano.gov/nanotech-101/what. [Accessed: 05-Aug-2014].
[39] D. B. Williams and C. B. Carter, *Transmission Electron Microscopy: A Textbook for Materials Science*. Springer Science & Business Media, 2009.
[40] “TEM Basics.” [Online]. Available: http://www.matter.org.uk/tem/. [Accessed: 04-Aug-2014].
[41] A. Cagliani, R. Wierzbicki, L. Occhipinti, D. H. Petersen, K. N. Dyvelkov, Ö. S. Sukas, B. G. Herstrøm, T. Booth, and P. Bøggild, “Manipulation and in situ transmission electron microscope characterization of sub-100 nm nanostructures using a microfabricated nanogripper,” *J. Micromechanics Microengineering*, vol. 20, no. 3, p. 035009, Mar. 2010.
[42] M. Nakajima, F. Arai, and T. Fukuda, “In situ measurement of Young’s modulus of carbon nanotubes inside a TEM through a hybrid nanorobotic manipulation system,” *IEEE Trans. Nanotechnol.*, vol. 5, no. 3, pp. 243–248, May 2006.
[43] H. Nili, K. Kalantar-zadeh, M. Bhaskaran, and S. Sriram, “In situ nanoindentation: Probing nanoscale multifunctionality,” *Prog. Mater. Sci.*, vol. 58, no. 1, pp. 1–29, Jan. 2013.
[44] G. Harman and J. Albers, “The Ultrasonic Welding Mechanism as Applied to Aluminum- and Gold-Wire Bonding in Microelectronics,” *IEEE Trans. Parts Hybrids Packag.*, vol. 13, no. 4, pp. 406–412, Dec. 1977.
[45] R. Rodwell and D. A. Worrall, “Quality control in ultrasonic wire bonding,” *Microelectron. Int.*, vol. 2, no. 3, pp. 67–72, 1985.
[46] K. Mølhave, B. A. Wacaser, D. H. Petersen, J. B. Wagner, L. Samuelson, and P. Bøggild, “Epitaxial Integration of Nanowires in Microsystems by Local Micrometer-Scale Vapor-Phase Epitaxy,” *Small*, vol. 4, no. 10, pp. 1741–1746, Oct. 2008.
[47] D. S. Engstrøm, N. L. Rupesinghe, K. B. K. Teo, W. I. Milne, and P. Bøgild, “Vertically aligned CNT growth on a microfabricated silicon heater with integrated temperature control—determination of the activation energy from a continuous thermal gradient,” *J. Micromechanics Microengineering*, vol. 21, no. 1, p. 015004, Jan. 2011.
[48] J. Lee and W. P. King, “Microcantilever hotplates: Design, fabrication, and characterization,” *Sens. Actuators Phys.*, vol. 136, no. 1, pp. 291–298, May 2007.
[49] H. C. Casey, *Devices for integrated circuits: silicon and III-V compound semiconductors*. John Wiley, 1999.
[50] N. D. Arora, J. R. Hauser, and D. J. Roulston, “Electron and hole mobilities in silicon as a function of concentration and temperature,” *Electron Devices IEEE Trans. On*, vol. 29, no. 2, pp. 292–295, 1982.
[51] J. Tu, D. Howard, S. D. Collins, and R. L. Smith, “Micromachined, silicon filament light source for spectrophotometric microsystems,” *Appl. Opt.*, vol. 42, no. 13, pp. 2388–2397, 2003.
[52] H. J. M., M. Asheghi, Y. S. Ju, K. E. Goodson, T. W. Kenny B. W. Chui, “Intrinsic-Carrier Thermal Runaway in Silicon Microcantilevers,” *Microscale Thermophys. Eng.*, vol. 3, no. 3, pp. 217–228, 1999.

[53] A. Jungen, M. Pfenninger, M. Tonteling, C. Stampfer, and C. Hierold, “Electrothermal effects at the microscale and their consequences on system design,” *J. Micromechanics Microengineering*, vol. 16, no. 8, p. 1633, Aug. 2006.
[54] D. S. Engstrøm, “Micro-System Integration and Growth Optimization of Vertically Aligned Carbon Nanotubes,” Technical University of Denmark, Kgs.Lyngby, Denmark, 2010.
[55] A. Boukabache and P. Pons, “Doping effects on thermal behaviour of silicon resistor,” *Electron. Lett.*, vol. 38, no. 7, pp. 342–343, Mar. 2002.
[56] Y. S. Touloukian, R. W. Powell, C. Y. Ho, and P. G. Klemens, “Thermophysical Properties of Matter - The TPRC Data Series. Volume 1. Thermal Conductivity - Metallic Elements and Alloys,” 1970.
[57] W. D. Walker and W. Weldon, “Thermal modeling and experimentation to determine maximum power capability of SCR’s and thyristors,” *IEEE Trans. Power Electron.*, vol. 14, no. 2, pp. 316–322, Mar. 1999.
[58] K. Carlson, K. N. Andersen, V. Eichhorn, D. H. Petersen, K. Mølhave, I. Y. Y. Bu, K. B. K. Teo, W. I. Milne, S. Fatikow, and P. Bøggild, “A carbon nanofibre scanning probe assembled using an electrothermal microgripper,” *Nanotechnology*, vol. 18, no. 34, p. 345501, Aug. 2007.
[59] S. Kodambaka, J. Tersoff, M. C. Reuter, and F. M. Ross, “Diameter-Independent Kinetics in the Vapor-Liquid-Solid Growth of Si Nanowires,” *Phys. Rev. Lett.*, vol. 96, no. 9, Mar. 2006.
[60] V. Schmidt, J. V. Wittemann, S. Senz, and U. Gösele, “Silicon Nanowires: A Review on Aspects of their Growth and their Electrical Properties,” *Adv. Mater.*, vol. 21, no. 25–26, pp. 2681–2702, Jul. 2009.
[61] R. F. Wolffenbuttel, “Low-temperature intermediate Au-Si wafer bonding; eutectic or silicide bond,” *Sens. Actuators Phys.*, vol. 62, no. 1–3, pp. 680–686, Jul. 1997.
[62] V. A. Filonenko, “The Stucture of the Gold-Silicon Eutectic Mixture in the Liquid and Solid States,” *Russ. J. Phys. Chem.*, vol. 43, no. 6, pp. 874–876, 1969.
[63] J. B. Hannon, S. Kodambaka, F. M. Ross, and R. M. Tromp, “The influence of the surface migration of gold on the growth of silicon nanowires,” *Nature*, vol. 440, no. 7080, pp. 69–71, Mar. 2006.
[64] E. I. Givargizov, “Fundamental aspects of VLS growth,” *J. Cryst. Growth*, vol. 31, pp. 20–30, 1975.
[65] F. M. Ross, J. Tersoff, and M. C. Reuter, “Sawtooth Faceting in Silicon Nanowires,” *Phys. Rev. Lett.*, vol. 95, no. 14, Sep. 2005.
[66] C. Wiethoff, F. M. Ross, M. Copel, M. Horn-von Hoegen, and F.-J. Meyer zu Heringdorf, “Au Stabilization and Coverage of Sawtooth Facets on Si Nanowires Grown by Vapor−Liquid−Solid Epitaxy,” *Nano Lett.*, vol. 8, no. 9, pp. 3065–3068, Sep. 2008.
[67] S. Kodambaka, J. B. Hannon, R. M. Tromp, and F. M. Ross, “Control of Si Nanowire Growth by Oxygen,” *Nano Lett.*, vol. 6, no. 6, pp. 1292–1296, Jun. 2006.
[68] B. J. Keene, “Review of data for the surface tension of pure metals,” *Int. Mater. Rev.*, vol. 38, no. 4, pp. 157–192, Jan. 1993.
[69] T. Ichinokawa, C. Haginoya, D. Inoue, H. Itoh, and J. Kirschner, “Electro-and Thermomigration of Metallic Islands on Si (lOO) Surface,” *Jpn J Appi Phys Vol*, vol. 32, pp. 1379–1384, 1993.
[70] T. U. Schülli, R. Daudin, G. Renaud, A. Vaysset, O. Geaymond, and A. Pasturel, “Substrate-enhanced supercooling in AuSi eutectic droplets,” *Nature*, vol. 464, no. 7292, pp. 1174–1177, Apr. 2010.

[71] C. E. Allen and E. G. Seebauer, “7 Surface diffusion on semiconductors,” in *Diffusion in Semiconductors*, vol. 33A, D. L. Beke, Ed. Berlin/Heidelberg: Springer-Verlag, 1998, pp. 1–20.
[72] H. B. Huntington, *Electromigration in Metals (chapter in Diffusion in Solids: Recent Developments)*. Elsevier, 2012.
[73] T. Ichinokawa, H. Itoh, and Y. Sakai, “Behaviors of small molten metal islands on several substrates†,” *J Anal Spectrom*, vol. 14, no. 3, pp. 405–408, 1999.
[74] Y. Akira, T. Yasumasa, and Y. Katsumichi, “Surface electromigration of Au on Si(001) studied by REM,” *Surf. Sci.*, vol. 264, no. 1–2, pp. 55–64, Mar. 1992.
[75] H. M. Lu and Q. Jiang, “Surface Tension and Its Temperature Coefficient for Liquid Metals,” *J. Phys. Chem. B*, vol. 109, no. 32, pp. 15463–15468, Aug. 2005.
[76] V. Schmidt, J. V. Wittemann, and U. Gösele, “Growth, Thermodynamics, and Electrical Properties of Silicon Nanowires †,” *Chem. Rev.*, vol. 110, no. 1, pp. 361–388, Jan. 2010.
[77] P. V. Petkov and B. P. Radoev, “Statics and dynamics of capillary bridges,” *Colloids Surf. Physicochem. Eng. Asp.*, vol. 460, pp. 18–27, Oct. 2014.
[78] X. Duan, R. Gao, P. Xie, T. Cohen-Karni, Q. Qing, H. S. Choe, B. Tian, X. Jiang, and C. M. Lieber, “Intracellular recordings of action potentials by an extracellular nanoscale field-effect transistor,” *Nat. Nanotechnol.*, vol. 7, no. 3, pp. 174–179, Mar. 2012.
[79] A. A. Talin, F. Léonard, B. S. Swartzentruber, X. Wang, and S. D. Hersee, “Unusually Strong Space-Charge-Limited Current in Thin Wires,” *Phys. Rev. Lett.*, vol. 101, no. 7, p. 076802, Aug. 2008.
[80] A. M. Katzenmeyer, F. Léonard, A. A. Talin, M. E. Toimil-Molares, J. G. Cederberg, J. Y. Huang, and J. L. Lensch-Falk, “Observation of Space-Charge-Limited Transport in InAs Nanowires,” *IEEE Trans. Nanotechnol.*, vol. 10, no. 1, pp. 92–95, Jan. 2011.
[81] I. Kimukin, M. S. Islam, and R. S. Williams, “Surface depletion thickness of p-doped silicon nanowires grown using metal-catalysed chemical vapour deposition,” *Nanotechnology*, vol. 17, no. 11, pp. S240–S245, Jun. 2006.
[82] keisan.casio.com, “High accuracy calculation for life or science.” [Online]. Available: http://keisan.casio.com/menu/system/000000000280. [Accessed: 19-Aug-2014].
[83] B. J. Kim, J. Tersoff, S. Kodambaka, J.-S. Jang, E. A. Stach, and F. M. Ross, “Au Transport in Catalyst Coarsening and Si Nanowire Formation,” *Nano Lett.*, vol. 14, no. 8, pp. 4554–4559, Aug. 2014.

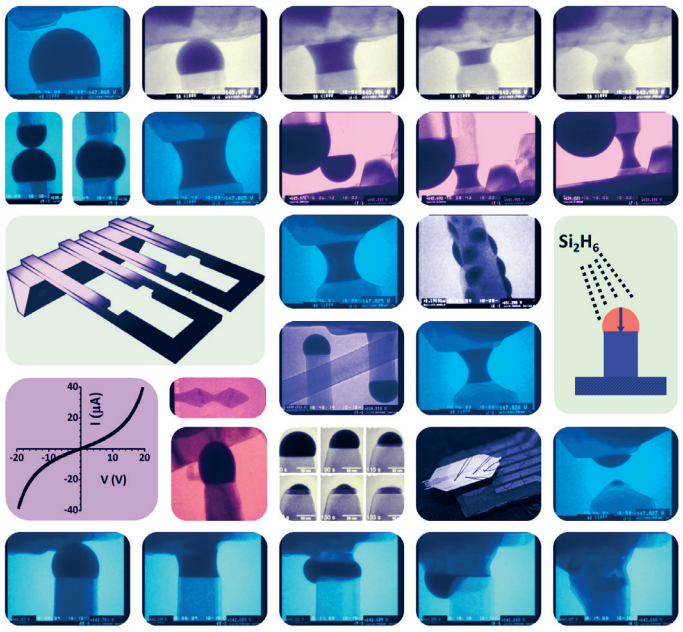

Published by:
DTU Nanotech
Department of Micro- and Nanotechnology
Technical University of Denmark
Ørsteds Plads, building 345B
DK-2800 Kgs. Lyngby